Dissertation zur Erlangung des Doktorgrades
der Fakultät für Chemie und Pharmazie
der Ludwig-Maximilians-Universität München

Effect of genetic rescue at late disease stages on retinal remodeling and visually guided behavior in retinitis pigmentosa

Jacqueline Kajtna

aus

München, Deutschland

2022

Erklärung

Diese Dissertation wurde im Sinne von § 7 der Promotionsordnung vom 28. November 2011 von Frau Prof. Dr. Susanne Friederike Koch betreut.

Eidesstattliche Versicherung

Diese Dissertation wurde eigenständig und ohne unerlaubte Hilfe erarbeitet.

München, den 26.01.2022

…….....Jacqueline Kajtna.....

(Jacqueline Kajtna)

Dissertation eingereicht am 26.01.2022

1. Gutachterin: Prof. Dr. Susanne Friederike Koch

2. Gutachter: Prof. Dr. Martin Biel

Mündliche Prüfung am 23.02.2022

Diese Dissertation enthält Ergebnisse, die in dieser wissenschaftlichen Arbeit veröffentlicht wurde:

Kajtna J, Tsang SH, Koch SF (2022). Late-stage rescue of visually guided behavior in the context of a significantly remodeled retinitis pigmentosa mouse model. *Cellular and Molecular Life Sciences*.

Acknowledgements

First and foremost, I would like to thank my supervisor, Prof. Dr. Susanne F. Koch, who not only provided me with the dream opportunity but also for being an excellent mentor in many ways. She is knowledgeable and joyous, always encouraging and supporting me to explore new realms. Her insightful feedback pushed me to sharpen my thinking and brought my work to a higher level. It was a joy to work with her and learn from such a great scientist. I could not have imagined having a better advisor and mentor.

I wish to thank my dissertation committee for the critical evaluation of my thesis.

I would also like to take this opportunity to thank the research group colleagues Michelle and Moni for their scientific discussions, help in the lab, encouragement, and enjoyable moments. Thanks also to Ann-Kathrin for her help on the RPE analysis and Tobias for the technical assistance. It was a pleasure to share the lab and to work closely with Anna, Antje, Josef, Kirsten, Lew, Nundi, and Oli. Thank you all for the stimulating discussion about science and life that I will miss going forward.

I am grateful to my friends Maja, Žiga, Špela, Luka, Anja, Sara, Gašper, Klara, and Mitja who made my life in Munich so much more enjoyable and exciting.

Finally, I would like to thank my parents and family for all their support possible. I cannot find words to thank you. Most importantly, I would like to thank my mother for all her advice, unconditional love, and understanding. Many thanks to my *oma* for always being there for me. Special thanks to Julia for her sympathetic ear and shoulder to lean on. The deepest acknowledgement I owe to my partner Ivan for his endless love, patience, encouragement, and support. Thank you so much for the amazing past 11 years.

Najlepša hvala vsem!

Table of contents

List of figures

List of tables

Abbreviations

ANOVA	Analysis of variance
AUC	Area under the curve
bp	Base pair
cGMP	Cyclic guanosine monophosphate
CNS	Central nervous system
DVP	Deep vascular plexus
EGFP	Enhanced green fluorescent protein
ERG	Electroretinogram
GCL	Ganglion cell layer
GDP	Guanosine diphosphate
GFAP	Glial fibrillary acidic protein
GMP	Guanosine monophosphate
GS	Glutamine synthetase
GTP	Guanosine triphosphate
H&E	Hematoxylin and eosin
Hsp90	Heat shock protein 90
INL	Inner nuclear layer
IPL	Inner plexiform layer
IS	Inner segments
IVP	Intermediate vascular plexus
L opsin	Long wavelength-sensitive cone opsin
loxP	Locus of x-over, P1
M opsin	Middle wavelength-sensitive cone opsin
ONFL	Outer nerve fiber layer
ONL	Outer nuclear layer

OPL	Outer plexiform layer
OS	Outer segment
PBS	Phosphate-buffered saline
PCR	Polymerase chain reaction
PDE	Phosphodiesterase
PDE*	Activated phosphodiesterase
PFA	Paraformaldehyde
PKC–α	Protein kinase C-alpha
pw	postnatal week
RP	Retinitis pigmentosa
RPE	Retinal pigment epithelium
S opsin	Short wavelength-sensitive cone opsin
SCGN	Secretagogin
SEM	Standard error of the mean
SVP	Superficial vascular plexus
TAE	Tris-acetate-EDTA buffer
WT	Wild type

Summary

Retinitis pigmentosa (RP) is a progressive neurodegenerative disease that causes loss of vision. While RP can be primarily a disease of rod photoreceptors, the downstream neurons of the inner retina, the retinal pigment epithelium (RPE), and the vasculature respond to the death of the photoreceptors in several manners. These changes include neuronal death, morphological changes, cell migration, formation of new neurites, and rewiring. As the diagnosis of RP is usually set during ongoing retinal degeneration, the question arises of whether treatment at late disease stages can halt photoreceptor cell death and retinal remodeling.

In this work, I used an RP gene therapy mouse model deficient in the beta subunit of rod-specific phosphodiesterase 6 (*Pde6b*). In the *Pde6b*$^{STOP/STOP}$ mouse model, both *Pde6b* alleles contain a floxed STOP cassette that prevents PDE6B expression. After tamoxifen injection, a tamoxifen-inducible and rod-specific *CreERT2* recombinase is activated, the STOP cassette removed, and PDE6B expressed in all remaining rods.

In *Pde6b*$^{STOP/STOP}$ retinas, the photoreceptors progressively degenerated and the downstream neurons of the inner retina, especially the horizontal and rod bipolar cells, retracted their dendrites. Furthermore, the RPE, which contacts the photoreceptor outer segments and performs several highly specialized functions for the homeostasis of the retina, gradually changed its cell sizes and shape. The retinal vessels supplying the inner retina responded to photoreceptor degeneration by a reduced area of the vascular network and by the development of acellular capillaries.

To mimic RP gene therapy at late-disease stages, 12, 16, and 24 weeks old *Pde6b*$^{STOP/STOP}$ mice, which have lost 73%, 88%, and 94% of their rods, respectively, were injected with tamoxifen (“treated”). At 40 weeks of age, an extensive morphological analysis of treated, untreated, and wild type retinas was performed. The functional outcome of the therapeutic intervention was studied by electroretinography (ERG) and the Morris water maze task.

In retinas of *Pde6b*$^{STOP/STOP}$ mice treated at 12 or 16 weeks of age, photoreceptor degeneration and remodeling of inner retinal neurons was halted. Furthermore, the genetic rescue was able to stop the functional decline and restore vision demonstrated by ERG measurements and water maze tests, respectively. In fact, in the water maze behavioral tests, the performance of mice treated at 16 weeks of age or earlier was indistinguishable from wild type. Unlike photoreceptor degeneration, inner retinal remodeling, and functional loss, changes in RPE and retinal blood vessels were not halted by treatment at 16 weeks of age, although there appeared to be some slowing of blood vessel degradation. In contrast, no rescue was apparent in mice

treated at 24 weeks of age, suggesting the remaining rod photoreceptors at 24 weeks may already be irreversibly damaged.

These data suggest that restoration of vision via genetic rescue requires only modest threshold numbers of resilient photoreceptors, halting of destructive remodeling, and sustained constructive remodeling.

1. Introduction

1.1. The mammalian retina

The following chapter will describe the location of the retina in the eye, retinal architecture, and delineate the cells that are present in the retina. This will later help to understand the changes in the diseased retina.

1.1.1. The anatomy of the eye

The eye is a sensory organ that transmits visual information to the brain. It works similar to a camera, capturing light that is reflected from objects. Light reflected from objects enters the eye through the transparent cornea, passes through the aqueous humor in the anterior chamber which lies between the cornea and the iris (**Fig. 1**). From there the light hits the transparent biconvex lens held in place by a ciliary body and passes the vitreous body. The lens focuses the light onto the retina. The retina itself is a multilayered tissue located in the inner side of the eyecup. On the outside, the retina is in contact with the retinal pigment epithelium (RPE) that in turn rests on the choroid. The outermost layer of the eye is called the sclera. It is a white-colored coat covering the choroid (1).

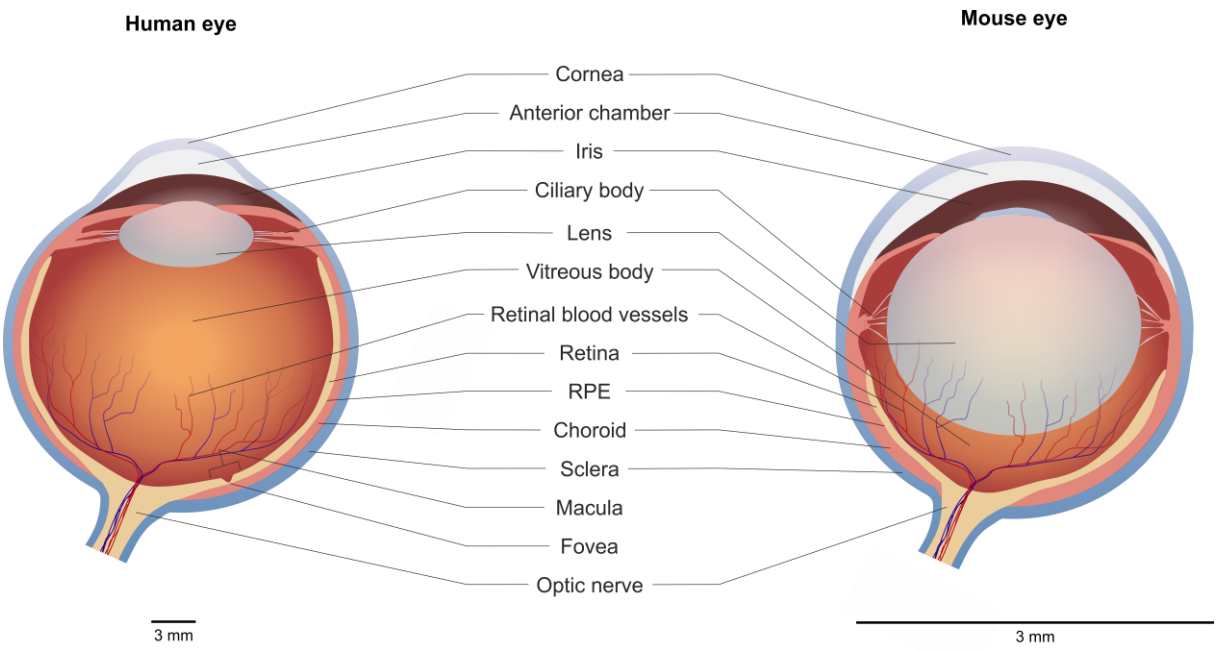

Fig. 1. Schematic representation of the mammalian eye. Human (left) and mouse eye (right). The eye's outermost layer consists of the sclera at the back of the eyecup and the cornea at the front of the eye. The layer in contact with the sclera is the choroid, followed by the retinal pigment epithelium (RPE). In the inner side of the RPE is the retina, which is in contact with the vitreous body on the other side. Scale bar, 3 mm.

Overall, the anatomy of the human and mice eye is similar. However, they exhibit a few differences. First, the retina in humans possesses an oval-shaped macula and inside it, a small central pit called the fovea (**Fig. 1**; left). The fovea is responsible for maximal visual acuity and sharp central vision. It is composed of densely packed cone photoreceptors. The rod photoreceptors are completely absent in the fovea. Their number increases towards the periphery (1). In contrast, in mice, the retina is rod-dominated with a small fraction (3%) of cone photoreceptors that are evenly distributed across the retina. Second, the lens in mice is proportionately larger and rounder in comparison to the human eye (**Fig. 1;** right). Consequently, the vitreous body occupies a smaller amount of the eyecup (2).

1.1.2. Retinal layers

The neural retina is a 100-200 µm thick tissue and contains five major neuronal cell classes: photoreceptors, bipolar cells, horizontal cells, amacrine cells, and ganglion cells (3). Metabolic and homeostatic support is provided by glial cells (4). All these cells are arranged in a multi-layered assembly.

The retina is composed of three layers of cell bodies and two layers of synapses (**Fig. 2A**). The outer nuclear layer (ONL) contains the cell bodies of the rod and cone photoreceptors, the inner nuclear layer (INL) contains the cell bodies of bipolar, horizontal, and amacrine cells, and the ganglion cell layer (GCL) contains the ganglion cell nuclei (**Fig. 2A,B**). The outer plexiform layer (OPL) lies between the ONL and the INL and contains the synapses between the photoreceptor, bipolar and horizontal cells. The inner plexiform layer (IPL) separates the INL and GCL and contains the synapses between bipolar, amacrine, and ganglion cells. The axons of the ganglion cells form the optic nerve and terminate in the visual cortex (5). Additionally, three types of retinal glial cells support the functions of the neurons: the Müller cells span radially from the photoreceptor inner segments (IS) to the inner limiting membrane (1). The microglia, the primary innate immune cells in the retina, have a highly branched morphology and are located in the plexiform layers of the retina (6). Astrocytes that are localized in the GCL and the outer nerve fiber layer (ONFL) play a role in retinal vascularization and contribute to various homeostatic functions (3).

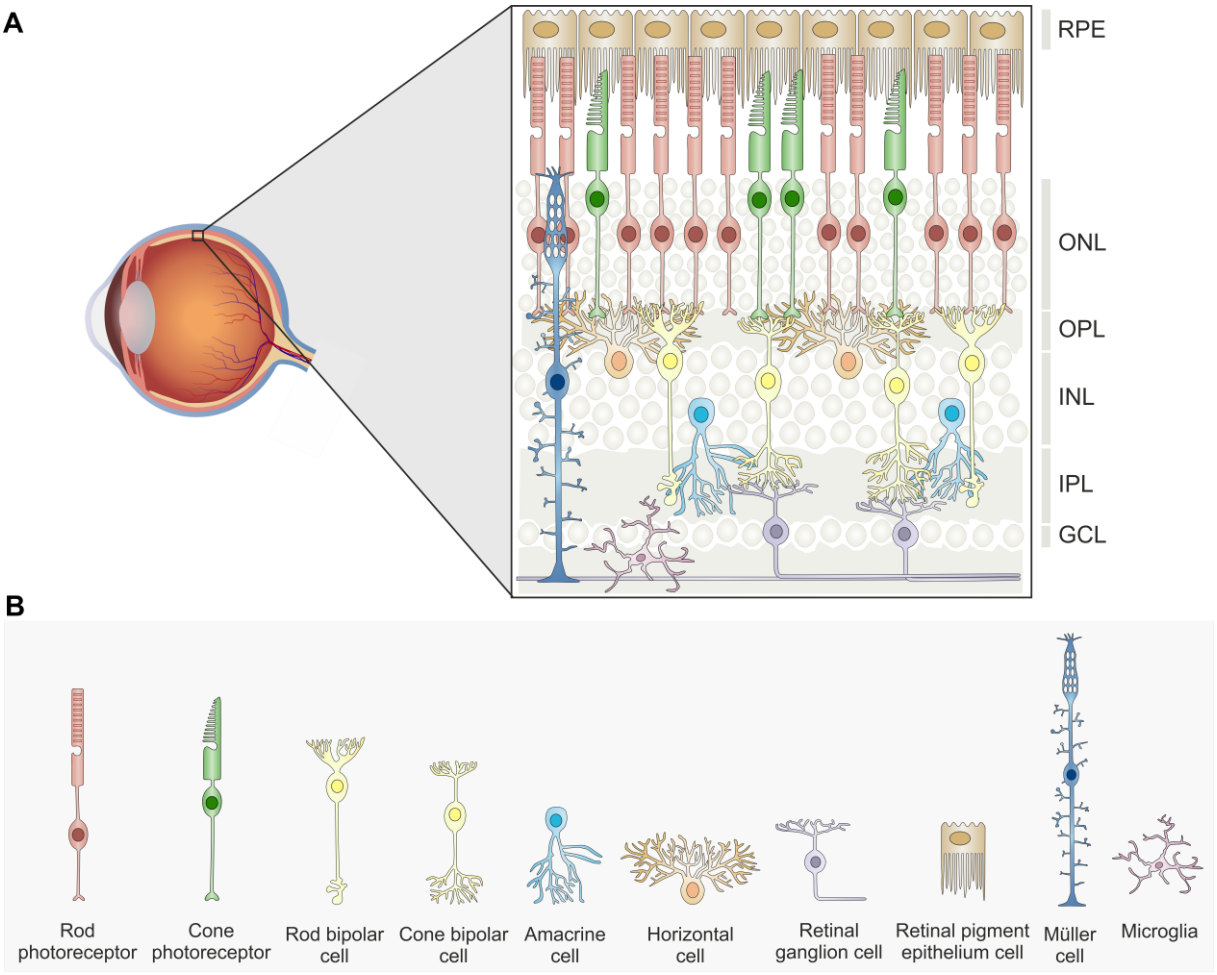

Fig. 2. Schematic representation of the mammalian retina. (A) The retina is located on the inner side of the eyecup and has a characteristic layered structure. It consists of three layers of cell bodies, the outer nuclear layer (ONL), the inner nuclear layer (INL) and the ganglion cell layer (GCL), and two layers of synapses, the outer plexiform layer (OPL) and inner plexiform layer (IPL). **(B)** The retina contains different types of neurons: rod photoreceptors, cone photoreceptors, rod bipolar cells, cone bipolar cells, amacrine cells, horizontal cells, and ganglion cells. In addition, the retina contains retinal pigment epithelium (RPE) cells and glial cells (Müller cells and microglia).

1.1.3. Photoreceptors

There are two types of photoreceptor cells: rods and cones. Rod photoreceptors can detect a single photon and are responsible for vision at low light levels (scotopic conditions). Cone photoreceptors are less sensitive and are engaged for seeing in bright light (photopic conditions). Under mesopic conditions, both rod and cone photoreceptors get activated (7).

While all rod photoreceptors contain the same light-sensitive visual pigment called rhodopsin, cones express several cone opsins with different absorption spectrums that enable color vision. Human trichromatic color vision is enabled by short (S), long (L), and middle (M) wavelength-sensitive cone opsin expression (7). The distribution of the three cone opsins in

humans is mosaic-like (**Fig. 3B**) (8). In the mouse retina, some cones express the S opsin, and 95% of cones co-express both S and M opsin (4, 9). The concentrations of cones expressing both the S and the M opsin decrease from the dorsal to the ventral side. Oppositely, the concentration of S opsin is highest at the ventral side and decreases towards the dorsal side. In the most far dorsal side cones only express S opsin (**Fig. 3C**) (9, 10). Another photoreceptor type are the intrinsically photosensitive retinal ganglion cells that express melanopsin in their dendrites and their soma. These cells contribute to the photoentrainment of the circadian rhythm (11).

Rods and cones have a highly compartmentalized structure that consists of the outer segment, connecting cilium, inner segment, nucleus, and synaptic region (**Fig. 3C**). The outer segment morphology differs significantly between rods and cones. Rod outer segment membrane discs are cylindrical and contain internal optic discs. Cone outer segments are conical shaped, shorter compared to rod outer segments, and are continuous with the plasma membrane (1).

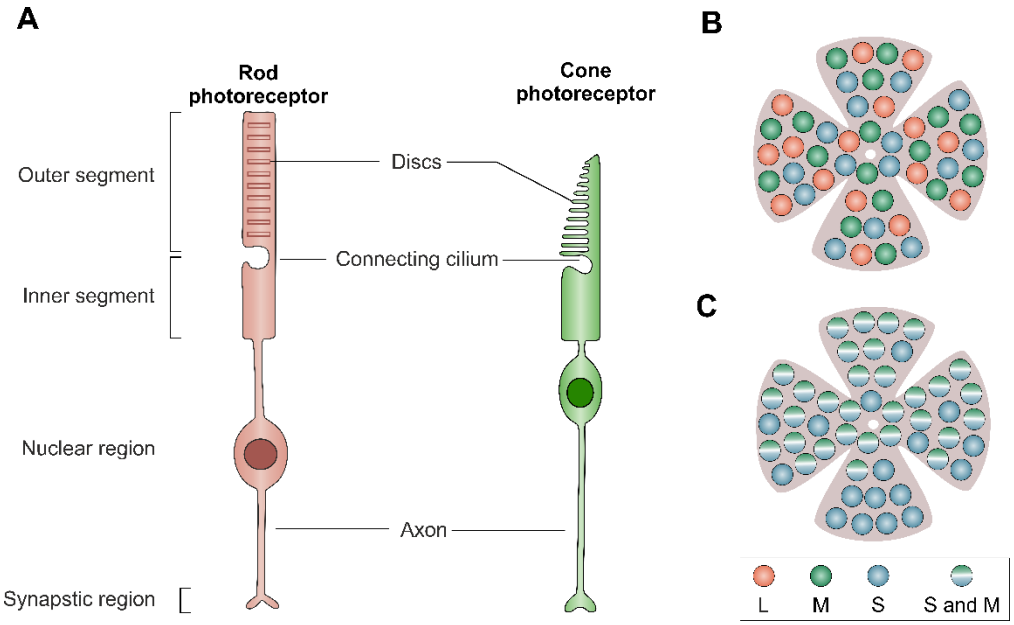

Fig. 3. Photoreceptor types and cone distribution in human and mouse retina. (A) Schematic drawing of a rod (left) and cone (right) photoreceptor cell morphology. Photoreceptor cells are composed of five major structural regions: outer segment, connecting cilium, inner segment, nuclear, and synaptic region. Rod outer segments contain cylindrical free-floating membranous discs, while cone outer segments are continuous with the plasma membrane. Cone outer segments are typically shorter than rod outer segments. Schematic drawing illustrating the distribution of the long (L), and middle (M) short (S) wavelength-sensitive cone opsin in **(B)** human and **(C)** mouse retina.

1.1.4. Rod phototransduction cascade

When light enters the eye and reaches the retina, the light-sensitive layer composed of rod and cone photoreceptors converts light to electrochemical impulses in a process called phototransduction (**Fig. 4**). The photopigment responding to the photon of light is located in the photoreceptor outer segment discs. In rod photoreceptors, the pigment is a glycoprotein called rhodopsin. Rhodopsin and its ligand 11-cis-retinal rest in an inactive state.

After absorption of light (**Fig. 4A**), 11-cis-retinal isomerizes to all-*trans* configuration which leads to conformational changes of rhodopsin to the active form metarhodopsin II. Metarhodopsin II binds to the guanosine triphosphate (GTP)-binding protein transducin. As a consequence of the interaction, GTP replaces guanosine diphosphate (GDP). Simultaneously with GDP dissociation, the α-subunit of the transducin is released which then binds to the inhibitory γ-subunit of the phosphodiesterase 6 (PDE6). PDE6B is a key enzyme of the phototransduction cascade in rod photoreceptors and is composed of two catalytic subunits one α and one β, and two inhibitory γ-subunits. When both γ-subunits of the PDE are bound to the α-subunit of the transducin, PDE6 becomes fully active (PDE6*) and can hydrolyze cyclic guanosine monophosphate (cGMP). The result of the intracellular cGMP concentration drop is the closure of cyclic nucleotide-gated (CNG) cation channels and hyperpolarization. Hyperpolarization causes the voltage-gated Ca^{2+} channels $Ca_V1.4$ at rod terminals to close. When the concentration of intracellular Ca^{2+} drops the glutamate release is slowed down (12, 13).

In darkness (**Fig. 4B**), rhodopsin is locked into its inactive conformation and leaves transducin inactivated. The inhibitory γ-subunits of PDE are bound to the protein complex disabling the enzyme's catalytic activity. Therefore, the intracellular concentration of cGMP is high and keeps the CNG channels open, creating a dark current. In this state, the photoreceptor is depolarized, leading to a high number of open voltage-gated Ca^{2+} channels $Ca_V1.4$ in the synaptic terminal and a high rate of glutamate release (12).

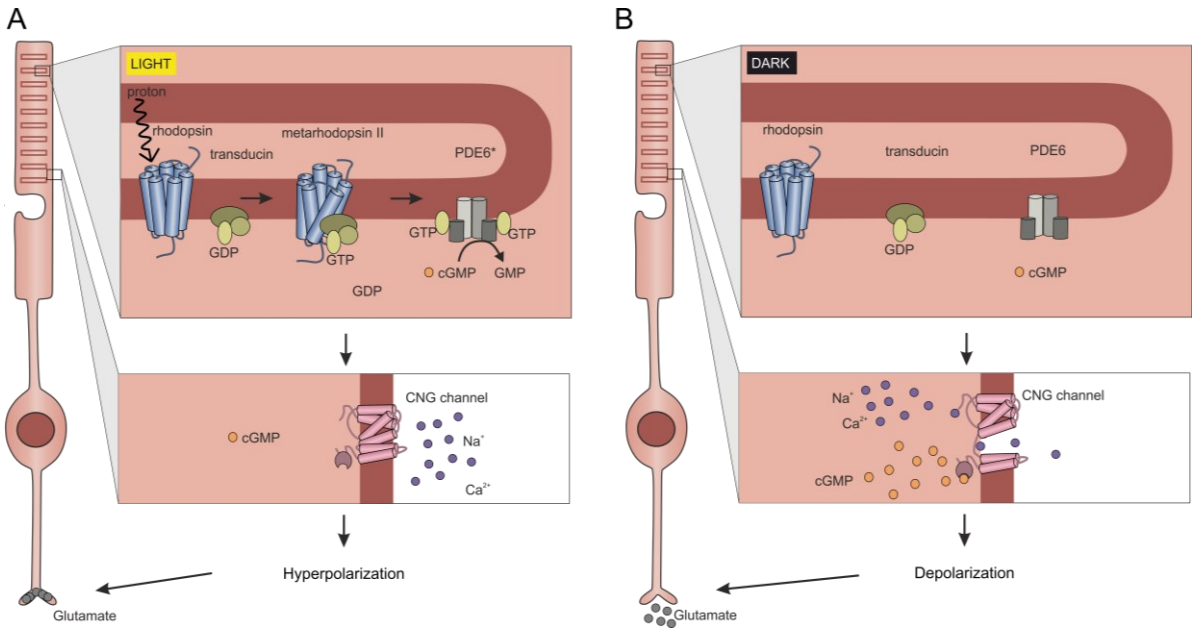

Fig. 4. Phototransduction cascade in rod photoreceptor cells. (A) Absorption of light causes conformational changes of rhodopsin to the activated state known as metarhodopsin II. Metarhodopsin II activates GTP-binding protein transducin. The α-subunit of transducin, in turn, activates PDE6 (PDE6*) by binding the γ-inhibitory subunits of PDE6. As a result, PDE6 degrades cGMP to GMP. Lower intracellular cGMP concentration leads to the cyclic nucleotide-gated (CNG) channels closure and hyperpolarization. The voltage-gated Ca^{2+} channels $Ca_V1.4$ at rod terminals close. The glutamate exocytosis is stopped. **(B)** In darkness, rhodopsin, transducin, and PDE6 are inactive. High cGMP concentration keeps CNG channels open. The inward current of cations keeps the cell depolarized and enables the release of glutamate from synaptic terminals.

1.1.5. Inner retinal cells

The inhibitory neurotransmitter glutamate released from the photoreceptor terminals transmits the information to second-order neurons in the OPL. On the photoreceptor postsynaptic side, the information is processed by the bipolar and horizontal cells in parallel pathways. Horizontal cells participate in light adaptation and modulate synaptic transmission in the OPL. When photoreceptors hyperpolarize and reduce the release of glutamate, horizontal cells hyperpolarize as well providing inhibitory feedback to photoreceptors and bipolar cells (14).

There are 11-14 types of mammalian cone bipolar cells connected to cone photoreceptors, and one type of rod bipolar cell that connects with rods (15, 16). The information from the cone bipolar cells is sent directly to retinal ganglion cells, while rod bipolar cells send their signals to the retinal ganglion cells via the amacrine cells, which in turn make either excitatory or inhibitory synapses with different cone bipolar and ganglion cells (14).

Bipolar cells can be divided into ON and OFF types according to their response to changes in light intensity. The ON bipolar cells have metabotropic receptors and are hyperpolarized to light, while OFF cells possess ionotropic receptors and are depolarized by light. The rod bipolar cells are all OFF cells, cone bipolar cells are both ON and OFF. The bipolar cell terminals contact their postsynaptic partners in the IPL; the ON type synapses make synapses with ON ganglion cells in the inner half and the OFF type with OFF ganglion cells in the outer half of the IPL. Ganglion cells can be divided into around 20 distinct types and transmit the information in form of spikes via the axons through the optic nerve in the brain (14).

1.1.6. RPE

The retinal pigment epithelium (RPE) is interposed between the retina and Bruch's membrane that is the innermost layer of the choroid. On their apical side, the RPE cells contain very long microvilli that engulf the photoreceptor outer segment tips. The RPE is a monolayer of highly polarized penta- to hexagonal shaped cells and performs several highly specialized functions for the homeostasis of the retina. One of the most critical roles is the involvement in the visual cycle of the chromophore retinal. With photon absorption, 11-*cis*-retinal photoisomerizes to all-*trans*-retinal, all-*trans*-retinal is then reduced to all-*trans*-retinol and finally reisomerizes back to the 11-*cis*-retinal in the RPE. Another notable function of the RPE is the daily phagocytosis of shed photoreceptor outer segments (17). Furthermore, the RPE is heavily pigmented and densely packed with melanin. Melanin absorbs the access of light that passes through the photoreceptors and could otherwise damage the outer retina from light generated oxygen reactive species (18, 19). The RPE is also an important part of the outer blood retinal barrier. Other functions include making and regulating numerous growth and signaling factors, selective transport of metabolites and oxygen from the choroidal vessels (17).

1.1.7. Retinal vasculature

The retina's high metabolic demands are met by two distinct vascular networks: choroidal and retinal vasculature (**Fig. 5**). The choroidal vasculature provides nourishment, oxygen supply, and metabolism exchange to the RPE and the outer retina. The inner retina is supplied from the retinal vasculature that is organized in three interconnected planar layers. The first layer containing arterioles, venules, and capillaries is the superficial vasculature plexus (SVP) and lies in the nerve fiber layer or the ganglion cell layer. The second layer is the intermediate vascular plexus (IVP) and lies at the IPL/INL interface. The third layer, the deep vascular plexus (DVP), contains predominantly capillary-sized vessels located at the junction of the INL and OPL. The arrangement of the venous system is similar to the arterial one (20). In contrast to

the fenestrated choroidal vessels (21), nonfenestrated endothelial cells of the retinal vasculature form the inner blood-retinal barrier and mediate the highly selective diffusion of molecules (22). Unlike choroidal circulation, the retinal vessels are not under neurogenic control but are mainly autoregulated in response to the local metabolic needs (23). The retinal vasculature system responds to changes in tissue oxygen levels through autoregulation to ensure a steady blood supply to the capillary network and the retinal cells. The altered concentration of blood gases and partial pressure of carbon dioxide also affects the retinal arteriolar and capillary diameter (20).

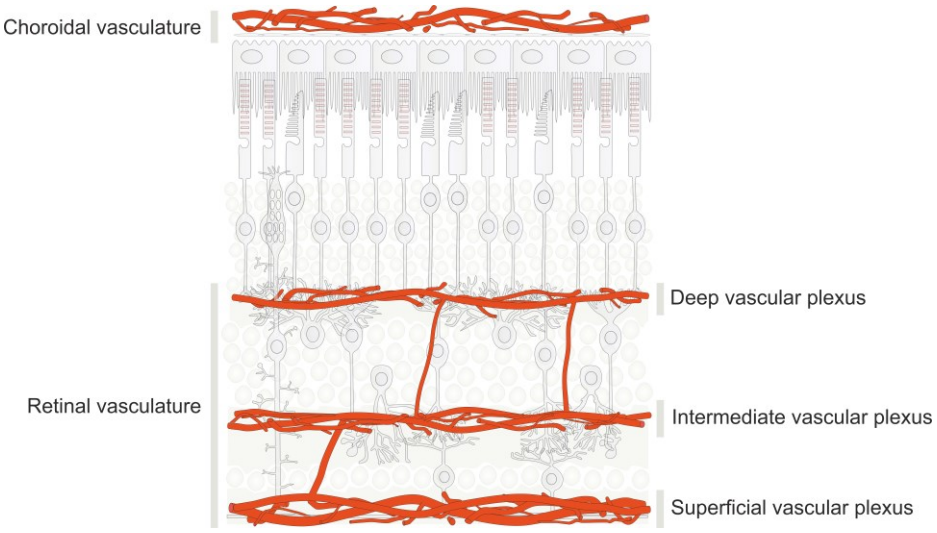

Fig. 5. Schematic representation of the choroidal and the retinal vasculature. The retina is supplied by two vascular systems: the choroidal vasculature that supplies the outer retina and the retinal vasculature that supplies the inner retina. The retinal vasculature system is composed of three interconnected layers: deep, intermediate, and superficial vascular plexus.

1.2. Retinitis pigmentosa

Retinitis pigmentosa (RP) is a group of inherited retinal degenerative diseases characterized by progressive photoreceptor cell loss and retinal pigment deposits. In most cases of RP, the rods start to degenerate, followed by the cones (24). The secondary cone death occurs at later stages of RP when most rod cells have already died. The reason for this subsequent cone death is not known yet (25). Inheritance patterns vary and include autosomal recessive (50-60%), autosomal dominant (30-40%), and X-linked (5-15%) forms. (24, 26). At least 80 genes and 3100 mutations are known to cause non-syndromic RP (27, 28). Some genes like PDE6 (PDE6A, PDE6B, and PDE6G), RP25, and RPE65 have a higher prevalence than others and

are the cause of 2-5% of all autosomal-recessive cases (28). More than 29 genes were found to cause syndromic forms of RP, where RP occurs as part of syndromes that affect other organs as well. The prevalence of typical RP without associated systemic disease is approximately 1:4000 (24, 26).

There is currently no cure for RP. For RP patients with profound visual loss, the ARGUS II, a retinal prosthesis system (29), retinal implant Alpha IMS, retinal implant Alpha AMS and IRIS II (30) can be used to improve visual performance. Clinical trials for novel therapeutic approaches are being conducted including gene therapies (NCT03328130, NCT04794101), optogenetic approaches (NCT04945772) (31), and stem cell therapies (NCT01560715, NCT04604899).

1.2.1. Clinical features and symptoms

First symptoms depend on the form of RP and usually evolve over several decades. The rate and extent of progression of visual loss in RP can vary. In rod-cone dystrophies, the first clinical hallmark is night blindness, which usually appears in adolescence, but sometimes already in early childhood. Night blindness normally goes unnoticed at first, as it has a minor effect on daytime life, while life at night typically includes sufficient light. At this early stage, fundus examination may seem normal, and attenuation of retinal arterioles is modest (**Fig. 6**) (26). An important diagnostic tool is the electroretinogram (ERG) which objectively measures the electrical activity of the retina in response to a light stimulus. It is also useful for the assessment of responses to treatment and following the disease progression (24). At early stages, a decrease in the ERG amplitude of the scotopic b-wave (amplitude from the trough of the initial negative deflection to the peak of the positive b-wave deflection) can be present in some cases. In mid-stages, patients' night blindness restricts their life in a less illuminated night-time environment and on top affects their peripheral vision under daylight, manifested as the so-called tunnel vision (26). Findings on retinal examination include bone spicule-shaped pigment deposits in the equatorial region, retinal vessel attenuation, optic disc pallor, and characteristic changes in ERG patterns (**Fig. 6**). Rod responses under scotopic conditions are usually unrecordable and the cone responses are typically hypovolted. In late stages, patients lose their peripheral vision, with the eventual loss of central vision and progression to total blindness. Clinical examination reveals widespread pigment deposits that reached the macular area, thin vessels, and unrecordable ERG responses (**Fig. 6**) (26).

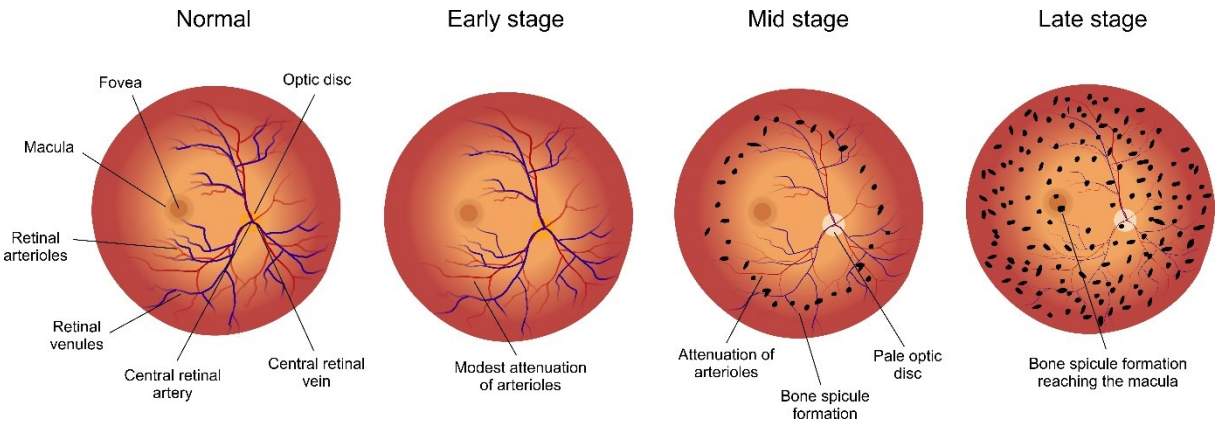

Fig. 6. Schematic representation of the fundus in the healthy retina and RP patients at early, mid and late disease stages. Funduscopic findings in some patients at early stages of RP include modest vessel attenuation, in mid-stages severe attenuation, waxy pallor disc, and bone-spicule-like pigmentation in the equatorial retina. In the late stages, pigment deposits are present all over the retina and the retinal vessels become very thin.

1.3. Retinal remodeling

In RP and other retinal degenerative diseases, photoreceptor loss triggers a series of progressive events in the retina called retinal remodeling. The retina responds to the loss of photoreceptors in a dynamic fashion. Retinal remodeling affects the whole retinal circuity; the main revisions are neuronal cell death, neuronal and glial migration, glial hypertrophy, elaboration of new neurites and synapses, rewiring of retinal circuits, and the formation of the glial seal. Furthermore, morphological alteration in the RPE and the vessels are evident, especially the invasion of the RPE and vessels into the retina (32–36).

Some of those changes might impact the success of the therapy (35). It is therefore important to understand the course of retinal remodeling and how it affects the ability of the retina to respond to therapeutic strategies in different phases of remodeling.

1.3.1. Phases of retinal remodeling

Retinal remodeling can be divided into three major phases of structural changes. Phase 1 is the pre-degeneration period of photoreceptor stress, phase 2 is the period of photoreceptor death and phase 3 is a life-long period of complex neural, glial and vascular remodeling (36). The experiments in this work were focused on phase 2 of the remodeling, where most of the photoreceptor cells have died and retinal remodeling takes place.

Phase 1

In phase 1, diseased rod photoreceptors become stressed. Symptoms of stressed photoreceptors include redirection of opsins to the inner segments, outer segment shortening, and sprouting (**Fig. 7**). Rod axonal processes sometimes sprout and bypass their normal rod bipolar cell targets in the OPL and enter the inner retina, extending to the ganglion cell layer. At the end of phase 1, rods may retract processes from the inner retina before death (32, 33). Rods with shortened outer segments are at risk to die. During phase 1, rod bipolar cells retract their dendrites from rod cells and sometimes extend sprouts towards cone pedicles. Truncation is also present in axons of horizontal cells that contact rods (37). As a consequence of photoreceptor stress, microglia ramify and extend processes towards the photoreceptor layer. Also, Müller cells get activated, start to hypertrophy and change their protein expression including glial fibrillary acidic protein (GFAP) upregulation and glutamine synthetase downregulation (37).

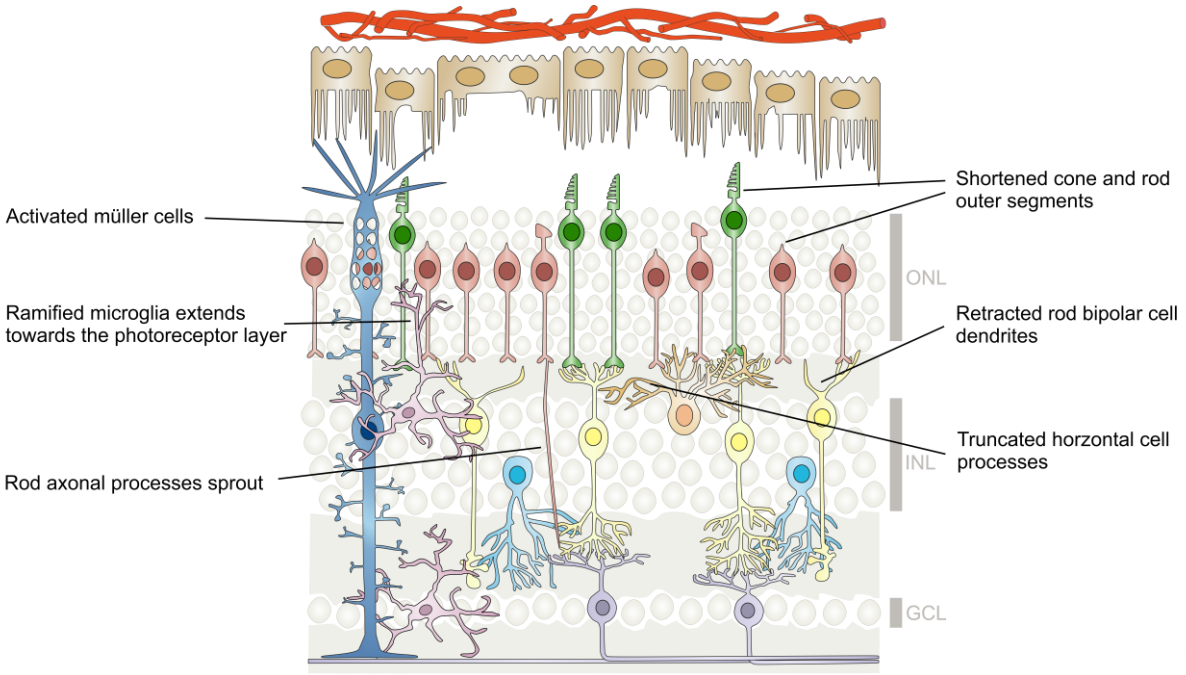

Fig. 7. Schematic representation of phase 1 of retinal remodeling. In this phase, rod and cone photoreceptor outer segments shorten, and some rods extend their neurites into the INL. Bipolar cells and horizontal cells undergo dendrite retraction. Müller cells begin to hypertrophy. Microglia ramify and extend the processes towards the photoreceptor layer. Changes of the RPE will be described in Chapter 1.3.2. Vertical bars: ONL (outer nuclear layer), INL (inner nuclear layer), and GCL (ganglion cell layer).

Phase 2

Phase 2 remodeling begins with rod photoreceptor cell death and ends when all photoreceptors are gone (34, 37). The subretinal space collapses when cone outer segments are gone. Cone opsin is redistributed to inner segments and sometimes transient axon extension into the neural retina can be observed (32).

During phase 2, rod and cone bipolar cells continue to retract their dendrites in response to the loss of rod and cone input (**Fig. 8**). In addition, altered expression of synaptic signaling receptors can be observed (32). Target switching of some rod bipolar cells appears in systems where cones outlive rods. Some rod bipolar cells receive ectopic synapses from cones. After the death of cones, bipolar cells get completely deafferented through the elimination of the glutamate receptors and retract their all dendrites (33). Moreover, a fraction of bipolar cells dies in this phase (32). Horizontal cells extend new sprouts into the IPL, their axons retract, and their cone-targeted horizontal cell somas hypertrophy (32, 37).

In addition, Müller cells continue to hypertrophy and form a distal glial seal. This seal isolates the neural retina from the remnant RPE and the choriocapillaris (37). The seal contains some gaps which allow RPE invasion at a later stage (34). In the metabolically changed Müller cells, the glutathione levels are increased, which points to higher oxidative stress present in the cells (37). Some Müller cell nuclei translocate from the INL into the ONL (32).

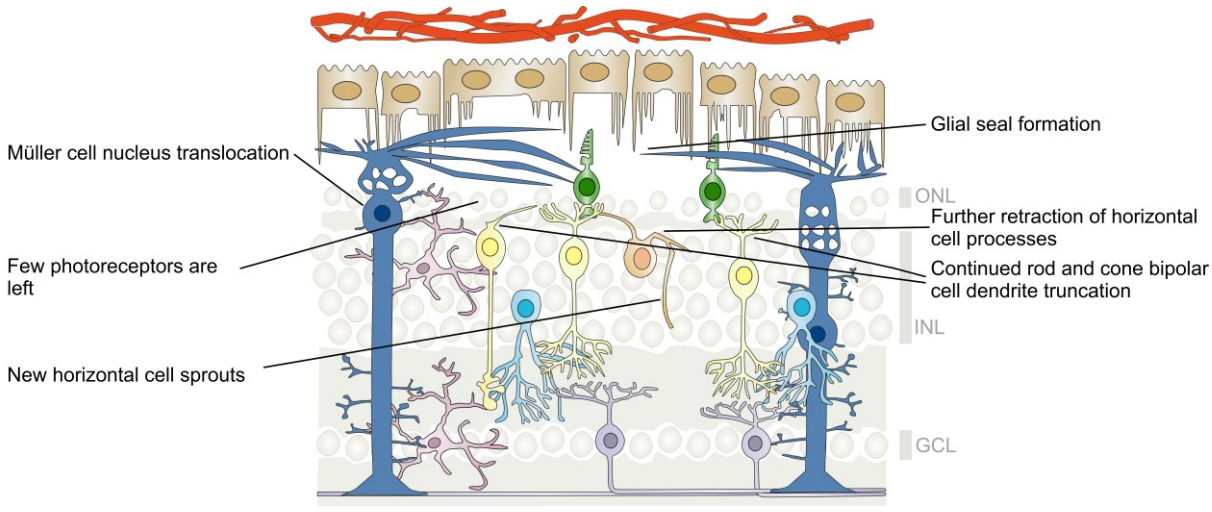

Fig. 8. Schematic representation of phase 2 of retinal remodeling. Phase 2 begins with photoreceptor cell death and ends when photoreceptor cells are completely gone. Horizontal and bipolar cells continue to retract their dendrites and lack them completely at the end. Müller cells seal the neural retina from the RPE with their distal processes. Changes of the RPE will be described in Chapter 1.3.2. Vertical bars: ONL (outer nuclear layer), INL (inner nuclear layer), and GCL (ganglion cell layer).

Phase 3

Phase 3 remodeling is characterized by complex neural remodeling due to photoreceptor loss and the instability of neuronal connectivity. The remaining neurons in the inner retina develop new processes that can form microneuromas outside the normal connectivity areas (**Fig. 9**). Those microneuromas form a typical synapse system with ribbon synapses, vesicle clouds, and post-synaptic dendrites (32) and contain GABAergic amacrine cell, glycinergic amacrine cell, glutamatergic bipolar cell, and ganglion cell processes (38). The formation of new sprouts is triggered due to the loss of afferent input and lack of signaling in neurons. When neurons fail to restore the signaling this results in cell death or cellular somatic migration to other regions of the retina (38). All cell classes migrate along the vertical axis; survived bipolar and amacrine cells translocate to the ganglion cell layer and the ganglion cells into the INL. In addition, some neurons escape the neural retina and extend within the choroid (32, 33). The migration of cells and processes follow the Müller cell hypertrophy, their migration, and the consequential disruption of retinal lamination. In this phase, Müller cells complete the glial seal, isolating the inner retina from the RPE and choroid. Since some gaps in the glial seal remain, RPE cells can migrate into the retina often accompanied by choroidal vessels. Müller cells might also mediate the formation of pigmented bone spicules, which is a common finding in RP patients (33). Furthermore, Müller cells express increased levels of GFAP and decreased levels of GS; and at some point lack GS expression completely. The microglia become less ramified in phase 3 remodeling (37).

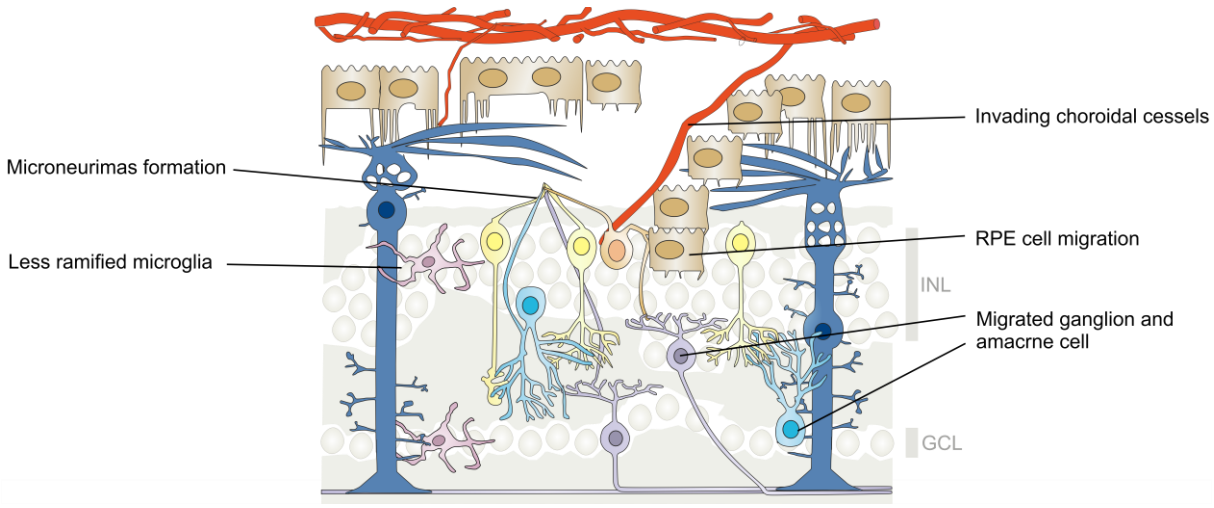

Fig. 9. Schematic representation of phase 3 of retinal remodeling. In this phase cell migration of ganglion and amacrine cells occurs. New bundles of mixed neuron sprouts form microneuromas. RPE cells migrate into the retina along choroidal vessels. Changes of the RPE will be described in Chapter 1.3.2. Vertical bars: INL (inner nuclear layer) and GCL (ganglion cell layer).

1.3.2. Remodeling of the RPE

Following the degeneration of photoreceptors in RP patients, the hexagonal shaped RPE cells become irregular in some areas. The irregularities of the RPE surround shortened and disorganized outer segments (39). In areas with shortened outer segments, the RPE cells contain less pure melanin granules and an increase of melanolysosomes, while in areas with more preserved photoreceptors, many melanin granules were found and fewer melanolysosomes were present (40). When all photoreceptor cells have died, the RPE becomes also irregular and/or hyperplastic (41). Some individual or sheets of RPE cells relocate into the inner retina and form the bone spicule pigment. The bone spicules often surround blood vessels and form a secondary barrier around leaky vessels (**Fig. 9**) (39, 42). As the RPE cells migrate, they lose their surface specialization. Most of the translocated RPE cells lack basal inholdings and contain no lipofuscin granules (43). The size and shape of the migrated RPE cells vary, most lose their polygonal shape (41).

In mouse models of RP, the RPE cells show morphological alterations (44–46). In the rd10 mouse model, RPE changes were already detectable when only 10 % of photoreceptors have died. At later disease stages (at 100 days) the RPE morphology showed even more disruptions. In the central area, RPE cells varied in size with a fraction of cells being larger than the others. In the equatorial region, cells were compressed or became elongated, while in the periphery the RPE looked quite normal at this stage. Later, also the peripheral area became disrupted (45, 46). When the photoreceptors were gone, also the RPE was lost (47). Just as in human RP patients, RPE cell migration was observed in mice and was related to the selective loss of rod and cone photoreceptors. RPE clusters around the retinal vessels correlated well with bone spicule formations in humans (48).

1.3.3. Remodeling of the retinal blood vessels

In addition to the remodeling of the retina and the RPE, changes in both vascular systems supplying the retina were reported in RP patients. Changes in the retinal blood vessels include reduced blood flow (49–51), thinning of the lumen (43, 49, 50, 52), and reduced vessel density with the greatest effect observed in the deep retinal plexus (53–55). It is hypothesized that the reduced retinal blood flow and vasoconstriction may be a consequence of the decreased metabolism due to decreased number of photoreceptors (49, 52, 56). A decreased number of photoreceptors might consume less oxygen and lead to increased oxygen levels (49). Moreover, a decreased number of photoreceptors also lower the distance from the choroid to the inner retina, which also promotes increased oxygen levels (49). As the retinal vasculature

has the ability to react to local oxygen levels, increased oxygen levels might lead to retinal vasoconstriction, and the blood flow decrease (57).

Similar observations were made in mouse models of RP. With disease progression, loss of retinal vascular network length (58), especially an early and rapid DVP decrease, is present (59–61). Another feature observed in the retinal vasculature is the formation of acellular capillaries (62), which are non-perfused remnants of capillaries with no endothelial cells (63). Although the photoreceptors trigger retinal vascular degeneration, these disruptions of the vessels plexus may also accelerate the progress of retinal degeneration (59) and have an impact on rescue success.

1.4. RP mouse model

Mouse models of RP have been used for many years to investigate the mechanism of disease, understand its progression, and predict the effectiveness of treatment. Several mouse models of RP are available, some with naturally occurring mutations, while others have been genetically engineered (2). In order to understand the plasticity of the remodeling in RP and its effect on vision following genetic rescue therapy, a genetically engineered mouse model that employs the Cre-*loxP* system was used in this study.

1.4.1. Cre-*loxP* system

The Cre-*loxP* system can be used to alter gene expression in a conditional manner. It requires a floxed gene and a Cre recombinase to excise the targeted genomic region. The Cre enzyme is a site-specific recombinase that recognizes a short DNA sequence called the *loxP* (locus of x-over, P1) site. The *loxP* site consists of two 13 base pairs (bp) palindromic repeats and 8 bp core sequences. Depending on the location and orientation of the *loxP* sites, the Cre mediated recombination can result in excision, inversion, or translocation of DNA. If the *loxP* sites are on the same DNA strand and have the same orientation, the sequence in-between gets excised or deleted (64).

To use the methodology for lineage or cell type-specific excision, Cre has to be expressed under the control of a cell-type-specific promoter. Apart from controlling Cre recombinase expression in a spatial manner, temporal control is also possible by Cre modification. To achieve Cre activation at a precise time, inducible systems have been developed. One of them – CreERT – is a tamoxifen-inducible Cre recombinase, where Cre is fused to the estrogen receptor containing a mutated ligand-binding domain. This mutation prevents the ability of the

endogeneous estrogen to bind to the receptor. With some modifications to the receptor, an improved version CreERT2 was generated (65). The CreERT2 is about ten times more sensitive to 4-hydroxytamoxifen than CreERT (66). CreERT2 is usually presented in the cytoplasm where it is bound to the heat shock protein 90 (Hsp90) (**Fig. 10A**). After tamoxifen (or 4-hydroxytamoxifen) administration, the interaction of Hsp90 with CreERT2 is disrupted and tamoxifen binds to CreERT2, which results in nuclear translocation of the CreERT2 complex (65). In the nucleus, Cre interacts with the *loxP* sites and excises the floxed sequence (**Fig. 10B**) (64).

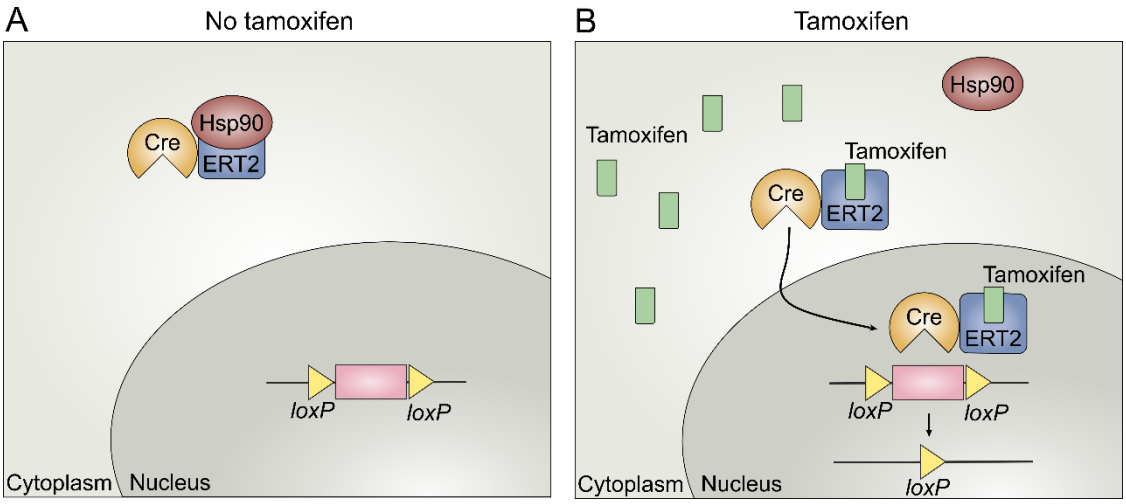

Fig. 10. Principle of the tamoxifen-inducible CreERT2-*loxP* system. (A) In the absence of tamoxifen, CreERT2 interacts with heat shock protein 90 (Hsp90) in the cytoplasm. **(B)** Upon tamoxifen administration, the interaction of Hsp90 with CreERT2 is disrupted. When tamoxifen is bound to CreERT2, the complex is translocated to the nucleus where Cre recognizes the *loxP* sites and excises the floxed sequence.

To assess the efficiency and specificity of the Cre-mediated recombination, Cre reporter mouse lines can be used (64). The ROSA$^{nT\text{-}nG}$ double-fluorescent Cre reporter mouse line expresses nuclear-localized red fluorescence (tdTomato) in cells prior to Cre recombinase exposure. Upon exposure of cells to Cre, nuclear-localized green fluorescence (EGFP) is observed (67).

1.4.2. *Pde6b*$^{STOP/STOP}$, *Pde6g*$^{CreERT2/+}$ mouse line

In this study, we used the CreERT2-*loxP* approach to control gene expression. Two *loxP* sites on either site of the STOP cassette were placed on both *Pde6b* alleles in intron 1 (*Pde6b*$^{STOP/STOP}$) (**Fig. 11A**). The STOP cassette is a transcription-inhibitor signal sequence that prevents the PDE6B expression (68). The disrupted expression of PDE6B is a frequent cause of autosomal recessive RP (69) and leads to rod photoreceptor degeneration. In addition to the disrupted expression, the floxed STOP cassette enables conditional gene activation in the presence of active CreERT2.

To take advantage of the conditional gene activation, the *Pde6b*$^{STOP/STOP}$ mice were crossed with *Pde6g*$^{CreERT2/+}$ mice. In the *Pde6g*$^{CreERT2/+}$ mice, exon 2 and 3 of the *Pde6g* gene were replaced by tamoxifen-inducible CreERT2 (70). The CreERT2 is under *Pde6g* locus control, a rod-specific promoter, which ensures that the CreERT2 is only expressed in rod photoreceptors.

In *Pde6b*$^{STOP/STOP}$, *Pde6g*$^{CreERT2/+}$ mutant mice that are not injected with tamoxifen (here referred to as untreated), the CreERT2 is inactive and the floxed STOP cassette prevents the PDE6B expression. Upon tamoxifen application (here referred to as treatment) in *Pde6b*$^{STOP/STOP}$, *Pde6g*$^{CreERT2/+}$ mice, the CreERT2 recombinase is activated, the STOP cassette is removed from the *Pde6b* gene, and the expression of PDE6B is restored (**Fig. 11B**) (70).

This *Pde6b*$^{STOP/STOP}$, *Pde6g*$^{CreERT2/+}$ mouse line has several advantages to study the effect of treatment on disease progression. First, the mouse model mimics the human RP disease progression including inner retinal remodeling and allows sufficient time for an intervention. Secondly, as the CreERT2-*loxP* system is used for activation of the *Pde6b* gene, PDE6B is restored in almost all rod photoreceptors and gives control over the number of treated cells. Moreover, as tamoxifen is injected intraperitoneally, an injury due to the injection into the eye (either by intravitreal or subretinal administration) is circumvented. Finally, after treatment, the expression level of the protein mimics the endogenous WT level in the targeted cells and thus provides a sufficient level for rescue.

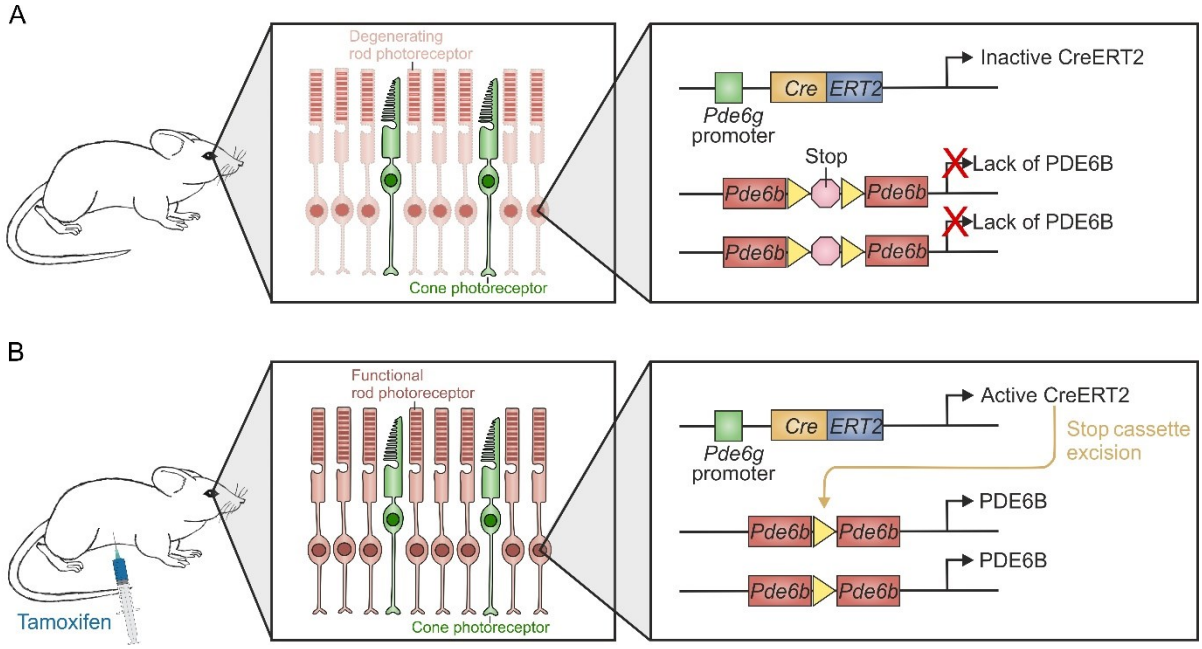

Fig. 11. *Pde6b*$^{STOP/STOP}$, *Pde6g*$^{CreERT2/+}$ mouse model. A floxed STOP cassette is inserted in intron 1 of the *Pde6b* gene. CreERT2 is expressed under the rod-specific *Pde6g* promoter. **(A)** In untreated mice, CreERT2 is inactive. The STOP cassette prevents the PDE6B expression which leads to rod photoreceptor degeneration. **(B)** After tamoxifen application, the CreERT2 gets activated, removes the STOP cassette, and restores the PDE6B expression.

2. Aim of the thesis

RP retinas are characterized by progressive photoreceptor cell death which is accompanied by several other pathological changes. For example, loss of rod bipolar processes, ectopic cell bodies, enlarged RPE cells and increased acellular capillaries. These structural alterations are known as remodeling. Since RP patients typically seek medical help after disease onset and, thus, during ongoing retinal degeneration and remodeling, it is crucial to determine the therapeutic time window.

This thesis aimed to 1) identify the threshold number of rod photoreceptors necessary for the long-term rescue of vision and 2) understand how the retina remodels during RP disease progression on a cellular level. Of special interest was if the progressive degeneration of the photoreceptors and the consequential remodeling of the inner retina (rod bipolar, cone bipolar, and horizontal cells), the RPE, and the retinal blood vessels, are plastic and whether these changes can be halted or even reversed by treatment.

The study was performed in the *Pde6b*$^{STOP/STOP}$, *Pde6g*$^{CreERT2/+}$ RP mouse model, with rescue induced at late disease stages by tamoxifen injection. To in-depth understand the structural underpinnings of remodeling and plasticity, an extensive morphological analysis of the retina from treated, untreated mutant, and wild type mice was performed. ERG measurements were used to study the retinal function. In addition, the Morris water maze was utilized to test whether the vision is restored after genetic rescue.

3. Material and methods

3.1. Material

3.1.1. Mouse line

All animal experiments were performed according to the ARVO statement for the use of animals in ophthalmic and vision research and were approved by the local authorities (Regierung von Oberbayern). Mice were kept under standard conditions under a 12-hour light/12-hour dark cycle with access to water and food *ad libitum.*

Pde6g^{CreERT2} and *Pde6b*^{STOP} mice were generated in the Barbara & Donald Jonas Stem Cells Laboratory, Columbia University, USA (68, 70, 71). Mice were rederived via *in vitro* fertilization at the Biomedical Center Munich, Germany. In our study we used mutant (*Pde6b*$^{STOP/STOP}$, *Pde6g*$^{CreERT2/+}$; referred to as *Pde6b*$^{STOP/STOP}$) and control mice (*Pde6b*$^{STOP/+}$, *Pde6g*$^{CreERT2/+}$; WT) of both sexes. CreERT2 was characterized in *Pde6b*$^{STOP/+}$, *Pde6g*$^{CreERT2/+}$, *ROSA*$^{nT\text{-}nG/+}$ mice. Primers and their annealing temperatures used for the PCR genotyping are given in **Table 1**. Some mice were also genotyped or sequenced for the absence of spontaneous mutations (rd1, rd8, cplf3).

Table 1. Primers used for genotyping and sequencing

Primer name	Forward primer (5`→3`)	Reverse primer (5`→3`)	Internal primer (5`→3`)	Annealing temperature [°C]
Pde6b^{Stop}	TGCTCTGTGGTGT TGCTCTGC	TGGCGATGCAGA GTGTCCTGA	GTCCTGCACGAC GCGAGCTG	65
Pde6g^{CreERT2}	GGTCAGATTCCAG TGTGTGGG	GTTTAGCTGGCCC AAATGTTG	CTTAGGTGGTCC TTTCCTGGG	65
ROSA$^{nT\text{-}nG}$	AAAGTCGCTCTGA GTTGTTAT	GGAGCGGGAGAA ATGGATATG	CCAGGCGGGCC ATTTACCGTAAG	60
Pde6g^{rd1}	ACCTGCATGTGAA CCCAGTATTCTAT C	CTACAGCCCCTCT CCAAGGTTTATAG	AAGCTAGCTGCA GTAACGCCATTT	65 and 60
Crb1^{rd8}	GGTGACCAATCTG TTGACAATCC	GCCCCATTTGCAC ACTGATGAC		58
Gnat2^{Cplf3}	CATCGAGACCAAG TTTTCTG	ACCATGTCGTAGG CACTGAG		58

3.1.2. Antibodies and lectins

Table 2. Primary antibodies, secondary antibodies, and lectins

Antibody/ lectin	Host species	Dilution	Manufacturer	Catalog number	Conjugate for secondary antibodies
Pde6b	Rabbit	1:4000	Thermo Fisher	PA1-722	
Cone arrestin	Rabbit	1:1000	Merck	AB15282	
Secretagogin	Rabbit	1:5000	A generous gift from Prof. Dr. Ludwig Wagner (University of Vienna, Austria)	(72)	
Rhodopsin (1D4)	Mouse	1:1000	Santa Cruz	sc-57432	
PKC–a (H-7)	Mouse	1:1000	Santa Cruz	sc-8393	
Calbindin D-28k	Mouse	1:8000	Swant	300	
ß-catenin	Rabbit	1:500	Cell Signaling Technology	8480S	
GFP	Goat	1:500	Biomol	600-101-215	
GARP, clone 4B1	Mouse	1:400	Sigma Aldrich	MABN2429	
Isolectin B4 conjugated FITC		1:100	Sigma Aldrich/ Merck	L2895	
488-Goat anti-rabbit	Goat	1:1000	Thermo Fischer	A-11070	Alexa Fluor 488
647-Goat anti-rabbit	Goat	1:1000	Thermo Fischer	A-21245	Alexa Fluor 647
555-Goat anti-mouse	Goat	1:1000	Thermo Fischer	A-21425	Alexa Fluor 555
647-Goat anti-mouse	Goat	1:1000	Thermo Fischer	A-21235	Alexa Fluor 647
488-Donkey anti-goat	Donkey	1:1000	Thermo Fischer	A-11055	Alexa Fluor 488

3.1.3. Chemicals

Table 3. Chemicals

Name	Supplier	Ordering number
100 bp DNA Ladder	Thermo Fisher Scientific	15628050
10X Blue Juice	Thermo Fisher Scientific	10816015

Acetic acid	Carl Roth	3738.4
Agarose	Carl Roth	3810.3
Aqua-Poly/Mount	Polysciences	18606
Circle Writer Liquid Blocker	Science Services GmbH	CWAL-FG
Corn oil	Sigma Aldrich/ Merk	C8267
D(+)-Saccharose	Carl Roth	4621.1
Dimethyl sulfoxide (DMSO)	Carl Roth	A994.1
dNTP Set	Thermo Fisher Scientific	10297018
DreamTaq DNA Polymerase	Thermo Fisher Scientific	EP0702
Ethanol > 99.5% (absolute)	Carl Roth	5054.1
H&E fast staining kit	Carl Roth	9194.1
H_2O_2	Carl Roth	9683.4
Hoechst 33342, Trihydrochloride, Trihydrate	Thermo Scientific	H1399
Isopropanol	Carl Roth	6752.2
KCl	Carl Roth	6781.3
Ketamin 10% (ketaminhydrochloride)	Bela-pharm GmbH & Co. KG	9089.01.00
KH_2PO_4	Carl Roth	3904.2
Methocel® 2% eyedrops	OmniVision GmbH	04682367
Mydriaticum Stulln eye drops (0.5% tropicamide-phenylephrine 2.5% eye drops)	Pharma Stulln	4647856
$Na_2EDTAx2H_20$	Sigma Aldrich / Merk	E1644-250G
Na_2HPO_4	Carl Roth	T876.1
NaCl	Carl Roth	3957.1
Neosynephrin-POS 10% eye drops	Ursapharm	828590
Paraformaldehyde	Carl Roth	0335.2
Proxylaz 20 mg/mL (xylazinhydrochloride)	Bela-pharm GmbH & Co. KG	3100408.00.00
SDS	Carl Roth	2326.1
SYBR™ Safe DNA Gel Stain	Thermo Fisher Scientific	SM0311
Tamoxifen free base	Sigma-Aldrich/Merck	T5648-1G
Tris HCl	Carl Roth	9090.3
Trisbase / Tris	Carl Roth	0188.1

Triton X 100	Carl Roth	3051.3
Triton® X-100	Carl Roth	3051.3
Trypsin (1:250)	Thermo Fisher Scientific	27250018

3.1.4. Consumables

Table 4. Consumables

Name	Supplier	Ordering number
0.2 ml 8-Strip 'Non-Flex' Natural PCR Tubes, Ind-Attached Flat Caps (Xtra-Clear)	Starlab	I1402-3700
24-Well plate	Greiner	662160
35 x 10 mm CytoOne® Dish, TC-Treated	Starlab	CC7682-3340
48-Well CytoOne® Plate, TC-Treated	Starlab	CC7682-7548
Chemiblocker	Merck Millipore	2170
Circle Writer Liquid Blocker	Science Services GmbH	CWAL-FG
Coverslips Thickness: 1, 24 x 60 mm	Carl Roth	H878.2
Disposable needles Sterican® long bevel facet, 40 mm, 0.80 mm, green	Carl Roth	X127.1
OMNICAN 50 0.5ML 0.30X8MM	NeoLab	9151117
Parafilm® Sealing Film	Starlab	I3080-1038
Rosco Supergel 27, Medium Red	Lightpower GmbH	74027
SafeSeal reaction tube, 1.5 ml	Sarstedt	72706
SafeSeal reaction tube, 2.5 ml	Sarstedt	72695500
SafeSeal reaction tube, 5 ml	Sarstedt	72701
Scalpel	NeoLab	294200101
Screw cap tube, 15 ml	Sarstedt	62554502
Screw cap tube, 50 ml	Sarstedt	62559001
STERICAN G30 0.30X12MM	Neolab	194211012
X2 NEG 50	Fisher Scientific	11912365
X72 Superfrost® Plus slides	Thermo Scientific	10149870

3.1.5. Buffers and solutions

Table 5. Buffers and solutions

Name	Composition
4% paraformaldehyde (PFA)	6 g PFA ad 150 mL 1X PBS
1X TAE	10 mL 50X TAE ad 500 mL ddH_20
50X TAE	242 g tris base 57.1 mL acetic acid 37.2 g $Na_2EDTAx2H_20$ ad 1 L ddH_20
10X PBS	11.75 g Na_2HPO_4 2 g KH_2PO_4 80 g NaCl 2 g KCl ad 1 L ddH_20
1X PBS	100 mL 10X PBS ad 900 mL ddH_20 adjust pH = 7.4
30% sucrose	150 g D(+)-Saccharose ad 500 mL ddH_20
0.1 M tris	6.057 g tris base ad 500 mL ddH20 pH = 7.8
3% trypsin	0.6 g trypsin ad 20 mL 0.1 M tris (pH = 7.8)
Hoechst 50 mg/mL	100 mg Hoechst 33342 ad 2000 µL ddH_20
Hoechst solution	5 µL 50 mg/mL Hoechst ad 50 mL 1X PBS
100 bp DNA ladder	100 µL 10X Blue Juice 100 µL 100 bp DNA ladder Invitrogen 400 µL ddH_20
50 mM NaOH	2 g NaOH ad 1 L ddH_20
1 M tris	24.23 g tris ad 200 mL ddH_20 adjust pH = 8.0
10% Triton X-100	1 mL Triton X-100 9 mL PBS

3.1.6. Instruments

Table 6. Instruments

Name	Supplier
Agarose gel chamber	Danaphore
Centrifuge 5415 R	Eppendorf
ChemiDoc XRS+ system	Bio-Rad
Corning® LSE™ 6770 Mini Mikrozentrifuge	Omnilab
Cryostat CM3050 S	Leica
Custom-made VisiScope CSU-X1 confocal system equipped with a high-resolution sCMOS camera	Visitron Systems
Espion ERG Diagnosys equipment	Diagnosys LLC
Heating mat	Trixie
KEYENCE BZ-X800	Keyence
Kleinfeld Vortex Genie® 2 Mixer	Omnilab
Leica TCS SP8	Leica
Mastercycler® nexus X2	Eppendorf
pH meter Lab 850	Schott Instruments
SZ51 KL 300 (Dissection microscope)	Olympus
ThermoMixer® C	Eppendorf
WM Video Mot2	TSe Systems
Zeiss LSM 710	Zeiss

3.1.7. Software

Table 7. Software

Name
ImageJ
Cell Profiler 3.1.9
GraphPad Prism 8
CorelDRAW 2018

3.2. Methods

3.2.1. Genotyping

To isolate the DNA, ear punches were lysed in 600 µL 50 mM NaOH. After boiling at 95°C for 10 minutes, 50 µL of 1 M tris HCl was added and vortexed. After 6 minutes of centrifugation at room temperature, the supernatant was transferred to a new tube and stored at 4°C. The polymerase chain reactions (PCRs) were performed on the Mastercycler® nexus X2. Master mix components (**Table 8)** without the DNA template were mixed and transferred to 0.2 ml 8-Strip PCR tubes, where DNA was added to each tube. Primers and their annealing temperatures used for genotyping are given in **Table 1**. The PCR conditions are given in **Tables 9 - 13.**

Table 8. Master mix components for genotyping

	Crb1^{Rd8} and Gnat2^{Cplf3}	Pde6b^{rd1} and Pde6g^{CreERT2}	ROSA$^{nT\text{-}nG}$ and PDE6b^{STOP}
10X Dreamtaq mix	1.50	2.50	1.50
dNTPs	0.50	0.50	0.50
10µM Forward primer	1.25	1.00	1.25
10µM Reverse primer	1.25	1.00	1.25
10µM Intermediate primer	/	1.00	1.25
DNA template	1.00	3.00	1.00
PCR grade water	9.38	15.70	8.13
Dream Taq	0.13	0.30	0.13
Total volume:	15.00	25.00	15.00

Table 9. Thermocycling conditions for amplification using Pde6b^{STOP} primers

Step	Temperature [°C]	Duration	Cycles
Initial denaturation	95	3 min	1
Denaturation	95	30 sec	
Annealing	65	30 sec	30
Extension	72	1 min	
Final extension	72	10 min	1
	10	hold	

Table 10. Thermocycling conditions for amplification using Crb1^{rd8} and Gnat2^{cplf3} primers

Step	Temperature [°C]	Duration	Cycles
Initial denaturation	95	3 min	1
Denaturation	95	30 sec	
Annealing	58	30 sec	30
Extension	72	1 min	
Final extension	72	10 min	1
	10	hold	

Table 11. Thermocycling conditions for amplification using ROSA$^{nT\text{-}nG}$ primers

Step	Temperature [°C]	Duration	Cycles
Initial denaturation	95	3 min	1
Denaturation	95	30 sec	
Annealing	60	30 sec	30
Extension	72	1 min	
Final extension	72	10 min	1
	10	hold	

Table 12. Thermocycling conditions for amplification using Pde6b^{rd1} primers

Step	Temperature [°C]	Duration	Cycles
Initial denaturation	94	2 min	1
Denaturation	95	20 sec	
Annealing	65	15 sec	10
Extension	68	10 sec	
Denaturation	94	15 sec	
Annealing	60	15 sec	28
Extension	72	15 sec	
Final extension	72	2 min	1
	10	hold	

Table 13. Thermocycling conditions for amplification using Pde6b^{CreERT2} primers

Step	Temperature [°C]	Duration	Cycles
Initial denaturation	95	3 min	1
Denaturation	95	30 sec	
Annealing	65	30 sec	40
Extension	72	1 min	
Final extension	72	10 min	1
	10	hold	

To separate the DNA PCR products by size, agarose gel electrophoresis was carried out. For this, 1% agarose gel was prepared by dissolving agarose in 1X TAE in the microwave. When the agarose solution was cooled down to about 50°C, 5 µL Sybr Safe was added to 100 µL of solution and poured into a gel tray with a comb in place. After the gel was solidified, the chamber was filled with 1X TAE and 100 bp DNA Ladder, and samples were loaded. The gel

was run at 80 V for 15 minutes. The DNA fragments were visualized using ChemiDoc XRS+ system. The product lengths can be found in **Table 14**.

Table 14. Product length for the combination of PCR primers.

	$Pde6b^{STOP}$	$Pde6b^{CreERT2}$	$ROSA^{nT\text{-}nG}$	$Pde6b^{rd1}$
WT lane [bp]	284	514	603	240
Mutant lane [bp]	415	715	320	560

The samples for the spontaneous point mutations $Crb1^{Rd8}$ and $Gnat2^{Cplf3}$ were not run on the gel after the PCR reaction but were sent for sequencing. For this, 2 µl of the 10 µM primer solution was added to 15 µL of the PCR reaction and sent to Eurofins. The sequence was aligned to the sequence where the mutation can be found. The rd8 of the *Crb1* gene is a single base deletion at nt3481 in exon 9 and its WT sequence is AGCTACAGTTCTTAT**C**GGTGTGCCTGTC (73). The absence of single-base substitution at position 598 in exon 6 (G->A) in the *GNAT2* gene named *cpfl3* was confirmed by the presence of the WT sequence GATGTTT**G**ATGTGGGA (74).

3.2.2. Tamoxifen treatment

Tamoxifen was weighted into an empty 1.5 mL tube and absolute ethanol was added to a concentration of 100 mg/mL. The solution was sonicated for 15 minutes, mixed, and sonicated again for 15 minutes to dissolve the tamoxifen completely. The solution was further diluted in corn oil to a stock solution of 10 mg/mL in a vial that was wrapped in aluminum foil. The stock solution was aspirated into an insulin syringe. The mice were intraperitoneally injected at a concentration of 100 µg/g body weight on two consecutive days (1 injection/day).

3.2.3. Tissue preparation

After the mice were euthanized, the temporal side of their eyes was marked with a hot cannula (**Fig. 12**; Step 1). For eyes enucleation, spring scissors that were slightly curved upwards were used. The preparation was made under a stereo microscope Olympus SZ51 in a 35 mm dissection dish. A hole was made with a cannula at *ora serrata* and submerged into 4% paraformaldehyde (PFA) for 5 minutes (**Fig. 12**; Step 2). A small incision at the burn mark, perpendicular to and just above the limbus was made to preserve the information about the orientation of the eye. After a circular cut was made above the *ora serrata* with small scissors

(**Fig. 12**; Step 3), the anterior segments, lens, and vitreous were removed (**Fig. 12**; Step 4). The eyecups were fixed in 4% PFA in phosphate-buffered saline (PBS) for 45 minutes. The eyecup was rinsed 3 times in PBS and was ready prepared for further steps for cryopreserving and sectioning.

To prepare retinal or RPE-choroid-sclera flat-mounts, the tissue outside the sclera was removed (**Fig. 12**; Step 5). Then forceps were positioned between the retina and the eyecup and moved slowly around the circumference to loosen the retina from the RPE (**Fig. 12**; Step 6). The eyecup was dissected into quarters (**Fig. 12**; Step 7) and the retina separated from the RPE-choroid-sclera flat-mount (**Fig. 12**; Step 8). Four additional incisions were made in the RPE-choroid-sclera flat-mount.

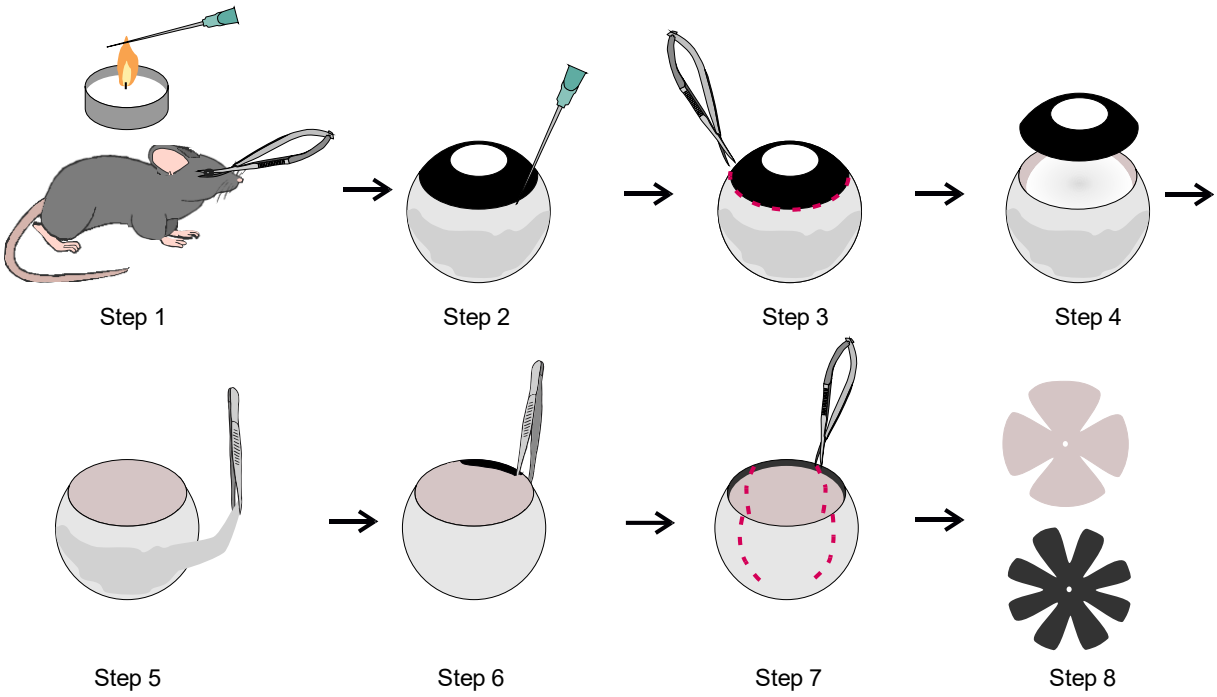

Fig. 12. Schematic step-by-step preparation of the eye for cryosections, retinal, and RPE-choroid-sclera flat-mounts. After the mouse was euthanized, eyes were marked temporally with a hot cannula and enucleated (Step 1). A puncture was made into the eye with a needle (Step 2) and placed into 4% PFA. After 5 minutes, a circular path along the *ora serrata* was cut (Step 3). After the lens and the vitreous were pulled out (Step 4), the preparation for cryosections was finished. For retinal and RPE-choroid-sclera flat-mounts, the tissue outside the sclera was removed (Step 5) and the retina was detached from the RPE with forceps (Step 6). Radial incisions were made (Step 7) and the retina and RPE-choroid flat-mount were separated (Step 8).

3.2.4. Retinal cryosections

For retinal cryosections, eyecups were washed 3 times in PBS and cryoprotected overnight in 30% sucrose so that the eyeball settled to the bottom of the well. The excess sucrose solution was removed by using a tissue. The eyeball was positioned with the eyecup facing up in a hand-made cup out of aluminum foil filled with Tissue-Tek® O.C.T.™ compound (Sakura). Parallel to the small incision on the temporal side of the eyeball, a mark was drawn on the outside of the aluminum cup to retain the orientation of the eye. The eyecup was meticulously orientated in the aluminum cup, frozen on dry ice, and stored at -80°C until the eyes were sectioned. Before cutting, a mark on the temporal side was made onto the frozen block and the aluminum foil was removed completely. The block in dorso-ventral orientation was sectioned at 10 µm using the Leica Cryostat CM3050 S. Retinal sections were carefully collected on SuperFrost Plus™ slides that were annotated and numbered. Six sections were collected on each slide. Sections were collected on one slide briefly before the optic nerve, all sections through the optic, and one slide after the optic nerve. The sections were stored at -20°C until they were used for immunohistochemical staining.

3.2.5. Immunohistochemistry of retinal sections

For staining, retinal sections were thawed, encircled with a writer liquid blocker, washed with PBS, and incubated overnight at 4°C in primary antibodies (**Table 2**) in PBS containing 5% Chemiblocker and 0.3% Triton® X-100. Subsequently, sections were washed in PBS (3x) and incubated with secondary antibodies (**Table 2**) in PBS containing 3% Chemiblocker for 2 hours at room temperature. For nuclear counterstaining, sections were incubated for 5 minutes in 5 µg/ml Hoechst 33342, then washed again with PBS. After washing, as much of the PBS was removed by gently shaking the slide. A drop anti-fading Aqua-Poly/Mount mounting media was added to each section and the slide was covered with a coverslip. It was allowed to harden overnight at room temperature in the dark. The slides were stored at 4°C indefinitely.

3.2.6. Immunohistochemistry of flat-mounts and RPE preparations

For flat-mounted retinal and RPE-choroid-sclera preparations, eyecups were washed in PBS (3x). The retina was removed from the RPE-choroid-sclera. The RPE-choroid-sclera preparations were bleached in 10% H_2O_2 at 55°C for 1.5 hours in a ThermoMixer® C. The retinal and RPE-choroid-sclera flat-mounts were then washed 3 times in PBS and incubated two nights at 4°C in primary antibodies (**Table 2**) in PBS containing 3% DMSO, 0.5% Triton X-100, and 5% Chemiblocker. Subsequently, the flat-mounts were washed with PBS and

incubated for 2 hours at room temperature with secondary antibodies (**Table 2**) in PBS containing 3% Chemiblocker. After washing the flat-mounts 3 times, nuclear counterstaining was carried out. For this, flat-mounts were incubated for 10 minutes with Hoechst 33342, then washed again with PBS and mounted on SuperFrost Plus™ slides. To do so a glass pipet was used to transfer the flat-mounts into the slide. The flat-mounts were then gently unfolded with forceps and as much liquid as possible removed with a tissue. Aqua-Poly/Mount media was covered used for mounting. The slides were allowed to harden overnight at room temperature in the dark. The slides were stored at 4°C indefinitely.

3.2.7. Imaging of the fluorescent stains

RPE-preparations, retinal cryosections, and flat-mounts were imaged at the laser-scanning confocal Zeiss LSM710, Leica TCS SP8, or custom-made VisiScope CSU-X1 confocal system equipped with a high-resolution sCMOS camera (Visitron Systems, Puchheim, Germany). For some quantitative analysis, images were taken at KEYENCE BZ-X800.

3.2.8. RPE morphometry

RPE-choroid-sclera flat-mounts were stained for ß-catenin. Images were acquired with a confocal microscope using a 40× oil objective in three regions of the flat-mount: central, equatorial, and peripheral (**Fig. 13A**) (75). After adjusting contrast and brightness in ImageJ, areas of equal size were used for the automatic morphometric measurements in CellProfiler (76). Not accurately segmented individual RPE cells were manually excluded from the analysis.

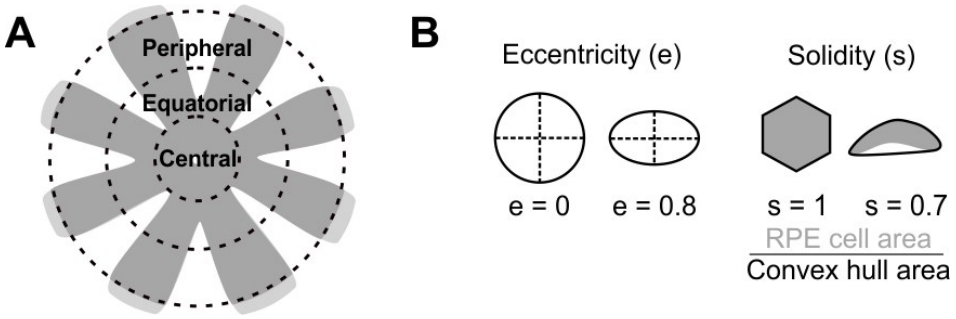

Fig. 13. Morphometric analysis of the RPE. (A) Images for the quantification were taken from the central, equatorial, and peripheral regions. **(B)** Parameters eccentricity and solidity were quantified.

Size parameter cell area, as well as shape parameters eccentricity and solidity were examined. Eccentricity shows how elongated a cell is. A perfect circle has an eccentricity value of 0, while an ellipse has a smaller eccentricity value (**Fig 14B**; left). Solidity is defined as the RPE cell area divided by the convex hull area. A hexagonal /pentagonal cell has the solidity of 1, lower values cells that are more concave (**Fig 14B**; right). The values for the three morphometric parameters of the RPE cells from each image were distributed over the selected three intervals and the mean (± SEM) percent of the RPE for each group was plotted. The values of the cell area of RPE cells were divided into RPE cells that were smaller than 150 μm², between 150 and 699 μm², and equal or greater than 700 μm². The eccentricity values of RPE cells were divided into intervals of less than 0.5, between 0.5 and 0.79, and with the solidity of greater equal to 0.8. The solidity values of RPE cells were divided into RPE cells with the solidity smaller than 0.85, between 0.85 and 0.92, and with the solidity equal or greater than 0.93. **Table 15** shows the number of mice in different groups of ages and genotypes.

Table 15. Number of mice for the RPE morphometric analysis

Region\ Group	Mutant pw16	Mutant pw24	Mutant pw40	Treated pw16/40	Treated pw24/40	WT pw40
Central	5	5	5	5	6	6
Equatorial	6	5	5	4	6	5
Peripheral	5	6	8	4	5	5

3.2.9. Retinal vessel area quantification

Retinal flat-mounts labeled with isolectin GS-IB4 conjugated FITC were scanned in z-stack mode (1 μm steps) from the top to the bottom layer in up to three regions in the center and periphery. Maximum intensity projections were made in ImageJ of the merged deep and intermediate vascular plexus (DVP + IVP) and for superficial vascular plexus (SVP). AngioTool software was used to quantify the percent vessel density (University of Warwick, UK) (77). AngioTool software allows a semi-automated detection of vessels. The vessel selection is shown by a yellow overlay on the image. By adjusting the analysis parameters vessel diameter, vessel intensity, removing small particles, and filling holes the software allows the user to best match the overlay with the vessels (**Fig 14**).

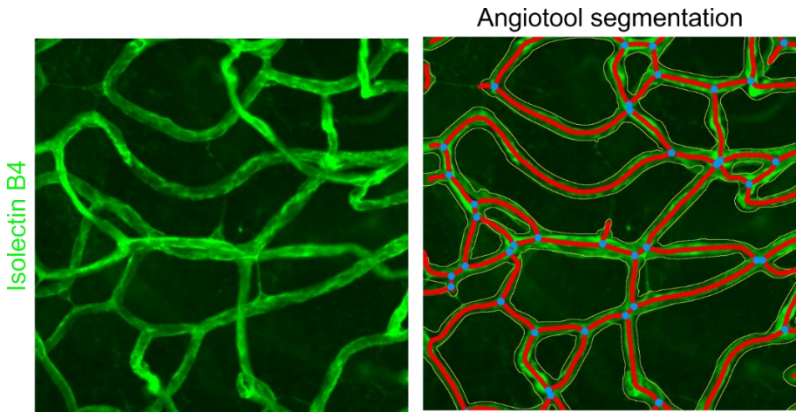

Fig. 14. Analysis of retinal blood vessels using AngioTool. A representative image before (left) and after (right) the analysis. The vessels are outlined in yellow, the skeleton representation of vasculature is marked red and branching points are blue.

3.2.10. Trypsin digestion and H&E staining

Trypsin digest is a method to analyze the retinal vasculature that is later stained with hematoxylin and eosin (H&E). For this, retinas were digested using trypsin as previously described with slight modifications (78). Briefly, after enucleation, a hole was made with a cannula at *ora serrata* and the eyecup was fixated in 4% PFA for 5 minutes. After a circular cut was made above the *ora serrata* (**Fig. 12**; Step 3), the anterior segments, lens, and vitreous were removed (**Fig. 12**; Step 4) and eyecups were further fixed in 4% PFA in PBS for 45 minutes. Forceps were then positioned between the retina and the eyecup and moved slowly around the circumference to loosen the retina from the RPE-choroid-sclera. The intact retina was isolated and further fixed in 4% PFA overnight. The next day, the retinas were washed (5x) with distilled water, with a minimum of 30 minutes between the washing steps. After overnight shaking in water at room temperature, retinas were transferred into 24-well plates and incubated in 3% trypsin in 0.1 M tris buffer at 37°C for 90 minutes. The inner limiting membrane was removed with scissors and then the vasculature was isolated by several washing steps by pipetting water up and down adjacent to vessels under the microscope. Washes were completed when little to no debris was present in the water. The digested vessels were transferred with a glass pipette onto SuperFrost Plus™ slides. When the vessels were unfolded, the vasculature was allowed to dry at 37°C overnight.

On the next day, the vasculature network was stained with an H&E fast staining kit. The staining protocol provided by the manufacturer was adjusted. First, the slides with the vasculature network were immerged in hydrochloric solution (pH = 4.3) for 10 seconds. Then the slides were incubated in H&E solution 1 for 8 minutes. After that, the slides were washed in hydrochloric solution (pH = 4.3) for 10 seconds and differentiated with hydrochloric acid

0.1% for 20 seconds. The blueing was performed by rinsing the vasculature with flowing tap water for 6 minutes, followed by an incubation in the H&E solution 2 for 5 minutes. The slides were rinsed in flowing tap water for 30 seconds and dried at room temperature overnight. Finally, the slides were mounted with Aqua-Poly/Mount media.

Microscopy was performed at the Core Facility Bioimaging of the Biomedical Center at the LMU with a Leica DM6 FS microscope. Bright-field images were recorded with a Leica DMC2900 CMOS camera with an image pixel size of 145 nm. A 20x/0.8 objective was used for quantification and overview image of the network and a 40x/0.95 objective for a detailed view of the vascular network.

3.2.11. Quantitative analysis of acellular capillaries

Acellular capillaries were manually counted using ImageJ software. For each animal, up to 5 areas of 0.06 mm² each were counted. Acellular capillaries were detected as vessel tubes without nuclei. N numbers for WT mice were 3, 6, 4, and 9 at the age of 16, 24, 30, and 40 weeks, respectively. N numbers for mutant mice were 4, 6, 2, and 7 at the age of 16, 24, 30, and 40 weeks, respectively. N numbers for 40-weeks-old mice treated at 12, 16, or 24 weeks were 5, 3, and 4, respectively.

3.2.12. Quantitative analysis of ONL thickness and rod photoreceptor number

The retinal cryosections were stained against cone arrestin and counterstained with Hoechst 33342. Images were taken in the central area of the retina (up to 3 sections per eye). Using ImageJ, the ONL thickness was measured 250 µm from the optic nerve on the ventral side of the eye. The N numbers for mutant retinas were 4, 6, 6, 4, 7, 3, and 8 for 4, 8, 12, 16, 24, 30, and 40-weeks-old mice, respectively. The N numbers for WT retinas were 3, 4, 3, 6, 2, 3, and 8 for 4, 8, 12, 16, 24, 30, and 40-weeks-old mice, respectively. The N numbers for 40-weeks-old mice treated at 4, 12, 16, and 24 weeks were 4, 4, 3, and 3, respectively. ONL thickness (Y) values of mutant animals were fit to a one-phase exponential decay model (79):

$$Y = y_o \cdot e^{(-k \cdot X)}.$$

Here, the variable X is the age in weeks, the symbol k is the rate constant for ONL thickness loss and y_o is the preexponential coefficient.

Rod numbers were determined by counting Hoechst-labeled nuclei in the ONL and subtracting the number of cones (ie, arrestin-positive cells). For this, images were taken in the central area of the retina in up to 2 sections per eye. Using ImageJ, a 75 µm wide rectangle ONL was selected 250 µm from the optic nerve on the ventral side of the retina, and the photoreceptor

number in this rectangle was quantified. Photoreceptors were counted in mutant retinas at 12, 16, 24, and 40 weeks of age (N = 5, 5, 4, and 4, respectively). Photoreceptors were counted in treated retinas at 12, 16, and 24 weeks of age (N = 4, 4, and 4, respectively). The rod photoreceptor number was normalized to 40-weeks-old WT mice (N = 4, mean ± SEM rod number: 210.4 ± 5.9).

3.2.13. Quantitative analysis of rod and cone bipolar cell dendrites

The quantification of rod and cone bipolar cells was performed on retinal sections. For this, retinal sections were labeled with the antibodies against protein kinase C-alpha (PKC–α) or secretagogin (SCGN) to label the rod or cone bipolar cells, respectively, and co-stained with Hoechst. Images were taken with 40x objective with the same laser power for all animals in the central area of the ventral retina. The quantification of the dendrite area was performed in ImageJ. First, the images were rotated in order to orient the ONL horizontally. Then the ONL and INL of 75 µm width were selected and saved as a new image. The dendrite area was selected so that a line was drawn above the cell bodies in the INL. The selected area with the staining of the dendrites was binarized with the same threshold on all images and the area of pixels above the threshold was analyzed. For each animal up to two retinal sections were analyzed and the area averaged. Dendrite area of rod bipolar cells and number of misplaced PKC-a positive cell bodies was quantified in 5 40-weeks-old WT mice, and in 5, 4, and 4 mutant mice at 16, 24, and 40 weeks of age, respectively. Dendrite area of rod bipolar cells and number of misplaced PKC-a positive cell bodies in 40-weeks-old mice treated at 12, 16, and 24 weeks of age was quantified in 4 mice in each group. The dendrite area of cone bipolar cells was quantified in 5 40-weeks-old WT mice, and 4 40-weeks-old mutant mice.

3.2.14. Quantitative analysis of horizontal cell processes

The quantification of horizontal cell processes was performed on retinal sections. For this, retinal sections were labeled with the antibodies against calbindin D-28k and costained with Hoechst. Images were taken with 40x objective with the same laser power for all animals in the central area of the ventral retina. The quantification of the processes was performed in ImageJ. First, the images were rotated in order to orient the ONL horizontally. Then the ONL and INL of 150 µm width were selected and saved as a new image. The area of the horizontal cell processes was selected so that a line was drawn to exclude the labeled horizontal cell bodies. The selected area with the staining of the processes was binarized with the same threshold on all images and the area of pixels above the threshold was analyzed. For each animal up to two retinal sections were analyzed and the area averaged. Dendrite area of cone

bipolar cells was quantified in 4 WT mice aged 40-weeks-old, and in 3, 5, 4, and 4 mutant mice at 12, 16, 24, and 40 weeks of age, respectively. Dendrite area of cone bipolar cells was quantified in 40-weeks-old mice treated at 12, 16, and 24 weeks of age in 3, 4, and 4 mice, respectively.

3.2.15. Electroretinogram recordings

The ERG is an electrophysiological tool that measures the electrical activity of the retina in response to a light stimulus. Before the measurements, animals were dark-adapted overnight. All handling on the day of the measurement was carried out under dim red light (used red filter: Rosco Supergel 27, Medium Red, #10273) (80). Mice were anesthetized by an intraperitoneal injection of 0.1 mL/10 g body weight of anesthetic solution (1 mL of 100 mg/mL ketamine, 0.1 mL of 20 mg/mL xylazine, and 8.9 mL of PBS). Pupils were dilated by one drop of 0.5% tropicamide (Mydriaticum Stulln 0.5%) and 5% phenylephrine hydrochloride (Neosynephrin-POS 5%). During measurements, the corneal hydration was ensured by application of hypromellose (Methocel® 2%), and golden loop electrodes were placed on each cornea. Body temperature was maintained at 37°C using a heating pad. ERG responses were recorded simultaneously from both eyes using an Espion E3 console in conjunction with the Color Dome. Scotopic electroretinograms were recorded at white light flash intensities of -3, -2, -1.5, -1.0, 0.5 and 1.0 log (cd·s/m²) (except for mice treated at 12 weeks, where intensities were -3 and 0.5 log (cd·s/m²)). For photopic measurements, mice were adapted for 10 min to a background of white light at an intensity of 30 cd/m^2 to suppress the rods, and then recordings were continued at white light intensities of -0.5, 0, 0.5, 1, and 1.5 log (cd·s/m²) (except for the for mice treated at 12 weeks, where the measurements were performed at intensities of 1.5 log (cd·s/m²)). A-wave amplitudes were measured from the baseline to the peak of the negative a-wave (baseline to trough), b-wave amplitudes were measured from the trough of the a-wave to the peak of the positive b-wave (**Fig. 15**). If the a-wave was missing, the b-wave was measured from the baseline to the peak of the b-wave. For each animal, the mean response of both eyes was averaged. Data were analyzed using a two-way analysis of variance (ANOVA).

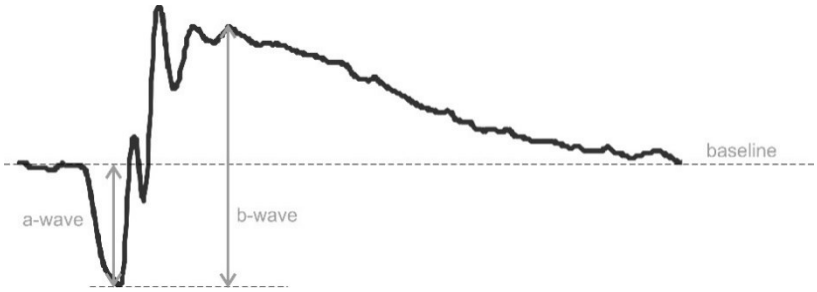

Fig. 15. Representative ERG response. The a-wave amplitude was measured from the baseline to the trough of the a-wave. The b-wave was measured from the trough of the a-wave to the peak of the b-wave.

3.2.16. Morris water maze

The Morris water maze task is a behavioral procedure that was conducted to assess visual function under dim light conditions (5.54 mW/cm² at 508 nm at the water level; measured with Nova II laser power/energy monitor and the PD300 photodiode head, Ophir Optronics LD). The setup consisted of a circular pool with a diameter of 160 cm filled halfway with 24-26°C warm water (**Fig. 16**). The pool was divided into imaginary quadrants and the platform of 10 cm in diameter submerged approximately 1.5 cm under water in the middle of the northern target quadrant. The pool was surrounded by distal cues and a camera with VideoMot2 software was used for tracking. Mice must learn to use distal cues to navigate to the hidden platform when started from different locations around the perimeter of the tank. The navigational task utilizes the averseness of water in motivating the mice to learn and find the escape platform rapidly. Mice were gently put into the water on different starting positions (**Table 16**) facing the wall and had to locate the platform. The mouse was given 60 seconds to find the platform. If the mouse failed to find the platform within 60 seconds, it was gently guided to the platform with a stick. Mice were allowed to remain 15 seconds on the platform before being returned to their cage. Mice were tested in eight trials per day for five consecutive days. Parameters escape latency (time for the animal to find the platform) and total swim path were analyzed.
On the fifth day after the last trial, the escape platform was removed from the tank. In this probe trial, mice were let 60 seconds to swim around and search for the platform. Time spent in each quadrant during a single trial was measured and the percent of occupancy for each quadrant was calculated and compared to the target quadrant. Representative paths were converted from raster to vector with CorelDRAW.

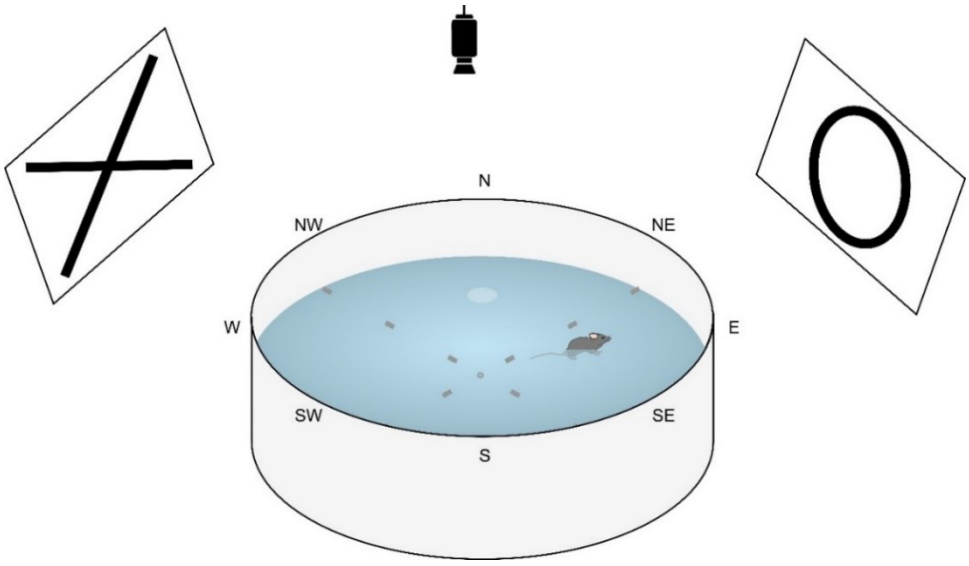

Fig. 16. Schematic drawing of the Morris water maze setup. A circular pool filled with water is surrounded by distal clues and equipped with a platform that is placed into the center of the imaginary target quadrant. The mouse learns to escape from the water by locating the platform. Its movements are tracked with a camera.

Table 16. Morris water maze spatial (hidden platform) start positions for days 1-5

Day\Trial	I	II	III	IV	V	VI	VII	VIII
1	SO	W	O	SW	W2	O2	S	SO2
2	SW	O	W	SO	O2	W2	S	SO2
3	W	SO	O	SW	SO2	S	W2	O2
4	O	SW	SO	W	SO2	W2	O2	S
5	SW	O	W	SO	S	W2	SO2	O2

3.2.17. Statistical analysis

Data are expressed as mean ± standard error of the mean (SEM). The N values refer to the number of individual animals. All data were analyzed in GraphPad Prism 5.0 software (La Jolla, CA, USA), using two-way ANOVA or t-test; $P \leq 0.05$ was considered statistically significant (* $P \leq 0.05$; ** $P \leq 0.01$; *** $P \leq 0.001$). To compare multiple groups, we used Tukey's or Sidak's multiple comparison test and reported adjusted *P*-values.

4. Results

4.1. Characterization of an inducible rod-specific Cre driver

In this study, we used an inducible rod-specific Cre mouse line (*Pde6g*$^{CreERT2/+}$), which contains tamoxifen-dependent CreERT2 in one allele of the *Pde6g* gene (70). To quantify the recombination efficiency, *Pde6g*$^{CreERT2/+}$ were crossed with *ROSA*$^{nT\text{-}nG/+}$ reporter mice (*Pde6g*$^{CreERT2/+}$, *ROSA*$^{nT\text{-}nG/+}$). These mice were tamoxifen injected at 4 weeks of age, sacrificed at 8 weeks of age, and EGFP and tdTomato positive cell nuclei were quantified using retinal sections (**Fig. 17A**). The analysis revealed a recombination rate of 93.4% ± 3.0% in rod photoreceptors.

To analyze tamoxifen-dependent recombination, retinas from 8-week-old untreated *Pde6g*$^{CreERT2/+}$, *ROSA*$^{nT\text{-}nG/+}$ mice were analyzed for the number of recombined cells. The percentage of EGFP positive cells in the rod photoreceptors was 10.0% ± 1.9% (**Fig. 17B**).

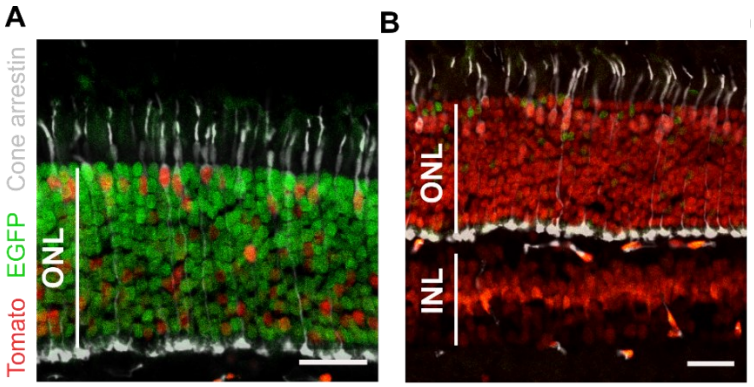

Fig. 17. The rod-specific Cre line exhibits high recombination after tamoxifen injections and low tamoxifen-independent recombination. *Pde6g*$^{CreERT2/+}$, ROSA$^{nT-nG/+}$ mice were treated at 4 weeks of age (or not) and sacrificed at 8 weeks. Retinal sections were labeled with anti-GFP antibodies and counterstained with Hoechst. **(A)** Representative image of an 8-week-old mouse retina that was treated at 4 weeks of age. **(B)** Representative image of an 8-week-old mouse retina in absence of tamoxifen. In the Cre-naïve state, the nuclei of cells express tdTomato (red), after CreERT2 recombinase exposure EGFP (green) is expressed. Vertical white bars, outer nuclear layer (ONL), and inner nuclear layer (INL). Scale bars, 25 µm.

4.2. Restoration of PDE6B after treatment

To use an RP gene therapy mouse model, we crossed the *Pde6g*$^{CreERT2/+}$ mice with the *Pde6b*$^{STOP/STOP}$ RP mouse line (**Fig. 11**). The *Pde6b*$^{STOP/STOP}$ mice contain a floxed STOP cassette in both alleles of the *Pde6b* gene. To demonstrate that *Pde6g*$^{CreERT2/+}$ can remove the floxed STOP cassettes and restore the PDE6B expression, we treated *Pde6b*$^{STOP/STOP}$, *Pde6g*$^{CreERT2/+}$ mutant mice with tamoxifen and immunostained retinal sections for PDE6B. In 40-weeks-old *Pde6b*$^{STOP/+}$, *Pde6g*$^{CreERT2/+}$ control mice (*Pde6b*$^{STOP/+}$, WT), PDE6B is expressed in outer segments. Untreated *Pde6b*$^{STOP/STOP}$, *Pde6g*$^{CreERT2/+}$ mice (*Pde6b*$^{STOP/STOP}$, mutant) at 4 weeks of age lack PDE6B expression due to the STOP cassette in the *Pde6b* gene. In some animals, we observed residual PDE6B expression. In 40-weeks-old *Pde6b*$^{STOP/STOP}$ mice that were treated at 4 weeks of age, PDE6B expression was detected in the outer segments (**Fig. 18)**.

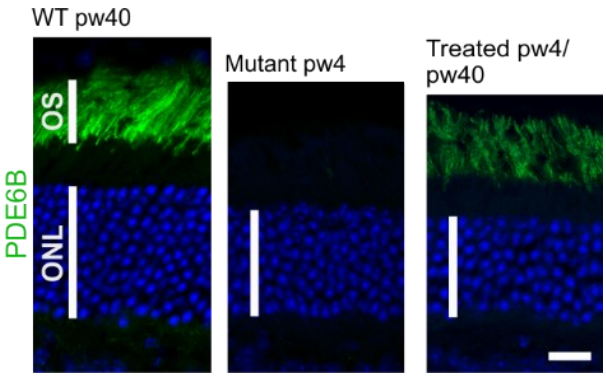

Fig. 18. Restoration of PDE6B expression in treated *Pde6b*$^{STOP/STOP}$ mice. PDE6B (green) is expressed in outer segments in 40-weeks-old Pde6b$^{STOP/+}$ (WT) mice, absent in 4-weeks-old untreated Pde6b$^{STOP/STOP}$ mice (mutant) and restored in tamoxifen-injected Pde6b$^{STOP/STOP}$ (treated) mice. Mice were treated at 4 weeks of age and sacrificed at 40 weeks of age. Vertical white bars, outer nuclear layer (ONL), and outer segments (OS). Scale bar, 15 µm.

4.3. Photoreceptor degeneration is halted by treatment at 16 weeks of age or earlier

To first gain an understanding of disease progression in our *Pde6b*$^{STOP/STOP}$ mouse model, progressive photoreceptor degeneration was evaluated as the thickness of the outer nuclear layer (ONL). While *Pde6b*$^{STOP/+}$ control mice maintained a relatively constant retinal thickness, (65.2 ± 4.6 µm) over time, the ONL thickness of *Pde6b*$^{STOP/STOP}$ mice decreased by 67%, 82%,

87%, and 91% at weeks 12, 16, 24, and 40, respectively, compared to 40-weeks-old WT mice (**Fig. 19A and Table 17**). The ONL thickness of mutant mice between 12 and 16 of age was significantly different ($P = 0.0018$, t-test), but not between 16 and 24 weeks of age ($P = 0.0672$, t-test) and not between 24 and 40 ($P = 0.1192$, t-test). To analyze rod photoreceptor degeneration, individual rod photoreceptor nuclei were counted. The quantification of the number of rod photoreceptors revealed that the number was decreased by 73%, 88%, 94%, and 95% in 12, 16, 24, and 40-weeks-old mutants, respectively (**Table 18**). A difference in rod number between 16 and 24 weeks of age ($P = 0.0259$, t-test), but not between 24 and 40 weeks of age ($P = 0.4382$, t-test).

As the focus of this thesis was whether treatment at the later stages of the disease is successful, we treated *Pde6b*$^{STOP/STOP}$ mice at weeks 12, 16, and 24. In 40-weeks-old *Pde6b*$^{STOP/STOP}$ mice treated at 12 or 16 weeks of age, ONL and rod degeneration were halted at the disease stage at which treatment was administered (**Fig. 19A,B** and **Table 17,18**). When mutant mice were treated at 24 weeks of age, the ONL thickness and rod number were similar to the mutants at 40 weeks of age.

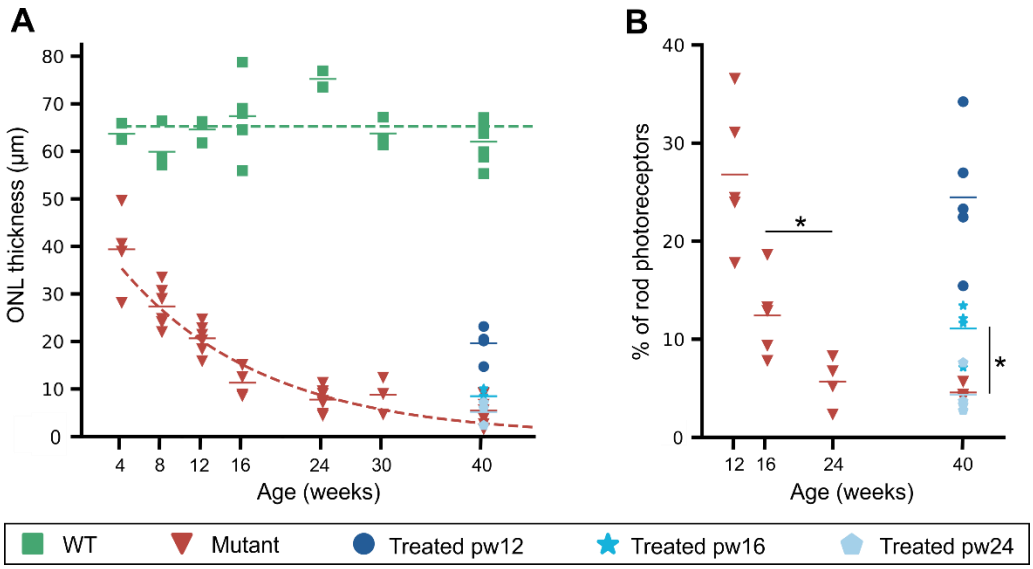

Fig. 19. Photoreceptor degeneration halted by treatment at 12 or 16 weeks of age. (A) ONL thickness of *Pde6b*$^{STOP/STOP}$ (mutant) and *Pde6b*$^{STOP/+}$ (WT) mice from 4 to 40 weeks of age, as well as mutants treated at 12, 16, and 24 weeks of age and sacrificed at pw40. Horizontal bars, mean ONL thickness. **(B)** Percent of rods in mutant mice at 12, 16, 24, and 40 weeks of age and mutants treated at 12, 16, and 24 weeks of age and sacrificed at pw40 (relative to 40-week-old WT retinas). Horizontal bars, mean rod percentage. Tukey's test for multiple comparisons mutant pw40 vs treated mutants. * $P \leq 0.05$.

Table 17. ONL thickness in untreated and treated mutant mice

Untreated		**Treated**	
Age at sacrifice (weeks)	ONL thickness (mean ± SEM; µm)	Age at treatment/ sacrifice (weeks)	ONL thickness (mean ± SEM; µm)
12	20.6 ± 1.3	12/40	19.6 ± 1.8
16	11.3 ± 1.6	16/40	8.5 ± 0.9
24	7.8 ± 0.9	24/40	5.2 ± 1.4
40	5.4 ± 1.0		

Table 18. Number of rod photoreceptors in untreated and treated mutant mice

Untreated		**Treated**	
Age at sacrifice (weeks)	Rod number (mean ± SEM; %) [+]	Age at treatment/ sacrifice (weeks)	Rod number (mean ± SEM; %) [+]
12	26.8 ± 7.2	12/40	24.5 ± 6.9
16	12.4 ± 1.9	16/40	11.1 ± 1.4
24	5.6 ± 1.3	24/40	4.3 ± 1.1
40	4.6 ± 0.4		

[+] Relative to the rod number of WT at 40 weeks

To analyze rod outer segments, retinal sections were labeled against rhodopsin. The rod outer segments of 40-weeks-old wild type showed normal rhodopsin expression in the outer segments (**Fig. 20B**). In untreated *Pde6b*$^{STOP/STOP}$ mice, rod outer segments progressively shorten as the disease progresses, and rhodopsin redistributes in untreated mutant mice aged 16 weeks and more from outer segments to inner segments and photoreceptor cell bodies, at later stages also to the neurites (**Fig. 20A**). In *Pde6b*$^{STOP/STOP}$ mice treated at 12 or 16 weeks of age, rod outer segments length was preserved, however not anymore in mice treated at 24 weeks of age (**Fig. 20B**).

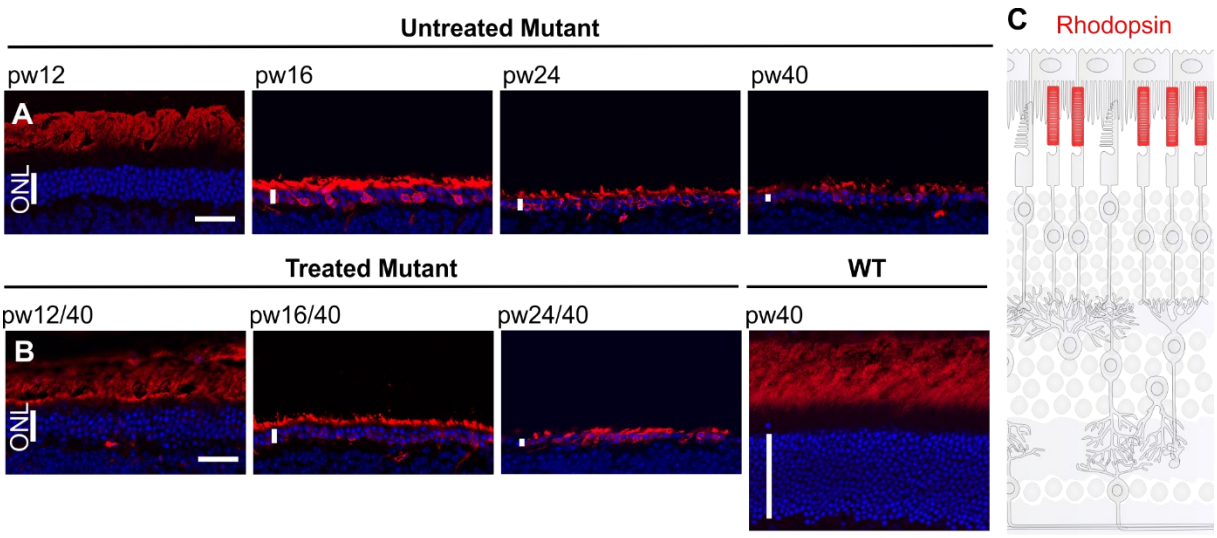

Fig. 20. Halt of rod outer segment degeneration after treatment at 12 weeks of age. (A,B) Representative images of retinal sections immunostained with anti-rhodopsin antibody and counterstained with Hoechst. **(A)** Untreated *Pde6b*$^{STOP/STOP}$ mice were sacrificed at 12, 16, 24, and 40 weeks of age. **(B)** *Pde6b*$^{STOP/STOP}$ mice were injected with tamoxifen at 12, 16, and 24 weeks of age, and then sacrificed at 40 weeks (treated). Pde6b$^{STOP/+}$ (WT; not treated) sacrificed at 40 weeks of age. **(C)** Schematic representation of healthy rod outer segments. Vertical white bars in A and B, ONL; horizontal scale bars, 30 µm.

To evaluate whether treatment was able to preserve the morphology of cone photoreceptors, retinal sections were immunolabeled with an anti-cone arrestin antibody. The cones of 40-weeks-old wild type showed normal cone arrestin expression, with well-organized parallel inner and outer segments, long axons, and pedicles aligned in the OPL (**Fig. 21B**). In untreated *Pde6b*$^{STOP/STOP}$ mice, the cone outer and inner segments became shorter with time. By the age of 40 weeks, the morphology of most cone photoreceptors in *Pde6b*$^{STOP/STOP}$ changes completely, some appeared to lack all processes except for the cell bodies (**Fig. 21A**). In 40-weeks-old *Pde6b*$^{STOP/STOP}$ mice treated at 12 or 16 weeks of age, further cone degeneration was halted (**Fig. 21B**). However, in *Pde6b*$^{STOP/STOP}$ mice treated at 24 weeks of age, cone degeneration continued.

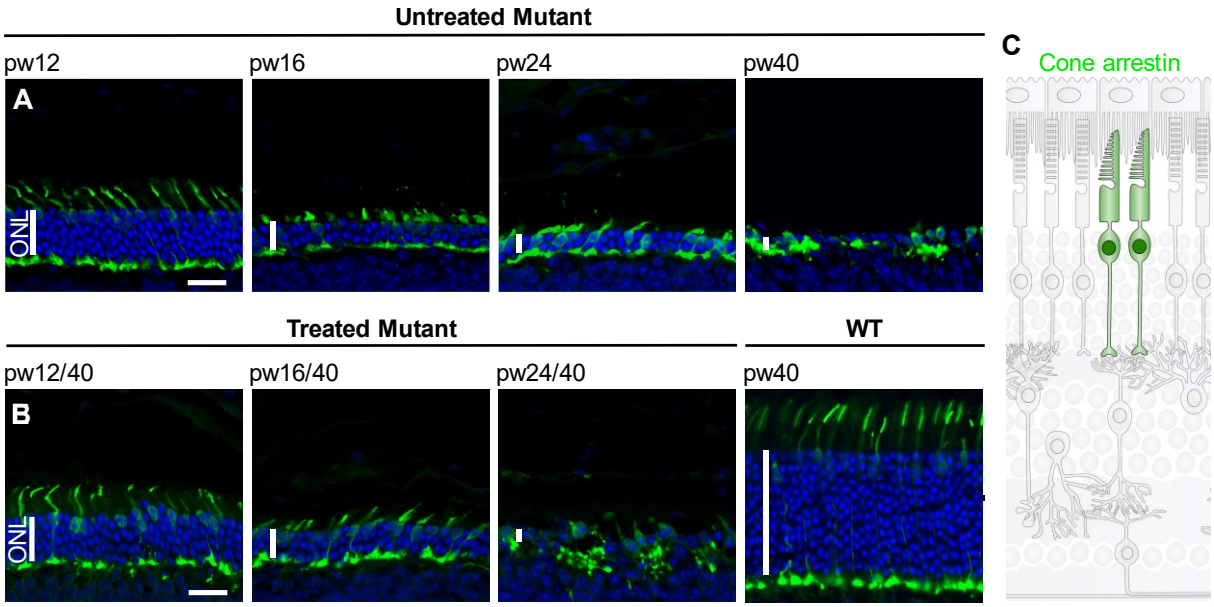

Fig. 21. Cone photoreceptor degeneration halted by treatment at 12 or 16 weeks of age, but not at 24 weeks. (A,B) Representative images of retinal sections immunostained with anti-cone arrestin antibody and counterstained with Hoechst. **(A)** Untreated *Pde6b*$^{STOP/STOP}$ mice were sacrificed at 12, 16, 24, and 40 weeks of age. **(B)** *Pde6b*$^{STOP/STOP}$ mice were injected with tamoxifen at 12, 16, and 24 weeks of age, and then sacrificed at 40 weeks (treated). Pde6b$^{STOP/+}$ (WT; not treated) sacrificed at 40 weeks of age. **(C)** Schematic representation of healthy cone cells. N values are provided in Material and methods. Vertical white bars in A and B, ONL; horizontal scale bars, 20 µm.

4.4. Remodeling of inner retinal cells halted by treatment at 16 weeks of age or earlier

Although RP is primarily a disease of the photoreceptors, the cells in the inner nuclear layer remodel as well (36). We evaluated how rod bipolar cells react to photoreceptor loss in *Pde6b*$^{STOP/STOP}$ mice and if those morphological alterations can be halted or are ever reversed by treatment. For this, rod bipolar cells were stained with an antibody against the protein kinase (PKC) –α (**Fig. 22**). The anti-PKC–α antibody labels the cell bodies, dendrites, axons, and the large lobular axon terminals of rod bipolar cells. Rod bipolar cells of 40-weeks-old WT retinas have dense, bushy dendritic arborization in the OPL with numerous dendrites irradiating from the cell (**Fig. 22B**; arrowhead). In 12-weeks-old untreated Pde6b$^{STOP/STOP}$ retina, the rod bipolar cell dendrites appear shorter and spatially disordered as compared to the 40-weeks-old WT (**Fig. 22A**). The retraction of the rod bipolar cell dendrites continues, so that in mutant mice of 24 weeks of age only a few very short dendrites are present. At 40 weeks of age, the majority of rod bipolar cells completely lack their dendrites and some cell bodies migrate to the ONL (**Fig. 22A**; arrow). In Pde6b$^{STOP/STOP}$ mice treated at 12 and 16 weeks of age, the dendritic area

was preserved (**Fig. 22B**). However, in *Pde6b*$^{STOP/STOP}$ mice treated at 24 weeks of age, rod bipolar cell dendrites retraction appeared to continue.

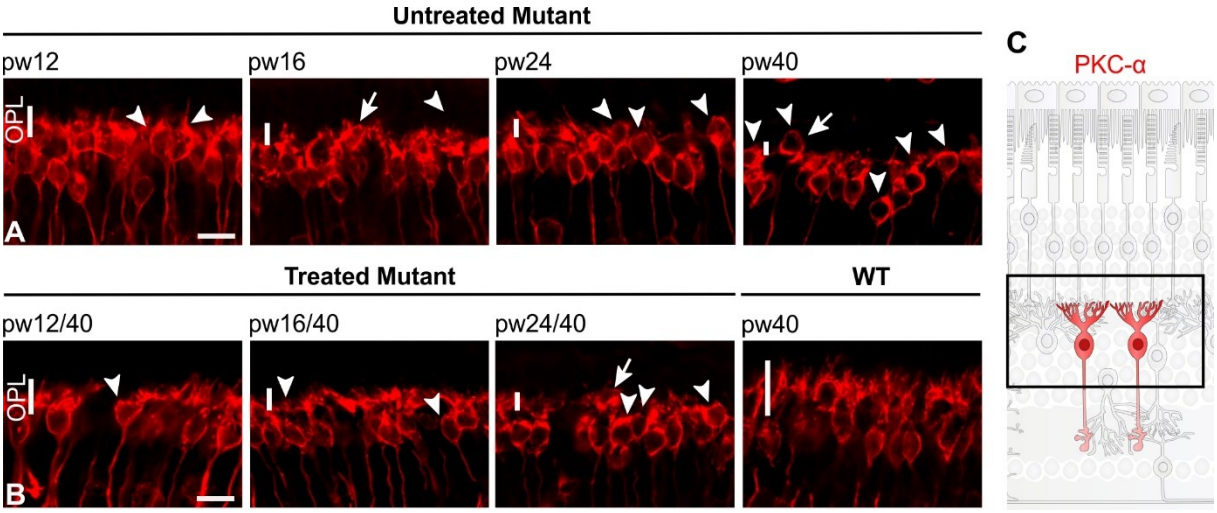

Fig. 22. Rod bipolar cell remodeling halted by treatment at 12 and 16 weeks of age, but not at 24 weeks. *Pde6b*$^{STOP/STOP}$ mice were treated (or not) at pw12, pw16, or pw24, and sacrificed at pw40. *Pde6b*$^{STOP/+}$ mice (WT) were 40 weeks of age. Retinal sections were labeled with anti-PKC–α antibodies to visualize rod bipolar cells, particularly their processes in the OPL. Sections from **(A)** untreated *Pde6b*$^{STOP/STOP}$ mice, and **(B)** treated *Pde6b*$^{STOP/STOP}$ and *Pde6b*$^{STOP/+}$ (WT) mice. Vertical white bars in A and B, rod bipolar dendrites in the OPL; arrowheads, rod bipolar cells having aberrant dendrites; arrows, ectopic cell body. Scale bars, 10 µm. **(C)** Schematic representation of healthy rod bipolar cells.

To quantify the remodeling of the rod bipolar cells, the area of the rod bipolar cell dendrites was analyzed in retinal sections (**Fig. 23A**). In mutant mice, the dendritic area progressively decreases and is significantly reduced compared to WT at 16, 24, and 40 weeks of age. The difference between pw24 and pw40 in mutant mice was only minor and not significantly different. After treatment at 16 weeks of age, the dendrite area was preserved when compared to 16-weeks-old mutants. The dendrite area in mice that were treated at 24 weeks of age remained at the level of the mutant at 24 weeks of age.

In addition, the number of PKC–α displaced cell bodies was quantified (**Fig. 23B**). A rod bipolar cell body was considered displaced if the PKC–α positive cell nucleus was localized in the ONL. In WT retinas we found almost no displaced cell bodies. The number of displaced rod bipolar cell bodies increased with disease progression (pw16 vs pw40, $P = 0.001$, t-test). No significant difference was found between pw24 and pw40 ($P = 0.3017$, t-test). Treatment at 12 and 16 weeks prevented the displacement of cell bodies to some extent.

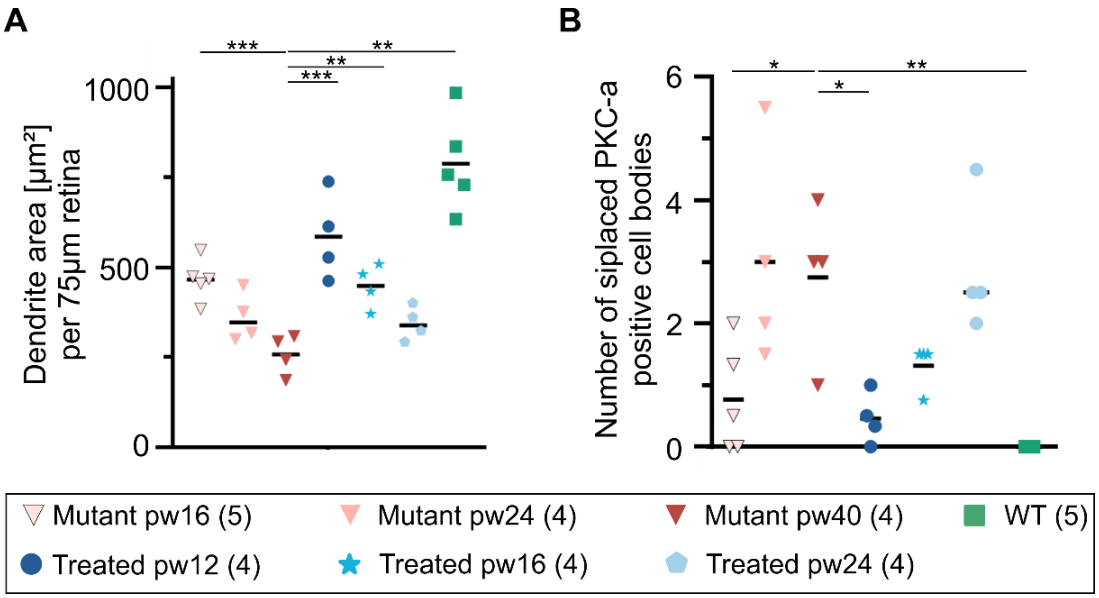

Fig. 23. Quantification of rod bipolar cell dendrites and displaced cell nuclei. *Pde6b*$^{STOP/STOP}$ mice were treated (or not) at pw12, pw16, or pw24, and sacrificed at pw40. *Pde6b*$^{STOP/+}$ mice (WT) were 40 weeks of age. Retinal sections were labeled with anti-PKC-α antibodies to visualize rod bipolar cells. **(A)** Using ImageJ the dendrite area from 75 µm wide retinas was quantified. **(B)** The number of displaced PKC-α positive cell bodies. Data represent individual values and mean (horizontal bar). T-test. * $P \leq 0.05$; ** $P \leq 0.01$; *** $P \leq 0.001$ (all in comparison to mutant pw40). N values are provided in the legend next to the groups.

Next, retinal vertical sections were stained with antibodies against SCGN to label most types of cone bipolar cells (81). The cone bipolar cells of 40-weeks-old *Pde6b*$^{STOP/+}$ mice possess a major dendritic branch emerging from the cell body that splits into minor branches the OPL (**Fig. 24B**). With disease progression in *Pde6b*$^{STOP/STOP}$ mice, the organization of the dendrites becomes disrupted, some cell bodies migrate toward the ONL (**Fig. 24A**). These minor morphological changes were also present in *Pde6b*$^{STOP/STOP}$ mice treated at 24 weeks of age (**Fig. 24B**). However, the total area of the dendrites is not significantly different at 40 weeks of age (**Fig. 25**).

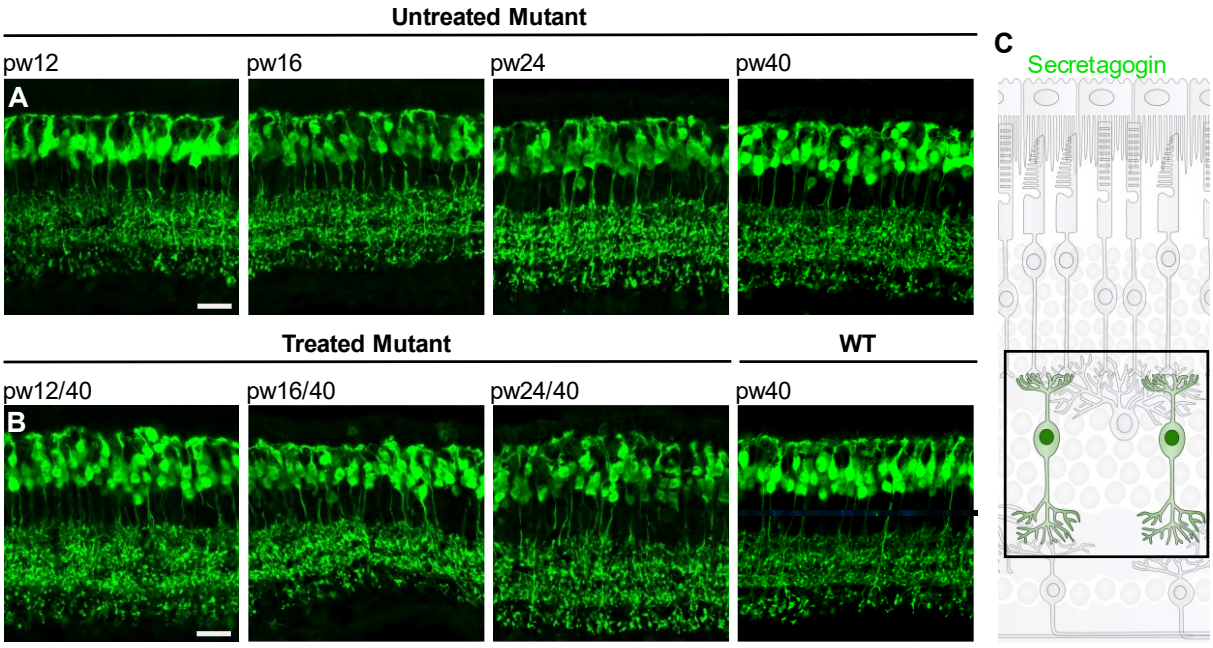

Fig. 24. Cone bipolar cell remodeling halted by treatment at 12 or 16 weeks of age, but not at 24 weeks. *Pde6b*$^{STOP/STOP}$ mice were treated (or not) at pw12, pw16, or pw24, and sacrificed at pw40. *Pde6b*$^{STOP/+}$ mice (WT) were 40 weeks of age. Retinal sections were labeled with anti-secretagogin antibodies to visualize cone bipolar cells, including their processes. Retinal sections from **(A)** untreated *Pde6b*$^{STOP/STOP}$ mice, and **(B)** treated Pde6b$^{STOP/STOP}$ and Pde6b$^{STOP/+}$ (WT) mice. Scale bars, 20 µm. **(C)** Schematic representation of healthy cone bipolar cells.

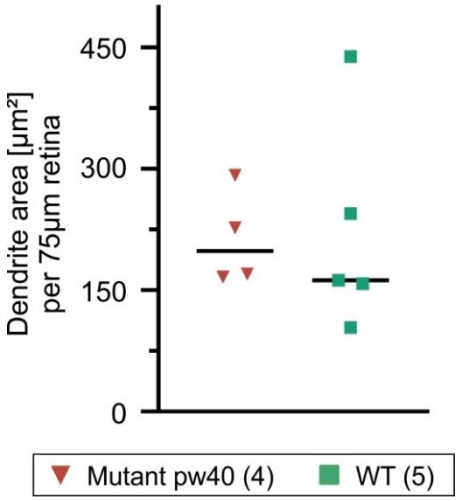

Fig. 25. Quantification of cone bipolar cell dendrites. *Pde6b*$^{STOP/STOP}$ and *Pde6b*$^{STOP/+}$ mice (WT) were 40 weeks of age. Retinal sections were labeled with anti-SCGN antibodies to visualize cone bipolar cells. Using ImageJ, the dendrite area from 75 µm wide retinas was quantified. Data represent individual values and mean (horizontal bar). N values are provided in the legend next to the groups.

Lastly, retinal horizontal cells were visualized using the calbindin-D28kD antibody, which labels the cell bodies and the dendrites. Horizontal cells of 40-weeks-old *Pde6b*$^{STOP/+}$ mice have a dense network of dendrites with tiny puncta in the OPL (**Fig. 26B**). With disease progression in untreated *Pde6b*$^{STOP/STOP}$ mice, the dendritic processes undergo progressive retraction, and the punctae disappear from the OPL (**Fig. 26A**). In mice treated at up to 16 weeks of age, the area of dendritic processes of the horizontal cells appeared to be preserved (**Fig. 26B**). On the contrary, when mice were treated at 24 weeks of age, the retraction of horizontal cell dendrites was not halted.

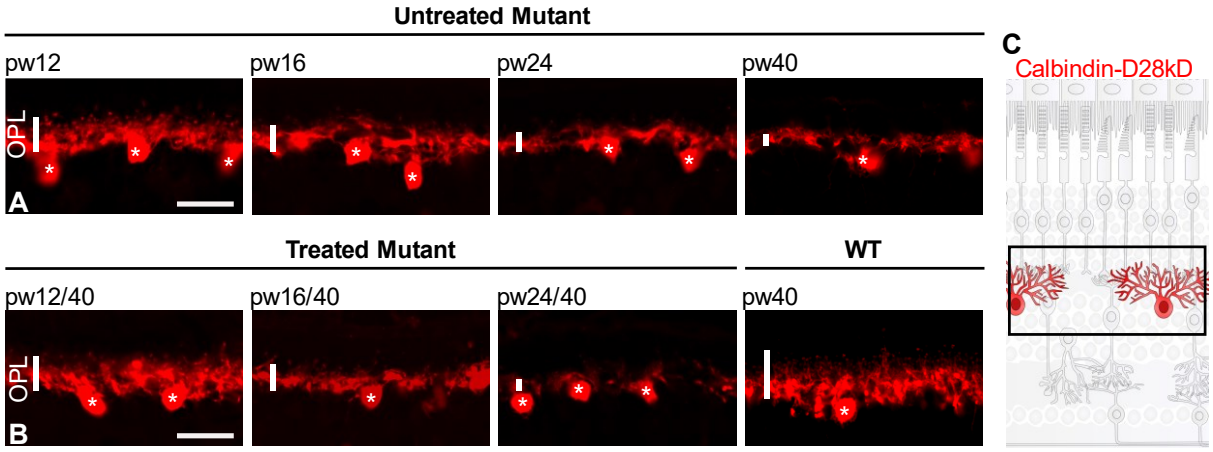

Fig. 26. Horizontal cell remodeling halted by treatment at 12 and 16 weeks of age, but not at 24 weeks. *Pde6b*$^{STOP/STOP}$ mice were treated (or not) at pw12, pw16, or pw24, and sacrificed at pw40. *Pde6b*$^{STOP/+}$ mice (WT) were 40 weeks of age. Retinal sections were labeled with anti-calbindin-D28kD antibodies to visualize horizontal cells, including their processes, in the OPL (vertical white bars). Retinal sections from **(A)** untreated *Pde6b*$^{STOP/STOP}$ mice, and **(B)** treated *Pde6b*$^{STOP/STOP}$ and *Pde6b*$^{STOP/+}$ (WT) mice. Asterisks indicate horizontal cell bodies. Scale bars, 20 µm. **(C)** Schematic representation of healthy horizontal cells.

To quantify the remodeling of the horizontal cell processes, the area of the calbindin-D28k positive staining excluding the cell body area was analyzed in retinal sections (**Fig. 27**). In mutant animals, the horizontal process area decreased by disease progression. In 12-weeks-old mutant mice, the processes were already significantly decreased in comparison to WT but were still more numerous than in mutants at week 40. While in mutants at 16 weeks of age a difference to the 40-weeks-old mutant animals was present; the difference almost disappeared by 24 weeks of age. In 40-weeks-old mice that were treated up to 16 weeks of age, the area of the processes was halted and was still statistically higher compared to mutant 40 weeks of age. The mean process area in mice that were treated at 24 weeks of age was slightly lower but was not significant when compared to mutants at 24 weeks of age.

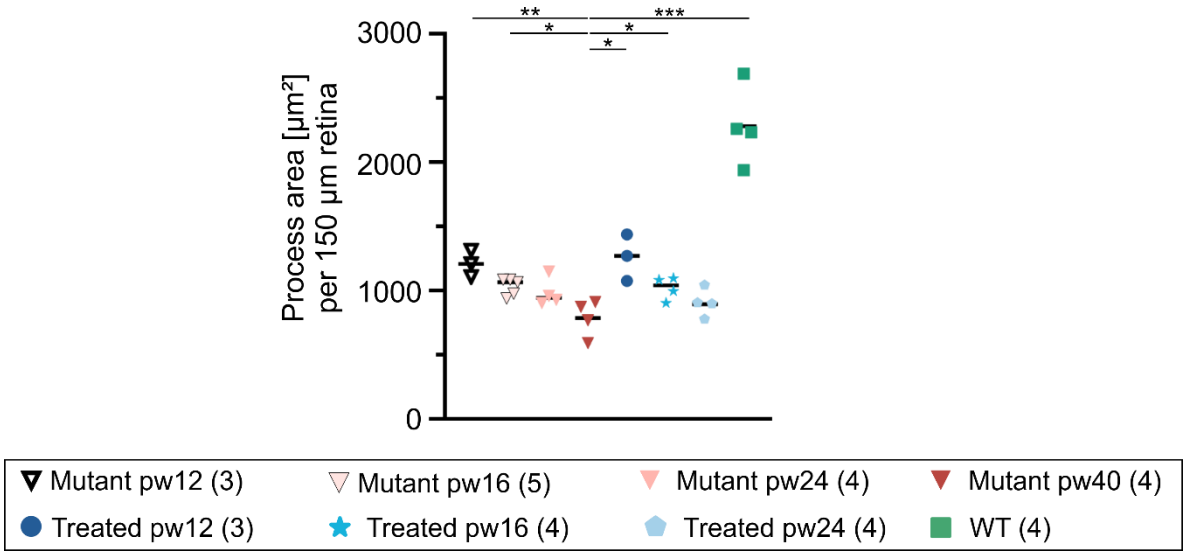

Fig. 27. Quantification of horizontal cell processes. *Pde6b*$^{STOP/STOP}$ and *Pde6b*$^{STOP/+}$ mice (WT) were 40 weeks of age. Retinal sections were labeled with anti-calbindin-D28k antibodies to visualize horizontal cells. Using ImageJ the area with the processes from 150 µm wide retinas was quantified. Data represent individual values and mean (horizontal bar). T-test. * $P \leq 0.05$; ** $P \leq 0.01$; *** $P \leq 0.001$ (all in comparison to mutant pw40). N values are provided in the legend next to the groups.

4.5. RPE remodeling continues after treatment at pw16 and pw24

The death of photoreceptors in RP causes changes to the RPE monolayer (46). Morphological changes in our RP mouse model and the impact of therapy on the RPE morphology were evaluated by immunolabeling the RPE cell adhesions using a β-catenin antibody (**Fig. 28**). In 40-week-old *Pde6b*$^{STOP/+}$ mice, the RPE cells had a polygonal, mostly hexagonal shape with uniform cell size in both central and equatorial RPE region (**Fig. 28B**; right-most panels). In untreated 16-week-old *Pde6b*$^{STOP/STOP}$ mice (**Fig. 28A**), the RPE maintained its shape. At 24 weeks of age, we observed disruption of the regular cell size and shape. The morphology changed more dramatically in the center, where an increased number of cells with enlarged cell areas are present (**Fig. 28**; dots). The β-catenin staining exhibited decreased cell boundary localization. Instead of being concentrated solely at cell-cell contacts, diffuse labeling of the β-catenin was detected in the cytoplasm (**Fig. 28A**; arrowheads). The RPE cells of the untreated *Pde6b*$^{STOP/STOP}$ at pw40 showed significant changes of the morphology in the equatorial region, changing to strikingly elongated cells (**Fig. 28A**). In the periphery, RPE cells only exhibited minor morphological changes (**Fig. 29**). In *Pde6b*$^{STOP/STOP}$ mice treated at 16 or 24 weeks, the

remodeling of the RPE cells appeared to continue, in both the central and equatorial regions (**Fig.28B**; left and middle panel).

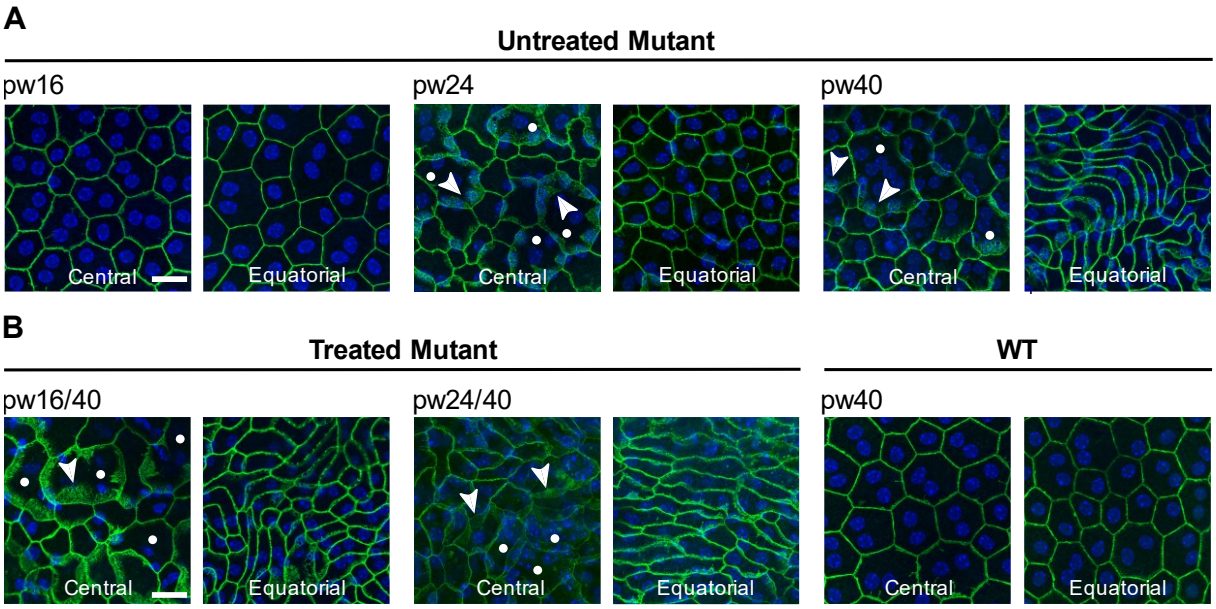

Fig. 28. Morphological abnormalities of RPE monolayer of the *Pde6b*$^{STOP/STOP}$ mice cannot be halted after treatment at 16 or 24 weeks of age. Untreated *Pde6b*$^{STOP/STOP}$ mice were sacrificed at 16, 24, or 40 weeks of age. Pde6b$^{STOP/+}$ (WT) mice and *Pde6b*$^{STOP/STOP}$ mice treated at 16 and 24 weeks of age were all sacrificed at 40 weeks of age. RPE-choroid-sclera flat-mounts were labeled with an anti-β-catenin antibody (green) to visualize a component of adherens junctions, which form the cell-cell contacts**. (A)** RPE flat-mounts from untreated *Pde6b*$^{STOP/STOP}$ mice at 16, 24, and 40 weeks of age and **(B)** from 40-weeks-old *Pde6b*$^{STOP/+}$ (WT/untreated) and treated *Pde6b*$^{STOP/STOP}$ mice. Images were taken in the central and equatorial regions of the RPE. Arrowheads indicate diffuse β-catenin labeling in the cytoplasm, the white dots represent enlarged RPE cells. Scale bars, 20 μm.

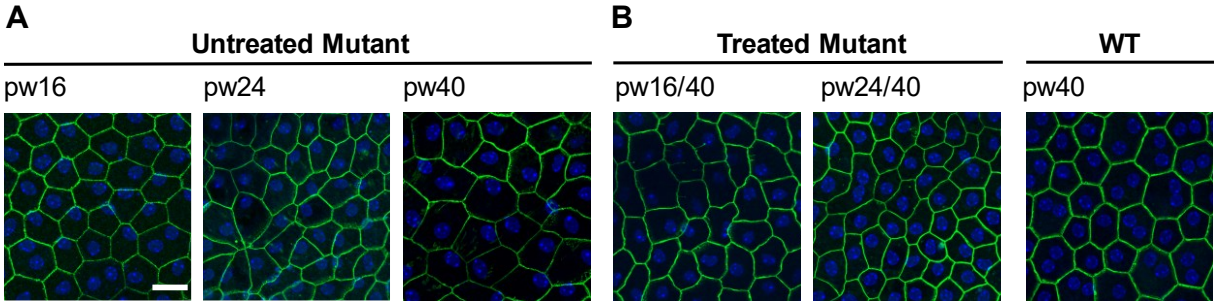

Fig. 29. Minor morphological changes of the peripheral retinal pigment epithelium. *Pde6b*$^{STOP/STOP}$ mice were injected with tamoxifen at 16 and 24 weeks of age and sacrificed at 40. RPE flat-mounts were labeled with an anti-β-catenin antibody (green) to visualize a component of adherens junctions, which form the cell-cell contacts. **(A)** RPE flat-mounts from untreated *Pde6b*$^{STOP/STOP}$ mice at 16, 24, and 40 weeks of age and **(B)** from 40-weeks-old *Pde6b*$^{STOP/+}$ (WT/untreated) and treated *Pde6b*$^{STOP/STOP}$ mice. Scale bar, 20 µm.

Morphometric analysis of the RPE cells was performed to quantify the changes to the RPE monolayer in the central, equatorial, and peripheral regions (**Fig. 13**). The cell size measurement in the center revealed that in 40-weeks-old *Pde6b*$^{STOP/+}$ mice, 96% of the RPE cells had an area of 150 – 699 µm² (**Fig. 30**). On the other hand, in 40-weeks-old *Pde6b*$^{STOP/STOP}$ mice only 73% the percent of RPE cells in the center had an area of 150 – 699 µm² (WT vs mutant pw40, $P = 0.0493$, Tukey's test): RPE cells became smaller than 150 µm² and bigger than 700 µm² (**Fig. 30**). In comparison with *Pde6b*$^{STOP/STOP}$ at 40 weeks of age, 16-weeks-old *Pde6b*$^{STOP/STOP}$ had significantly more RPE cells with the area of 150 – 699 µm² (96%) ($P = 0.0316$; Tukey′s test). *Pde6b*$^{STOP/STOP}$ of 24 weeks of age did not differ to 40-weeks-old mutants ($P = 0.3551$; Tukey′s test).

In the equatorial region, no cells were smaller than 150 µm² in 40-weeks-old *Pde6b*$^{STOP/+}$ (**Fig. 30**). The percent of RPE cells smaller than 150 µm² in 40-weeks-old *Pde6b*$^{STOP/STOP}$ was 43%. In *Pde6b*$^{STOP/STOP}$ mice at 16 and 24 weeks, the percent of RPE cell size in the equatorial region with the area of 150 – 699 µm² was statistically greater in comparison with the mice at 40 weeks ($P = 0.0057$ and $P = 0.260$, respectively, Tukey′s test). This shows, that the RPE cell area starts to change in the central area (the cell size in the central area in 24-week-old mutant is not significantly different to 40-weeks-old mutant) and spreads toward the equatorial region (the cell area in 24-weeks-old mutant is significantly different to 40-weeks-old mutant in the equatorial region). In the peripheral region, no statistical difference was observed among the groups.

Treatment at 16 or 24 weeks of age did not halt the remodeling of the RPE cells. The cell area of treated RPE cells changed in comparison to the cell area of RPE at the time of treatment

and was not statistically different to 40-weeks-old *Pde6b*$^{STOP/STOP}$ in both the central and equatorial region.

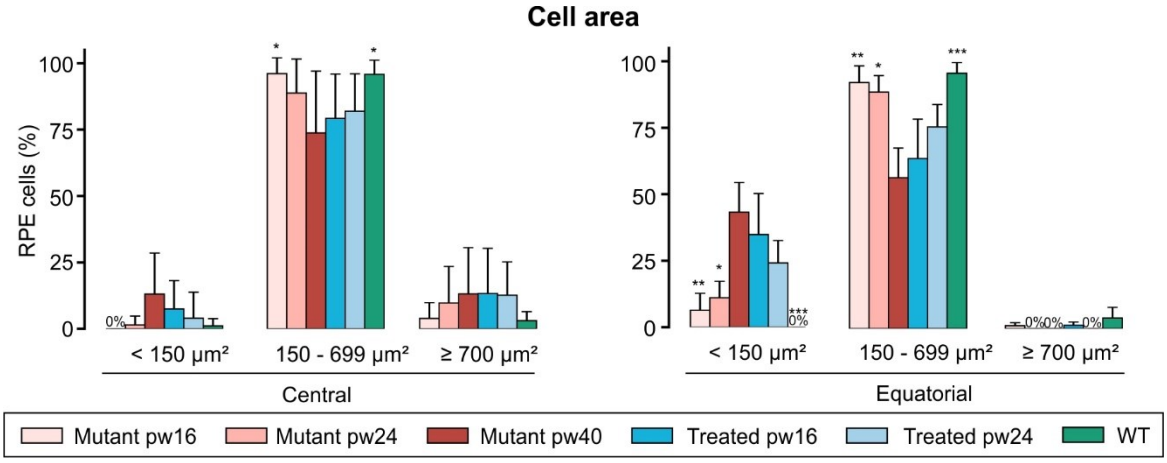

Fig. 30. Cell size measurements of RPE cells in the central and equatorial regions. The percentage of RPE cells that are smaller than 150 µm², are between 150-699 µm² or are equal or larger than 700 µm² was quantified in CellProfiler in untreated *Pde6b*$^{STOP/STOP}$ mice at 16, 24, and 40 weeks of age and in 40-weeks-old *Pde6b*$^{STOP/+}$ (WT) as well as treated *Pde6b*$^{STOP/STOP}$ mice at 16 or 24 weeks of age. Data represent mean percentage ± SEM; Tukey's test for multiple comparisons. * $P \leq 0.05$; ** $P \leq 0.01$; *** $P \leq 0.001$ (all in comparison to mutant pw40). N values are provided in Material and methods.

The elongation of the RPE cells was measured through the eccentricity factor (**Fig. 13**). In the central region, no RPE cells had an eccentricity of equal or greater than 0.8 in 40-weeks-old *Pde6b*$^{STOP/+}$ and 16-weeks-old *Pde6b*$^{STOP/STOP}$ mice (**Fig. 31**). The proportion of RPE cells in 40-weeks-old *Pde6b*$^{STOP/STOP}$ with the same eccentricity was statistically greater with 53% (mutant pw16 vs mutant pw40 and WT vs mutant pw40; $P < 0.0001$; Tukey's test). Untreated *Pde6b*$^{STOP/STOP}$ at 24 weeks had 23% percent RPE cells with the eccentricity being equal to or greater than 0.8.

Compared with the central region, the equatorial region of the 40-weeks-old *Pde6b*$^{STOP/STOP}$ had even more (71%) of the RPE cells with an eccentricity of equals or greater than 0.8. This was again significantly more than in 16-weeks-old *Pde6b*$^{STOP/STOP}$ with 11% (mutant pw16 vs mutant pw40; $P < 0.001$; Tukey's test). Again, as for the RPE cell area, the eccentricity among groups was not different in the periphery.

When *Pde6b*$^{STOP/STOP}$ mice were treated at 16 or 24 weeks of age, the eccentricity of the RPE cells seemed to continue to change, as the number of elongated cells (eccentricity ≥ 0.8) increased in comparison to 16- or 24-week-old untreated mutants. No significant differences

were present in the central or equatorial region between mice that were treated at 16 or 24 weeks of age compared to 40-weeks-old untreated *Pde6b*$^{STOP/STOP}$.

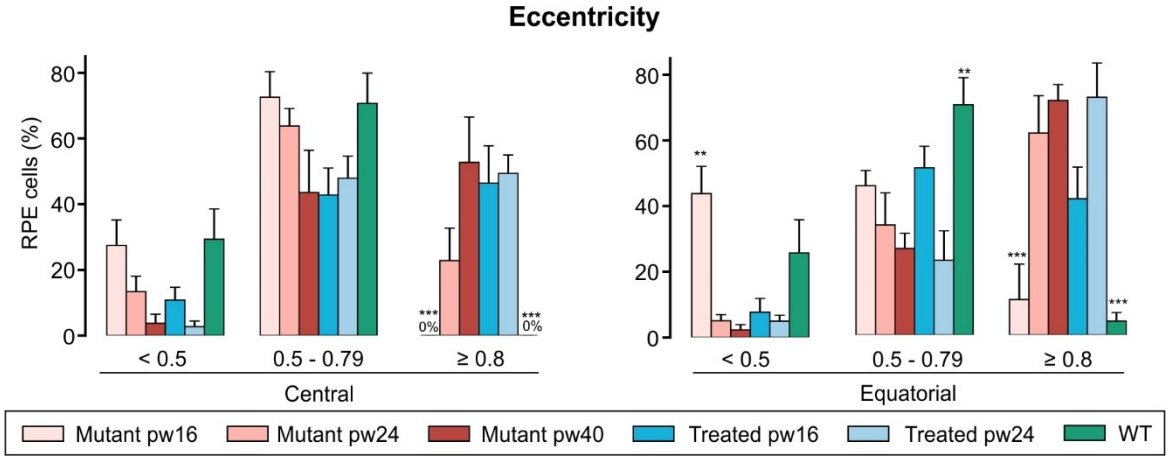

Fig. 31. The eccentricity of RPE cells in the central and equatorial regions. The percentage of RPE cells that have an eccentricity of lower than 0.5, between 0.5 and 0.79, or equal or higher than 0.8 were quantified in CellProfiler in untreated *Pde6b*$^{STOP/STOP}$ mice at 16, 24, and 40 weeks of age and in 40-weeks-old *Pde6b*$^{STOP/+}$ (WT) and treated *Pde6b*$^{STOP/STOP}$ mice at 16 or 24 weeks of age. Data represent mean percentage ± SEM; Tukey's test for multiple comparisons. *** $P \leq 0.001$ (all in comparison to mutant pw40). N values are provided in Material and methods.

Next, the percent of RPE cells with different solidity values (proportion of the RPE cell area filling a best-fit convex envelope) was analyzed (**Fig. 13**). In the central region of the 40-weeks-old *Pde6b*$^{STOP/+}$ mice, no cells had a solidity of less than 0.85, and 56% had a solidity of ≥ 0.93 (**Fig. 32**). Quantifications in untreated 16-weeks-old *Pde6b*$^{STOP/STOP}$ mice were similar to WT at 16 weeks (2% for < 0.85 and 48% for ≥ 0.93) but became distinct at 24 weeks of age. The solidity of the RPE cells of untreated 24-weeks-old *Pde6b*$^{STOP/STOP}$ mice was similar to the one at 40 weeks.

The solidity of the RPE cells in the equatorial region was similar to the central region among the groups. In 40-weeks-old *Pde6b*$^{STOP/+}$ mice, 66% of cells in the equatorial region had a solidity of ≥ 0.93, which was more than in mutants aged 40 weeks ($P = 0.0032$, Tukey's test). In 16-weeks-old mutant mice the number of RPE cells with a solidity of ≥ 0.93 was still higher to mutants pw40 (P = 0.0457, Tukey's test) but not anymore at 24 weeks when the values became comparable to 40-weeks-old mutants ($P > 0.9999$, Tukey's test).

In animals that were treated at 16 or 24 weeks of age, the RPE cells had a similar solidity to the cells of 40-weeks-old untreated mice in both the central and equatorial regions. With treatment at 16 weeks of age, the change of the RPE cell solidity seemed to continue.

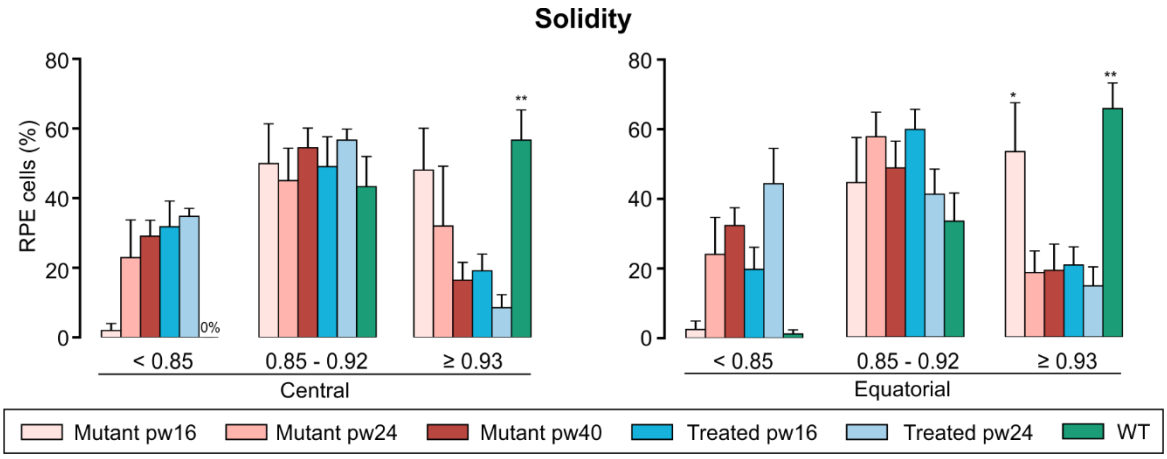

Fig. 32. The solidity of RPE cells in the central and equatorial regions. The percentage of RPE cells that have a solidity of lower than 0.5, between 0.5 and 0.79, or equal or higher than 0.8 were quantified in CellProfiler in untreated *Pde6b*$^{STOP/STOP}$ mice at 16, 24, and 40 weeks of age and in 40-weeks-old *Pde6b*$^{STOP/+}$ (WT) and treated *Pde6b*$^{STOP/STOP}$ mice at 16 or 24 weeks of age. Data represent mean percentage ± SEM; Tukey's test for multiple comparisons. *** $P \leq 0.001$ (all in comparison to mutant pw40). N values are provided in Material and methods.

RPE cell multinucleation is associated with age and is thought to be triggered by atrophic cells in the RPE (75). To characterize the changes in the number of nuclei per cell, the RPE-choroid-sclera was labeled against β-catenin and co-stained with Hoechst. In the central region the number of RPE cells with one nucleus per cell in untreated *Pde6b*$^{STOP/STOP}$ mice in comparison to age-matched *Pde6b*$^{STOP/+}$ was significantly greater ($P = 0.0152$, Sidaks's test), and with two nuclei per cells significantly lower ($P = 0.003$, Sidaks's test) (**Fig. 33**). The distribution pattern in the equatorial region was similar to the center. In the periphery, more than 85% of the cells had only one nucleus and no significant difference between WT and mutant was observed.

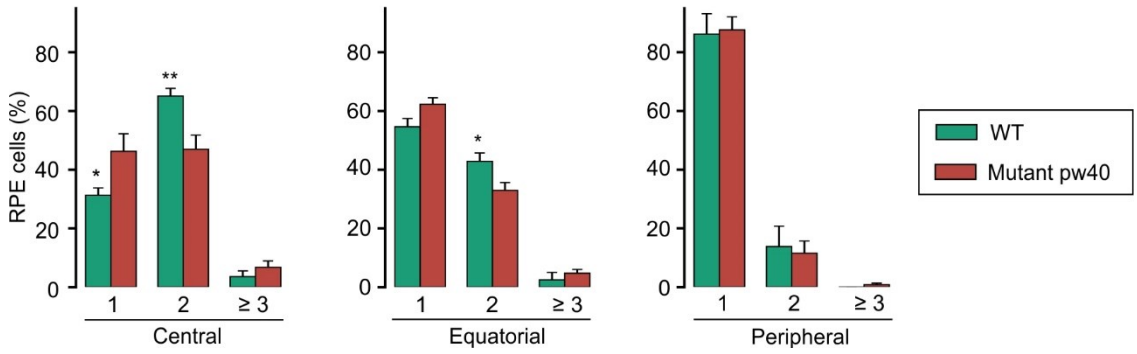

Fig. 33. The number of nuclei per RPE cell in the central, equatorial and peripheral regions. The percentage of RPE cells that have 1, 2, and 3 or more nuclei in 40-weeks-old untreated *Pde6b*$^{STOP/STOP}$ mice vs *Pde6b*$^{STOP/+}$ (WT). Data represent mean percentage ± SEM; Tukey's test for multiple comparisons. * $P \leq 0.05$; ** $P \leq 0.01$ (in comparison to mutant). N values are provided in Material and methods.

4.6. Blood vessel remodeling is partially affected by treatment

RP has been associated with structural changes of the retinal vasculature (51, 54, 59, 82). To examine vascular pathologies, whole mounted retinas were stained with an endothelial cell marker isolectin GS-IB4 (**Fig. 34**). Of the 3-layered interconnected retinal vascular network supplying the inner retina, the deep and intermediate vascular plexus (DVP + IVP) were merged, and the superficial vascular plexus (SVP) was analyzed separately. The DVP + IVP of 40-weeks-old *Pde6b*$^{STOP/+}$ mice showed normal retinal capillary loops, with similar diameter among individual capillaries (**Fig. 34A,B**). At 24 weeks of age, the vessel network of untreated *Pde6b*$^{STOP/STOP}$ changes, some retinal capillary loops are lost and some of the remaining capillary diameters got thinner. By 40 weeks of age, the substantial remodeling of the vascular bed was even more visible. Treatment at 16 and 24 weeks of age did not seem to halt vascular changes completely.

The SVP is directly supplied by the central retinal artery, lays in the ganglion cell layer, and is composed of larger vessels. In 40-weeks-old *Pde6b*$^{STOP/STOP}$ mice as well as some mice that were treated at 24 weeks of age, we observed some tortuous vessels (**Fig. 34A**; arrowheads).

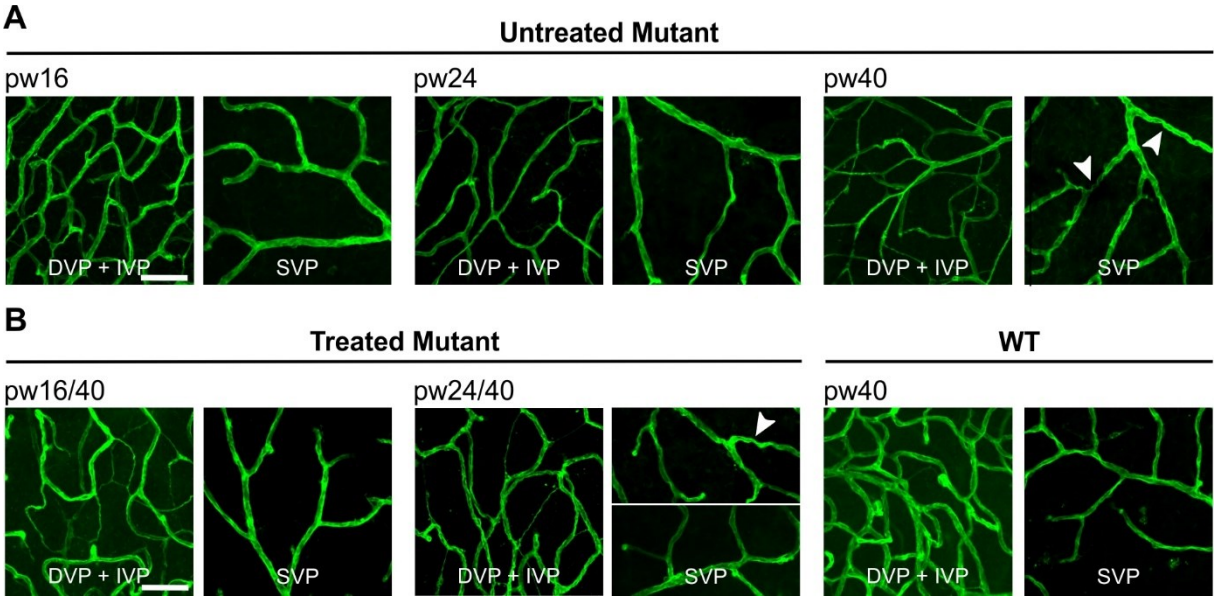

Fig. 34. Morphological abnormalities of the deep and intermediate and superficial vascular plexus. Untreated *Pde6b*$^{STOP/STOP}$ mice were sacrificed at 16, 24, or 40 weeks of age. Pde6b$^{STOP/+}$ (WT) mice and *Pde6b*$^{STOP/STOP}$ mice treated at 16 and 24 weeks of age were all sacrificed at 40 weeks of age. Retinas were stained with isolectin GS-IB4. Shown are the maximum intensity projection images of the merged deep and intermediate plexus (DVP + IVP) and the superficial vascular plexus (SVP). Arrowheads, tortuous vessels. Scale bars, 50 µm.

To quantify the vascular degenerative changes, isolectin GS-IB4 stained retinas were imaged in the central and peripheral retina and the maximum intensity projection images of the DVP + IVP and SVP were analyzed with AngioTool. Despite the morphological alterations of the SVP no differences were found in the vascular surface area between WT, untreated, and treated mice (**Fig. 35**).

The capillary vessels area in the central retina was 31% in 40-weeks-old Pde6b$^{STOP/+}$ and 32% in 16-weeks-old *Pde6b*$^{STOP/STOP}$. By 24 weeks, the area was reduced to 28%, however, in comparison to WT, it was not statistically different. By 40 weeks the *Pde6b*$^{STOP/STOP}$ area was statistically reduced to 24% in comparison to WT ($P < 0.0001$, Tukey's test). Mice that were treated at 16 weeks of age had a significant decrease in vessel area in comparison to untreated *Pde6b*$^{STOP/STOP}$ animals at 16 weeks of age ($P = 0.0066$, Tukey's test) and were on top not any more different to the 40-weeks-old untreated animals ($P = 0.8585$, Tukey's test). In the central region loss of capillary vessels, the area could already not be prevented by treatment at 16 weeks.

In the peripheral retina, the vessel area of 40-weeks-old *Pde6b*$^{STOP/+}$ mice was 28% and was lower than in the center. In *Pde6b*$^{STOP/STOP}$ the vessel area was statistically greater up to 24 weeks (22%) in comparison to 40-weeks-old *Pde6b*$^{STOP/STOP}$ (19%) (mutant pw24 vs pw40,

P = 0.0037). Treatment at 16 weeks of age halted the loss of capillary vessel area in the periphery (24%) (treated pw24 vs mutant pw40, *P* = 0.0481, Tukey's test). When animals were treated at 24 weeks of age the peripheral vessel area was reduced to 22% and was thus not any more different to 40-weeks-old untreated mice (*P* = 0.2816, Tukey's test).

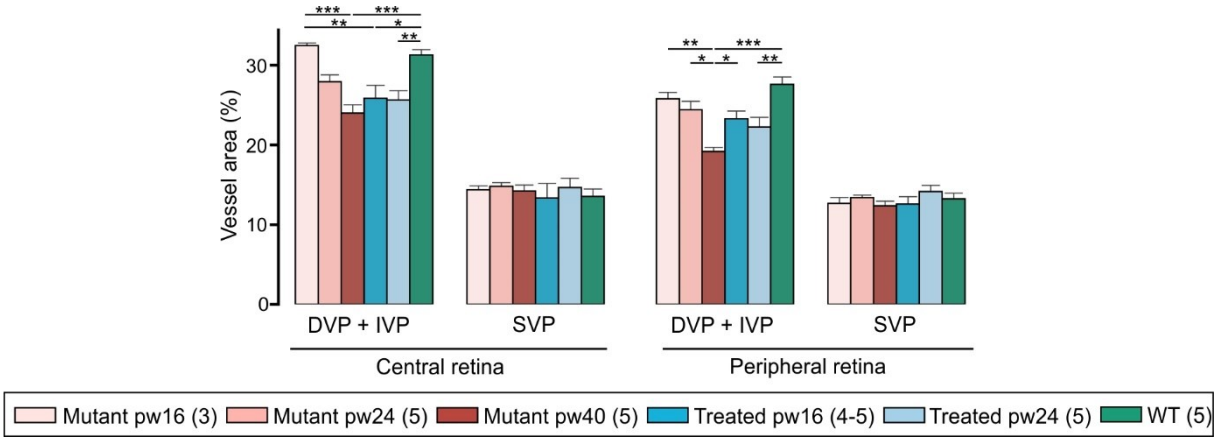

Fig. 35. Analysis of the central and peripheral blood vessel area. Untreated *Pde6b*$^{STOP/STOP}$ mice were sacrificed at 16, 24, or 40 weeks of age. Pde6b$^{STOP/+}$ (WT) mice and *Pde6b*$^{STOP/STOP}$ mice treated at 16 and 24 weeks of age were all sacrificed at 40 weeks of age. Retinas were stained with isolectin GS-IB4, imaged and the merged deep and intermediate plexus (DVP + IVP), as well as the superficial vascular plexus (SVP), quantified using AngioTool software. Data presented as mean ± SEM; Tukey's test for multiple comparisons. * $P \leq 0.05$; ** $P \leq 0.01$; *** $P \leq 0.001$. N values are provided in the legend next to the groups.

Another pathologic vascular change is the formation of acellular capillaries. They emerge when endothelial cells die, leaving empty basement membrane sleeves with no endothelial cell nuclei along their length behind (63). To assess the formation of acellular capillaries trypsin digested retinas were stained with hematoxylin and eosin. In *Pde6b*$^{STOP/+}$ mice, only a few acellular capillaries were present at 12, 16, 30, and 40 weeks of age (**Fig. 36A,B**). In untreated *Pde6b*$^{STOP/STOP}$ mice, the acellular capillaries were not significantly increased up to 24 weeks of age in comparison to WT but dramatically increased at 30 and 40 weeks of age (**Fig. 36B**). When *Pde6b*$^{STOP/STOP}$ mice were treated at 12 weeks of age, the number of acellular capillaries was not significantly different from 40-weeks-old WT (*P* = 0.8019, t-test) (**Fig. 36B**). In mice treated at 16 weeks, we observed a small non-significant increase in the number of acellular capillaries compared to *Pde6b*$^{STOP/+}$ (*P* = 0.1087, t-test). This increase was significantly different compared to mutant pw40 (*P* = 0.0012, t-test). When mice were treated at 24 weeks of age, the mean number of acellular capillaries was not significantly different compared to untreated *Pde6b*$^{STOP/STOP}$ pw40 (*P* = 0.1015, t-test).

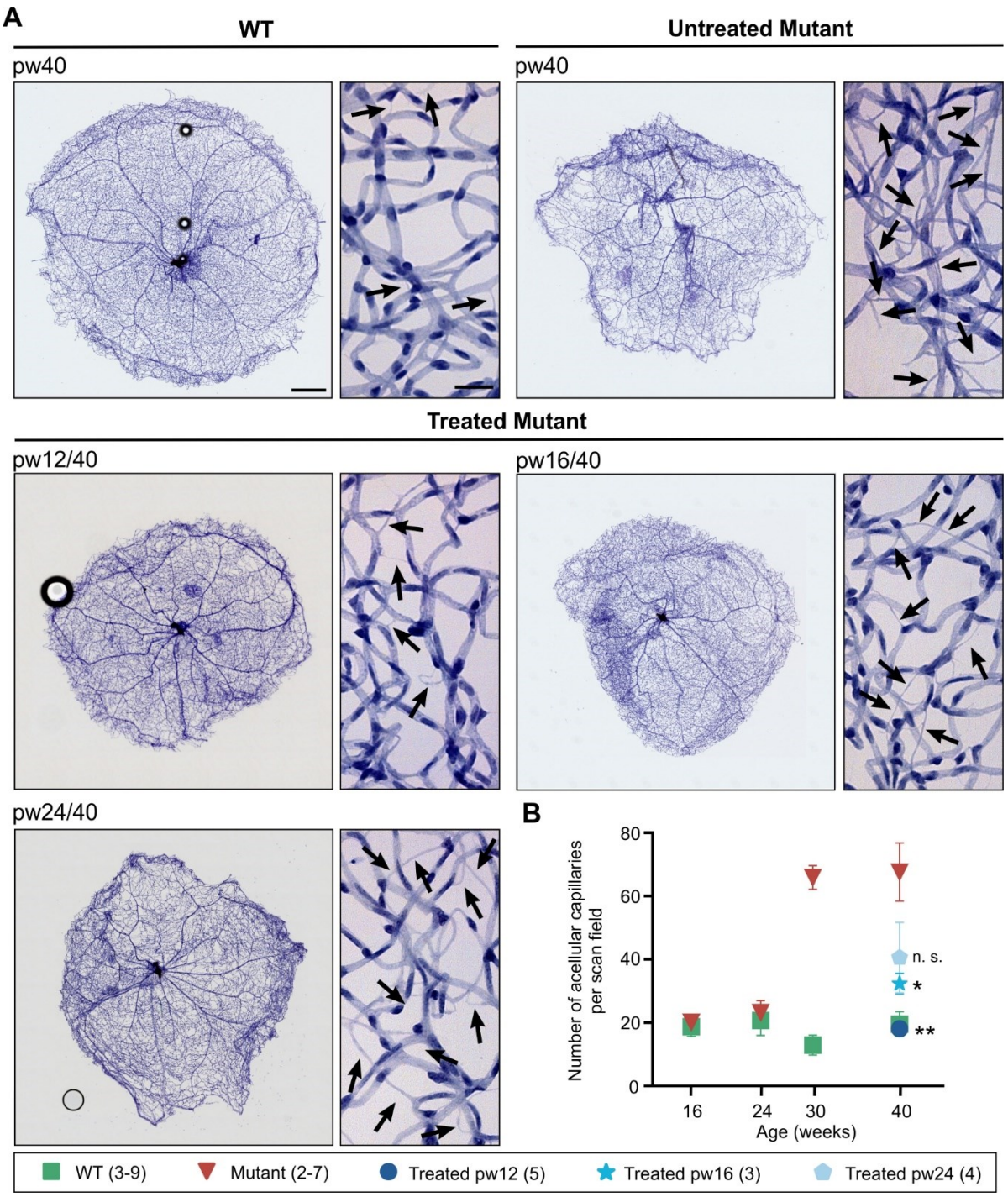

Fig. 36. Quantification of acellular capillaries. Untreated *Pde6b*$^{STOP/STOP}$ (mutant) and *Pde6b*$^{STOP/+}$ (WT) mice were sacrificed at 16, 24, 30, and 40 weeks of age. *Pde6b*$^{STOP/STOP}$ mutant mice were treated at 12, 16, or 24 weeks of age, and were sacrificed at 40 weeks of age. Whole-mounted retinas were trypsin digested and stained with hematoxylin and eosin. **(A)** Representative images of whole retinal vasculature and higher-magnification images—all at 40 weeks of age. Black arrows, acellular capillaries; scale bars, 500 µm (whole retina/low mag), and 25 µm (high mag). **(B)** Mean number of acellular capillaries per scan field (± SEM); t-test comparing treated mutants vs 40-week-old untreated mutant; n.s. not significant; * $P \leq 0.05$; ** $P \leq 0.01$. N values are provided in the legend next to the groups and in detail in Material and methods.

4.7. ERG

To measure the effect of treatment on retinal function, full-field single-flash ERG responses were recorded in 40-week-old mice. ERGs measure the transretinal potential change generated during phototransduction in response to light. The signal is composed of a negative deflection (a-wave) followed by a positive deflection (b-wave). The a-wave is a direct measure of the photoreceptor response, and the b-wave is generated by cells in the inner retina (83). At luminance of -2.0 log (cd·s/m^2) or less (ie, the scotopic range), only rods are activated (84). At higher stimulus intensities (ie, the mesopic range), both rods and cones are activated. After exposing animals to rod-saturating background light, the photopic response of cones can be measured.

In *Pde6b*$^{STOP/+}$ mice, the scotopic a-wave amplitude increased with increasing light intensities and develops a clear a-wave at -1.5 log (cd·s/m²) (**Fig. 37A**) which is also seen from the representative curves as a negative deflection (**Fig. 37C**). In contrast, in untreated *Pde6b*$^{STOP/STOP}$ mice, the a-wave was completely absent (**Fig. 37A,C**). In mice treated at 16 and 24 weeks of age, the a-wave amplitude was indistinguishable from mutants. Treatment at 12 weeks of age had a small effect on the a-wave amplitude, however, it was not statistically different to the mutant animals. At 0.5 log (cd·s/m²) the mean amplitude was 32% of that of the WT at the same light intensity.

In *Pde6b*$^{STOP/+}$ mice, the positive b-wave, initiated by the bipolar cells, was present at -3.0 log (cd·s/m²) and increased at higher light intensities (**Fig. 37B,C**) In the untreated *Pde6b*$^{STOP/STOP}$ mice, the b-wave amplitude at -3.0 log (cd·s/m²) was low and it did not increase up to the highest measured intensity at 1.0 log (cd·s/m²). The b-wave amplitudes of *Pde6b*$^{STOP/STOP}$ retinas were partially (yet significantly) rescued by treatment at either pw12 or pw16 (vs untreated *Pde6b*$^{STOP/STOP}$) and the increase of the b-wave amplitude was more apparent at higher stimulus intensities. At 0.5 log (cd·s/m²) the mean b-wave amplitude was 51% and 39% of that of the WT for mice treated at 12 and 16 weeks, respectively. In contrast, the b-wave amplitude of animals treated at 24 weeks of age remained at the level of untreated animals.

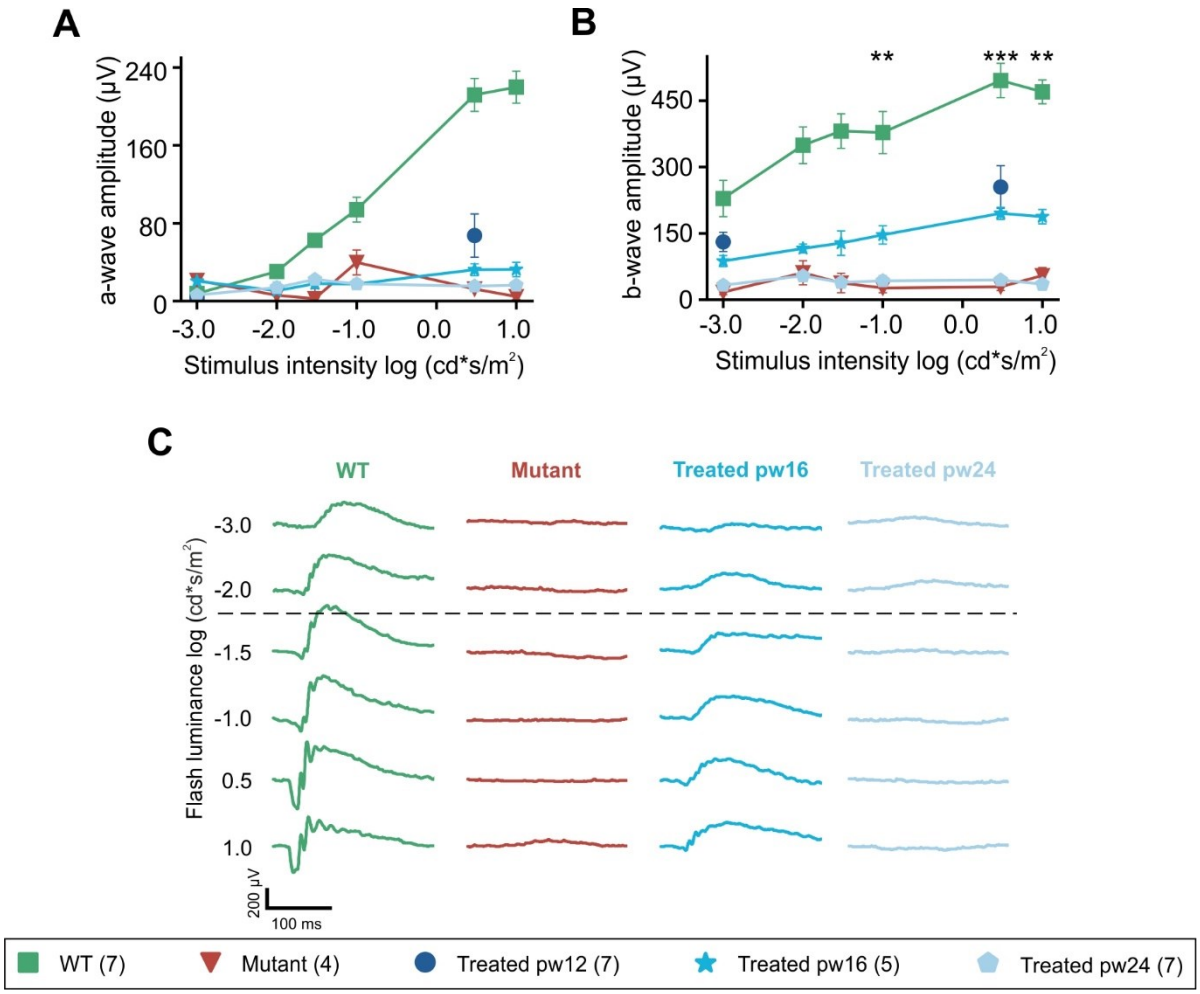

Fig. 37. Rescue of scotopic and mesopic retinal function. *Pde6b*$^{STOP/STOP}$ mice were treated (or not) at pw12, pw16, or pw24, and full-field single-flash ERGs recorded at pw40 along with 40-week-old *Pde6b*$^{STOP/+}$ (WT). Scotopic and mesopic **(A)** a-wave and **(B)** b-wave amplitudes. **(C)** Representative responses from a single retina in the scotopic and mesopic range. Data represent the mean ± SEM; Tukey's test for multiple comparisons. ** $P \leq 0.01$; *** $P \leq 0.001$. Asterisks, significant differences between mutant and treated at pw16. No statistical difference was found between animals treated at pw24 and mutant. N values are indicated in legend next to each group. Dashed line, the border between scotopic (above) and mesopic ranges (below).

Cone photoreceptor function was assessed after mice were light-adapted with a rod-desensitizing background. The ERG recordings of *Pde6b*$^{STOP/+}$ mice under photopic conditions showed an increase in the b-wave amplitude all the way up to the highest measured intensity of 1.5 log (cd·s/m^2) (**Fig. 38A,B**). The photopic ERG recordings showed no detectable responses in untreated *Pde6b*$^{STOP/STOP}$ mice, demonstrating the cone photoreceptor function was not preserved (**Fig. 38A,B**). The cone-driven (photopic) b-wave amplitudes of mice treated at 12 weeks of age were about 87% of WT at the highest measured intensity of 1.5 log (cd·s/m^2). When mice were treated at 16 weeks of age, the cone b-wave amplitude was

greater in comparison to untreated *Pde6b*$^{STOP/STOP}$ mice, however, the increase was not statistically significant. The photopic b-wave amplitudes of mice treated at 24 weeks of age were undistinguishable from untreated (**Fig. 38A,B**).

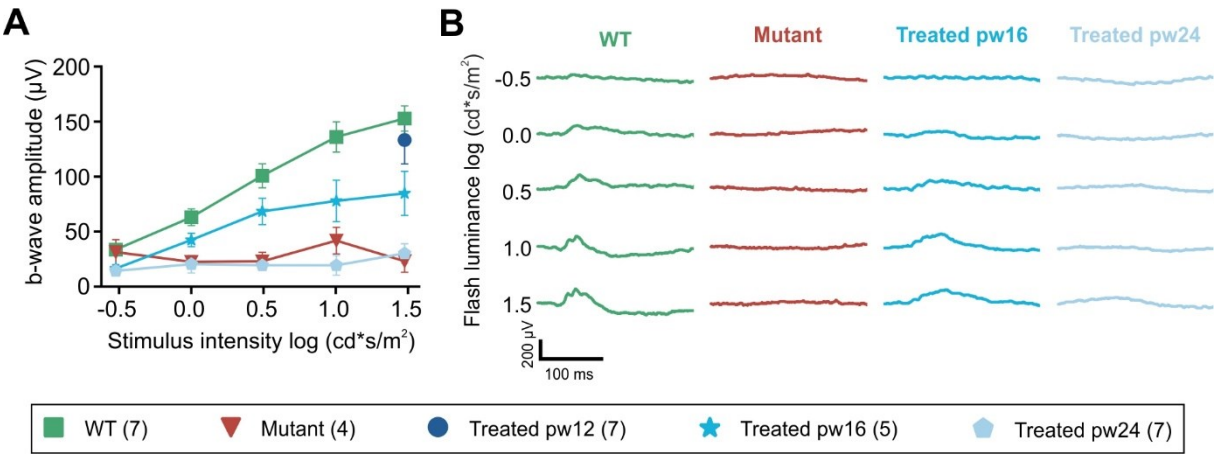

Fig. 38. Rescue of photopic retinal function. *Pde6b*$^{STOP/STOP}$ mice were treated (or not) at pw12, pw16, or pw24, and full-field single-flash ERGs recorded at pw40 along with 40-week-old *Pde6b*$^{STOP/+}$ (WT). **(A)** Photopic b-wave amplitudes. **(B)** Representative responses from a single retina. Data represent the mean ± SEM; Tukey's test for multiple comparisons. N values are indicated in legend next to each group.

4.8. Visual function completely rescued by treatment at 16 weeks of age or earlier

To investigate whether treatment at different disease stages rescues vision and its processing in the brain, the Morris water maze test was performed. In this test, mice use visual cues to orient themselves in order to locate a hidden submerged platform. As the experiment was carried out under dim light conditions, mainly rod photoreceptors were needed to accomplish this task.

First, escape latency was analyzed, which is the time it takes the mouse to find a hidden platform. While mean escape latency in *Pde6b*$^{STOP/+}$ mice decreased from 47.6 seconds on day 1 to 13.6 on day 5, it remained around 46.9 seconds over the 5-day training period in untreated Pde6b$^{STOP/STOP}$ mice (**Fig. 39A**). On day 1, there was no significant difference in the parameter escape latency between those two groups. The escape latency in *Pde6b*$^{STOP/STOP}$ mice treated at 12 or 16 weeks decreased over time so that on day 5 no significant difference was observable between these two groups vs WT. In contrast, *Pde6b*$^{STOP/STOP}$ mice treated at 24 weeks of age, like untreated mutants, showed no significant decrease in escape latency

over time. To compare escape latency over the entire 5-day training period, the area under the curve (AUC) was analyzed for each group (**Fig. 39B**). The AUC values for WT and *Pde6b*$^{STOP/STOP}$ mice treated at weeks 12, or 16 were similar. In contrast, the AUC of *Pde6b*$^{STOP/STOP}$ mice treated at 24 weeks of age was similar to untreated *Pde6b*$^{STOP/STOP}$ mice and was statistically greater when compared to *Pde6b*$^{STOP/+}$.

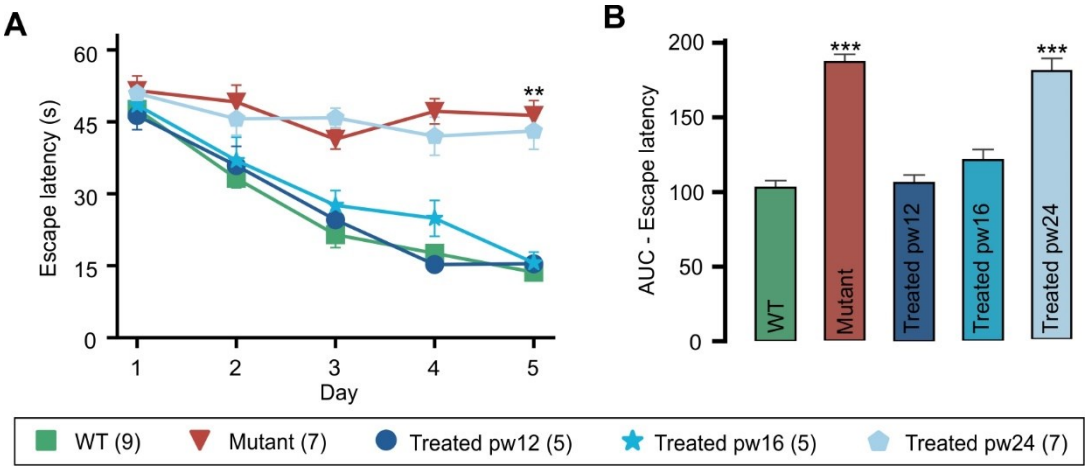

Fig. 39. Escape latency in the Morris water maze test. *Pde6b*$^{STOP/STOP}$ mice were treated at 12, 16, or 24 weeks of age, and then subjected to the Morris water maze behavioral test (under dim light conditions) over 5 consecutive days at 40 weeks of age (or 30 weeks for pw12-treated mice). **(A)** Escape latency (time to find the hidden platform), and **(B)** the area under the curve (AUC) for the parameter escape latency—presented as the mean ± SEM. Asterisks, significance for mutant and treated pw24 vs WT and treated pw12 and pw16. Tukey's test for multiple comparisons. ** $P \leq 0.01$; *** $P \leq 0.001$. N values are indicated in legend next to each group.

We next analyzed path length between the given start position and the hidden platform and found the results to be similar to escape latency. In *Pde6b*$^{STOP/+}$ mice and *Pde6b*$^{STOP/STOP}$ mice treated at 12, or 16 weeks of age, the mean path length progressively decreased over the 5 days (**Fig. 40A**). In contrast, path lengths in untreated *Pde6b*$^{STOP/STOP}$ mice and mice treated at 24 weeks of age remained high up to the last day. The total path length over the 5-day training session (AUC) was similar in *Pde6b*$^{STOP/+}$ mice and *Pde6b*$^{STOP/STOP}$ mice treated at 12, or 16 weeks. The AUC in untreated *Pde6b*$^{STOP/STOP}$ mice and mice treated at 24 weeks of age was significantly higher in comparison to WT (**Fig. 40B**). These findings are summarized by representative swim paths from days 1 and 5 for all six groups (**Fig. 40C**). On the first day, mice from all groups swam crisscross in the pool. On the last day, *Pde6b*$^{STOP/+}$ mice, as well as mice treated at 12 and 16 weeks of age, swam directly to the platform. Mice treated at 24 weeks and untreated *Pde6b*$^{STOP/STOP}$ mice still swam without direction in the pool.

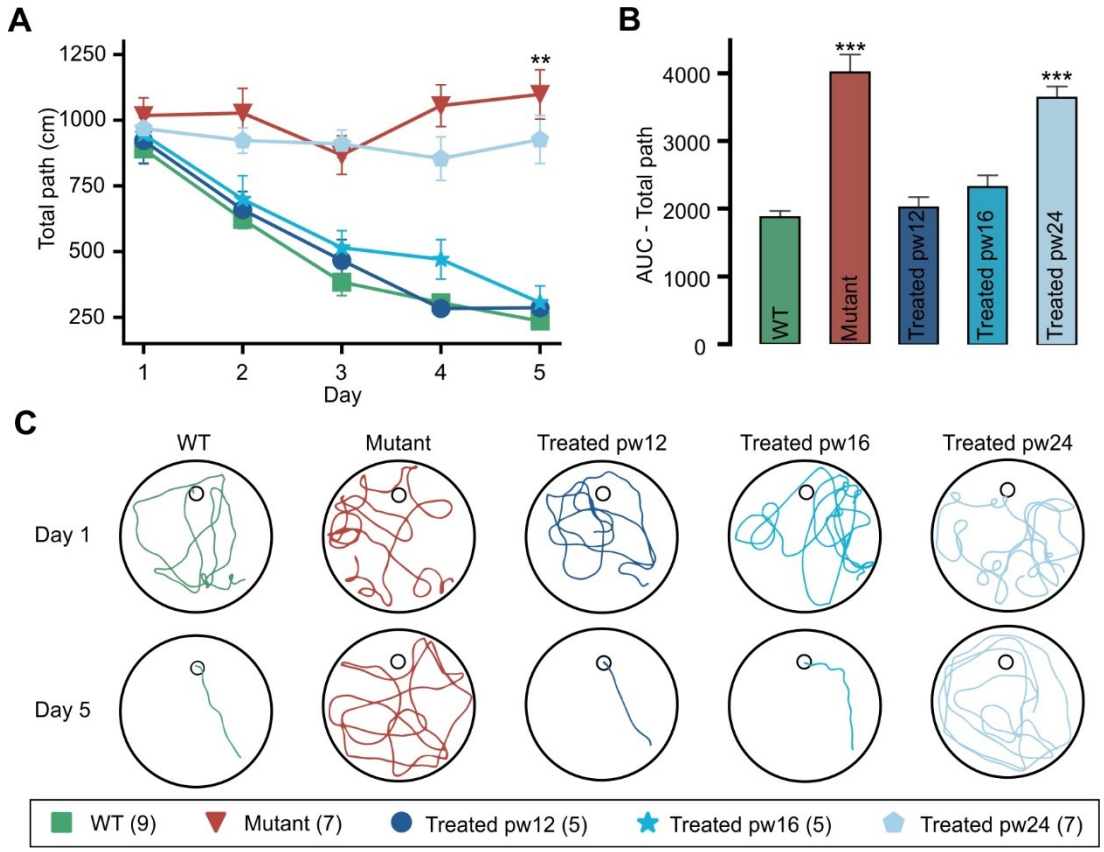

Fig. 40. Total path in the Morris water maze test. *Pde6b*$^{STOP/STOP}$ mice were treated at 12, 16, or 24 weeks of age, and then subjected to the Morris water maze behavioral test (under dim light conditions) over 5 consecutive days at 40 weeks of age (or 30 weeks for pw12-treated mice). **(A)** Total path (length of the swimming path taken to find the platform), and **(B)** the area under the curve (AUC) for the parameter total path—presented as the mean ± SEM. **(C)** Representative swimming trajectories for days 1 and 5. Asterisks, significance for mutant and treated pw24 vs WT and treated pw12 and pw16. Tukey's test for multiple comparisons. ** $P \leq 0.01$; *** $P \leq 0.001$. N values are indicated in legend next to each group.

After the last trial of the 5-day session, the platform was removed from the target quadrant and the mice were given 60 seconds to search for it. Time spent in each imaginary quadrant was measured. *Pde6b*$^{STOP/+}$ (WT) mice and *Pde6b*$^{STOP/STOP}$ mice treated at 12, or 16 weeks spent significantly more time in the right quadrant (56%, 53%, and 55%, respectively) (**Fig. 41**). In contrast, untreated *Pde6b*$^{STOP/STOP}$ mice and mice treated at 24 weeks of age spent 18% and 24% in the target quadrant, which is close to the chance level of 25%. Representative swim paths of the probe trial illustrate these findings. *Pde6b*$^{STOP/+}$ (WT) mice and *Pde6b*$^{STOP/STOP}$ mice treated at 12, or 16 weeks swam first to the region of the pool that previously contained the platform, which was opposite the starting position, and were then swimming around the

region, where the platform was previously located. In contrast, untreated *Pde6b*$^{STOP/STOP}$ and *Pde6b*$^{STOP/STOP}$ mice treated at 24 weeks were randomly swimming across all four quadrants.

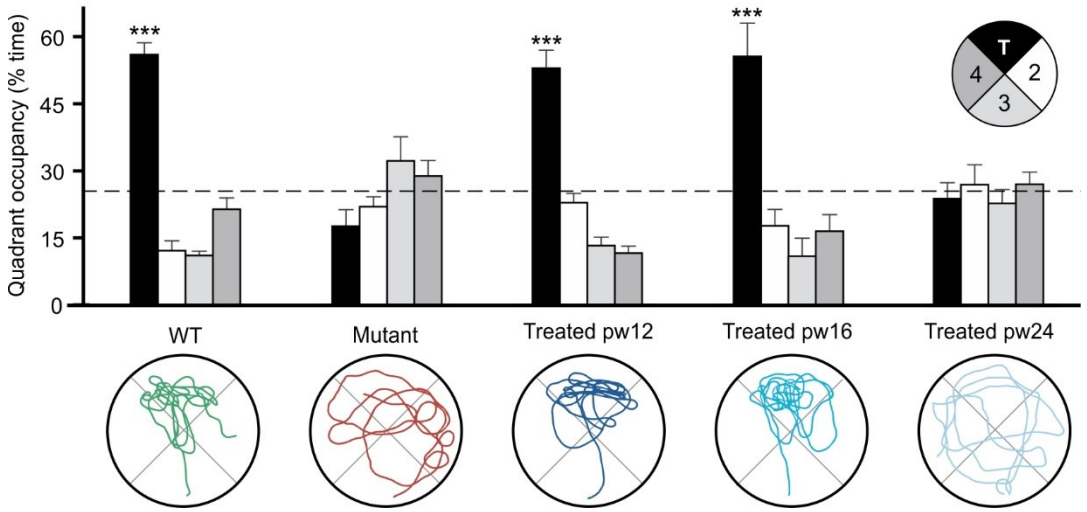

Fig. 41. Morris water maze probe trial performance. *Pde6b*$^{STOP/STOP}$ mice were treated at 12, 16, or 24 weeks of age, and performed the probe trial as the last trial on the 5th day at 40 weeks of age (or 30 weeks for pw12-treated mice) along with 40-weeks-old WT and untreated *Pde6b*$^{STOP/STOP}$ mice. For the probe trial, the platform was removed from the north target (T) quadrant, and the time spent in each quadrant was measured. Data presented as mean percentage (± SEM) of time spent in each quadrant; dashed line, chance level (25%). On the bottom representative tracings from the MWM probe trial are given. Asterisks, significance for T vs other quadrants. Tukey's test for multiple comparisons. *** $P \leq 0.001$. N values are indicated in legend next to each group.

5. Discussion

RP patients typically seek medical help when their vision is already impaired (85). Hence, rescue strategies should be evaluated at mid-to-late disease stages where retinal alterations are already present. To achieve long-lasting effects, different therapeutic approaches might only be viable within a given stage of disease progression, when certain preconditions are met (37). For instance, in gene therapy targeting primary mutations, the presence of functional photoreceptors is necessary. In this work, we used a genetically engineered RP gene therapy mouse model to determine the number of photoreceptors that are needed for a successful rescue. The mouse model was combined with the Cre-*loxP* system which enables temporal and spatial control of gene activation. *Pde6b*$^{STOP/STOP}$, *Pde6g*$^{CreERT2/+}$ (*Pde6b*$^{STOP/STOP}$) mice were injected with tamoxifen (referred to here as “treatment”) at 12, 16, or 24 weeks of age and analyzed at (30-) 40 weeks of age. With the Cre-*loxP* system, we sustainably treated more than 90% of the photoreceptors.

5.1. Successful therapeutic rescue of RP mice extends to late disease stages

Our study demonstrated a long-term functional rescue of visually guided in *Pde6b*$^{STOP/STOP}$ mice when the PDE6B protein was restored up to 16 weeks of age (**Figs. 39 - 41**). In contrast, the visually guided behavior of RP mice treated at 24 weeks of age was not rescued and was indistinguishable from 40-weeks-old untreated RP mice. These observations were in line with the ERG measurements (**Figs. 37, 38**) and the retinal morphology analysis (**Fig. 19**) demonstrating rescue of retinal function and photoreceptor cells, respectively by treatment at 12 or 16 weeks of age, but not at 24 weeks.

Strikingly, at 16 weeks of age, the ONL thickness was only 18% of that of a 40-weeks-old wild type (**Table 17**) and only 12% of rod photoreceptors were left. These results provide evidence of a broad therapeutic window in our RP mouse model and imply that the point of no return, at which gene therapy treatment is irreversible, can be pushed forward with more sophisticated methods and approaches of genetic therapeutic intervention. Especially at late disease stages, the therapeutic success may be dependent on the treatment efficiency, ie number of transduced cells and long-term gene expression. The Cre-*loxP* approach cannot be used in patients, but viral vectors are predominantly applied to replace the diseased gene. The efficacy of viral vectors is often not as high as in our study (86). Thus, it is important that future research will focus on further enhancing transduction efficiency, developing less invasive administrations, and providing long-term gene expression to ensure therapeutic success even

at late disease stages for a greater vision-related quality of life. A recent study successfully addressed the enhanced targeting of photoreceptors after the less invasive intravitreal injection by designing a newly engineered recombinant adeno-associated virus termed AAV2.GL and AAV2.NN (87). Also, new genome editing tools such as CRISPR/Cas9 are being developed for in vivo gene correction (88).

We showed that 24 weeks represent a turning point where rescue of vision in *Pde6b*$^{STOP/STOP}$ mice cannot be achieved anymore (**Figs. 39 - 41**). The ONL thickness of mutant mice at 24 weeks of age was 13% of that of a 40-weeks-old wild type (**Table 17**) and was not significantly thinner than the ONL thickness of 16-weeks-old mutants. The number of rod photoreceptors between mutant animals at 16 and 24 weeks of age was statistically different (**Fig. 19B**). We postulate that a substantial number of rod photoreceptors present in mutant mice at 24 weeks is already irreversibly damaged (79). The molecular mechanisms that contribute to the point of no return in neurodegenerative diseases remain unknown but may be important targets for delaying disease progression. Some of the proposed mechanisms limiting the timeline of the therapeutic intervention in neurodegenerative diseases are compromised neurotropic signaling, mitochondrial dysfunction and oxidative stress, permeabilization of mitochondrial membranes, aggregation of misfolded proteins causing stress of the endoplasmic reticulum, and aggregation of neurofilaments (89).

5.2. Restoration of dendritic length of inner retinal neurons is not required for complete rescue of visually-guided behavior

In response to photoreceptor degeneration in RP, rod bipolar and horizontal cells are deafferented, and consequently sprout and/or retract their dendrites (32, 90–93). Dendrite truncation was also present in our *Pde6b*$^{STOP/STOP}$ RP mouse model (**Figs. 22, 26**). It has been proposed that despite degradative remodeling, rod bipolar cells show increased sensitivity, a phenomenon described as homeostatic plasticity (94). Only a few studies investigated the morphology of inner retinal cells after rod photoreceptor rescue (95–97). However, apart from previous studies, in this work, RP animals were treated at multiple late disease stages. Also, this study analyzed whether inner retinal remodeling is halted at the stage at which treatment was administered. Our data show that the dendrite retraction from horizontal and rod bipolar cells is halted by treatment at 12 or 16 weeks of age (**Figs. 23A, 27**). These data revealed that dendrite truncations are not reversible; the restorative structural plasticity of the inner retina seems to be limited.

Thus, our visually guided behavior data show that dim-light (rod-dependent) vision was restored after treatment at late disease stages (pw12 and 16; **Figs. 39 - 41**) when rod bipolar cell dendrites are already severely truncated. These results show that it is not necessary to restore dendritic length/area to achieve the complete rescue of visually guided behaviors. Thus, short dendrites are functional and promote vision, and are probably not the limiting factor for gene therapy rescue.

The central nervous system (CNS) displays dynamic changes of dendrites during nervous system development which includes retraction and expansion (98, 99). Dendrite-regenerative capacity studies in adult mammals are limited. One study on the dendritic retraction in the medial prefrontal cortex in rats observed a complete reversal after 3 weeks of exposure to the stressor followed by the same amount of recovery (100). This study provided evidence that some dendrites possess the capability to regrow after short-term retraction. Regeneration of dendrites was also shown to occur in mice after acute brain prick injury by administering an extrinsic factor to promote neurite growth in CNS (101).

5.3. Ongoing potentially constructive RPE remodeling despite treatment

Alterations of the RPE in RP in response to photoreceptor degeneration were demonstrated in previous studies (44–47, 102). In line with these findings, we detected morphological alterations of the RPE in our mutant RP mouse model, including cell size irregularity, loss of honeycomb structure, and shift of the β-catenin staining from cell walls towards the cytoplasm (**Fig. 28**). The release of the β-catenin to the cytoplasm of RPE cells was already reported after laser photocoagulation in Bl6 mice (103). The released β-catenin may promote the epithelial-mesenchymal transition meaning a shift towards non-polarized cells that have invasive and migratory behavior under pathological circumstances (104).

Our results showed that the start of the RPE remodeling was in the central retina. RPE cells in the peripheral regions displayed only minor structural changes up to the age of 40 weeks (**Fig. 29**). This is consistent with the pattern of photoreceptor degeneration in mouse models of RP, which starts in the center of the retina and spreads to the periphery (105, 106). The morphological changes of the RPE cells may be driven by the diminished numbers of photoreceptors and shortened outer segments that would lead to reduced photoreceptor light absorption and oxygen consumption and, finally, cause chronic oxidative stress in the retina. Chronic activation of the oxidative stress response pathways was shown to cause mitochondrial damage (107), which damages the cell. In age-related macular disorder especially oxidative stress plays an important role in RPE dysfunction (17, 108). Regulating

the response to oxidative stress in RP mice via overexpression of Nrf2 has been shown to protect the RPE morphology (44). In addition, as the metabolism of the RPE and the photoreceptors is highly complementary (109, 110), decreased numbers of photoreceptors might lead to RPE starvation.

Unlike photoreceptor degeneration, photoreceptor functional loss, and inner retinal remodeling, RPE remodeling was not halted by treatment at 16 weeks of age (**Fig. 28**). The persistent changes of the RPE may be adaptive rather than solely destructive. Enlarged RPE cells and/or RPE cells that migrated toward lesion sites, might preserve an overall functioning RPE monolayer and maintain homeostasis (75). To what extent those altered RPE cells are still functional enough to support the retina in long term is still questionable and needs to be investigated in future research.

5.4. Partially slowed down potentially constructive retinal blood vessel remodeling despite treatment

Vascular damage and dysfunction are frequently associated with neurodegenerative disorders such as Alzheimer's disease, dementia, and Parkinson's disease (111–113). Degeneration of the retinal vasculature has been described in RP patients (54, 56, 82) and animal models (59, 62). An altered retinal vasculature system may be supplying inadequate oxygen and or nutrients, which could speed up secondary photoreceptor degeneration and would be a potential limitation to the gene therapy outcome.

In the untreated *Pde6b*$^{STOP/STOP}$ mice major retinal vascular changes were present, especially a reduction of the vessel area (**Fig. 35**) and an increased number of acellular capillaries (**Fig. 36**). Treatment at 12 weeks of age prevented these changes, while treatment at 16 weeks only partially slowed down the vessel remodeling. Treatment at 24 weeks did not impact the vascular remodeling, probably due to the ongoing photoreceptor degeneration and thus decreasing oxygen consumption and metabolic demand. Thus, normal visually guided behavior in our mice treated at 12 or 16 weeks suggests an adequate matching of metabolic needs and blood supply.

6. References

1. Cioffi CL (2020) *Introduction: Overview of the Human Eye, Mammalian Retina, and the Retinoid Visual Cycle*. Drug Delivery Challenges and Novel Therapeutic Approaches for Retinal Diseases (Springer). doi: 10.1007/7355_2020_94.
2. Veleri S, Lazar CH, Chang B, Sieving PA, Banin E, Swaroop A (2015) Biology and therapy of inherited retinal degenerative disease: insights from mouse models. *Disease models & mechanisms* 8:109–129. doi: 10.1242/dmm.017913.
3. Wilkinson CP, Hinton DR, Sadda SR, Wiedemann P (2017) *Ryan's Retina E-Book* (Elsevier Health Sciences).
4. Hoon M, Okawa H, Della Santina L, Wong ROL (2014) Functional architecture of the retina: development and disease. *Progress in retinal and eye research* 42:44–84. doi: 10.1016/j.preteyeres.2014.06.003.
5. Kolb H (2005) *Simple Anatomy of the Retina. In: Kolb H, Fernandez E, Nelson R, eds. Webvision: The Organization of the Retina and Visual System. Salt Lake City (UT): University of Utah Health Sciences Center.*
6. Karlstetter M, Scholz R, Rutar M, Wong WT, Provis JM, Langmann T (2015) Retinal microglia: just bystander or target for therapy? *Progress in retinal and eye research* 45:30–57. doi: 10.1016/j.preteyeres.2014.11.004.
7. Peichl L (2005) Diversity of mammalian photoreceptor properties: adaptations to habitat and lifestyle? *The anatomical record. Part A, Discoveries in molecular, cellular, and evolutionary biology* 287:1001–1012. doi: 10.1002/ar.a.20262.
8. Swaroop A, Kim D, Forrest D (2010) Transcriptional regulation of photoreceptor development and homeostasis in the mammalian retina. *Nature reviews. Neuroscience* 11:563–576. doi: 10.1038/nrn2880.
9. Demb JB, Singer JH (2015) Functional Circuitry of the Retina. *Annual Review of Vision Science* 1:263–289. doi: 10.1146/annurev-vision-082114-035334.
10. Szél A, Röhlich P, Caffé AR, Juliusson B, Aguirre G, van Veen T (1992) Unique topographic separation of two spectral classes of cones in the mouse retina. *J Comp Neurol* 325:327–342. doi: 10.1002/cne.903250302.
11. Sand A, Schmidt TM, Kofuji P (2012) Diverse types of ganglion cell photoreceptors in the mammalian retina. *Progress in retinal and eye research* 31:287–302. doi: 10.1016/j.preteyeres.2012.03.003.

12. J.B. Hurley (2009) *Phototransduction*. Encyclopedia of Neuroscience (Academic Press). doi: 10.1016/B978-008045046-9.00914-1.

13. Chen CK (2005) The vertebrate phototransduction cascade: amplification and termination mechanisms. *Reviews of physiology, biochemistry and pharmacology* 154:101–121. doi: 10.1007/s10254-005-0004-0.

14. Bertalmío M (2019) *Vision Models for High Dynamic Range and Wide Colour Gamut Imaging. The biological basis of vision: the retina. doi:* 10.1016/C2017-0-00438-X.

15. Tsukamoto Y, Omi N (2017) Classification of Mouse Retinal Bipolar Cells. Type-Specific Connectivity with Special Reference to Rod-Driven AII Amacrine Pathways. *Frontiers in neuroanatomy* 11:92. doi: 10.3389/fnana.2017.00092.

16. Shekhar K, Lapan SW, Whitney IE, Tran NM, Macosko EZ, Kowalczyk M, Adiconis X, Levin JZ, Nemesh J, Goldman M, McCarroll SA, Cepko CL, Regev A, Sanes JR (2016) Comprehensive Classification of Retinal Bipolar Neurons by Single-Cell Transcriptomics. *Cell* 166:1308-1323.e30. doi: 10.1016/j.cell.2016.07.054.

17. Strauss O (2005) The retinal pigment epithelium in visual function. *Physiological reviews* 85:845–881. doi: 10.1152/physrev.00021.2004.

18. Wang Z, Dillon J, Gaillard ER (2006) Antioxidant properties of melanin in retinal pigment epithelial cells. *Photochemistry and photobiology* 82:474–479. doi: 10.1562/2005-10-21-RA-725.

19. Boulton M, Dayhaw-Barker P (2001) The role of the retinal pigment epithelium: topographical variation and ageing changes. *Eye (Lond)* 15:384–389. doi: 10.1038/eye.2001.141.

20. Kur J, Newman EA, Chan-Ling T (2012) Cellular and physiological mechanisms underlying blood flow regulation in the retina and choroid in health and disease. *Progress in retinal and eye research* 31:377–406. doi: 10.1016/j.preteyeres.2012.04.004.

21. Bill A, Sperber G, and Ujiie K (1983) Physiology of the choroidal vascular bed. *International ophthalmology 6.2* 6:101–107. doi: 10.1007/BF00127638.

22. Naylor A, Hopkins A, Hudson N, Campbell M (2020) Tight Junctions of the Outer Blood Retina Barrier. *IJMS* 21:211. doi: 10.3390/ijms21010211.

23. Barabas P, Augustine J, Fernández JA, McGeown JG, McGahon MK, Curtis TM (2020) Ion channels and myogenic activity in retinal arterioles. *Current topics in membranes* 85:187–226. doi: 10.1016/bs.ctm.2020.01.008.

24. Hartong DT, Berson EL, Dryja TP (2006) Retinitis pigmentosa. *The Lancet* 368:1795–1809. doi: 10.1007/SpringerReference_104923.

25. Newton F, Megaw R (2020) Mechanisms of Photoreceptor Death in Retinitis Pigmentosa. *Genes* 11:1120. doi: 10.3390/genes11101120.

26. Hamel C (2006) Retinitis pigmentosa. *Orphanet journal of rare diseases* 1:40. doi: 10.1186/1750-1172-1-40.

27. Menghini M, Cehajic-Kapetanovic J, MacLaren RE (2020) Monitoring progression of retinitis pigmentosa: current recommendations and recent advances. *Expert opinion on orphan drugs* 8:67–78. doi: 10.1080/21678707.2020.1735352.

28. Tsang SH, Sharma T (2018) Retinitis Pigmentosa (Non-syndromic). *Advances in experimental medicine and biology* 1085:125–130. doi: 10.1007/978-3-319-95046-4_25.

29. Finn AP, Grewal DS, Vajzovic L (2018) Argus II retinal prosthesis system: a review of patient selection criteria, surgical considerations, and post-operative outcomes. *Clinical ophthalmology (Auckland, N.Z.)* 12:1089–1097. doi: 10.2147/OPTH.S137525.

30. Edwards TL, Cottriall CL, Xue K, Simunovic MP, Ramsden JD, Zrenner E, MacLaren RE (2018) Assessment of the Electronic Retinal Implant Alpha AMS in Restoring Vision to Blind Patients with End-Stage Retinitis Pigmentosa. *Ophthalmology* 125:432–443. doi: 10.1016/j.ophtha.2017.09.019.

31. Sahel J-A, Boulanger-Scemama E, Pagot C, Arleo A, Galluppi F, Martel JN, Degli Esposti S, Delaux A, Saint Aubert J-B de, Montleau C de, Gutman E, Audo I, Duebel J, Picaud S, Dalkara D, Blouin L, Taiel M, Roska B (2021) Partial recovery of visual function in a blind patient after optogenetic therapy. *Nature medicine* 27:1223–1229. doi: 10.1038/s41591-021-01351-4.

32. Marc RE, Jones BW, Watt CB, Strettoi E (2003) Neural remodeling in retinal degeneration. *Progress in retinal and eye research* 22:607–655. doi: 10.1016/S1350-9462(03)00039-9.

33. Jones BW, Kondo M, Terasaki H, Lin Y, McCall M, Marc RE (2012) Retinal remodeling. *Japanese journal of ophthalmology* 56:289–306. doi: 10.1007/s10384-012-0147-2.

34. Jones BW, Marc RE (2005) Retinal remodeling during retinal degeneration. *Experimental eye research* 81:123–137. doi: 10.1016/j.exer.2005.03.006.

35. Marc RE (2009) *Injury and Repair: Retinal Remodeling* (Elsevier, Amsterdam). doi: 10.1016/B978-0-12-374203-2.00220-7.

36. Jones BW, Pfeiffer RL, Ferrell WD, Watt CB, Marmor M, Marc RE (2016) Retinal remodeling in human retinitis pigmentosa. *Experimental eye research* 150:149–165. doi: 10.1016/j.exer.2016.03.018.

37. Pfeiffer RL, Marc RE, Jones BW (2020) Persistent remodeling and neurodegeneration in late-stage retinal degeneration. *Progress in retinal and eye research* 74:100771. doi: 10.1016/j.preteyeres.2019.07.004.

38. Jones BW, Watt CB, Marc RE (2005) Retinal remodelling. *Clinical and Experimental Optometry* 88:282–291. doi: 10.1111/j.1444-0938.2005.tb06712.x.

39. Milam AH, Zong-Yi Li, and Robert N. Fariss (1998) Histopathology of the human retina in retinitis pigmentosa. *Progress in retinal and eye research* 17:175–205. doi: 10.1016/s1350-9462(97)00012-8.

40. Szamier RB, Berson EL, Klein R, Meyers S (1979) Sex-linked retinitis pigmentosa: ultrastructure of photoreceptors and pigment epithelium. *Invest. Ophthalmol. Vis. Sci.* 18:145–160.

41. Gartner S, Henkind P (1982) Pathology of Retinitis Pigmentosa. *Ophthalmology* 89:1425–1432. doi: 10.1016/S0161-6420(82)34620-5.

42. Vinores SA, Küchle M, Derevjanik NL, Henderer JD, Mahlow J, Green WR, Campochiaro PA (1995) Blood-retinal barrier breakdown in retinitis pigmentosa: light and electron microscopic immunolocalization. *Histology and histopathology* 10:913–923.

43. Li Z-Y, Possin DE, Milam AH (1995) Histopathology of Bone Spicule Pigmentation in Retinitis Pigmentosa. *Ophthalmology* 102:805–816. doi: 10.1016/S0161-6420(95)30953-0.

44. Wu DM, Ji X, Ivanchenko MV, Chung M, Piper M, Rana P, Wang SK, Xue Y, West E, Zhao SR, Xu H, Cicconet M, Xiong W, Cepko CL (2021) Nrf2 overexpression rescues the RPE in mouse models of retinitis pigmentosa. *JCI insight* 6. doi: 10.1172/jci.insight.145029.

45. Jiang Y, Qi X, Chrenek MA, Gardner C, Boatright JH, Grossniklaus HE, Nickerson JM (2013) Functional principal component analysis reveals discriminating categories of retinal pigment epithelial morphology in mice. *Investigative ophthalmology & visual science* 54:7274–7283. doi: 10.1167/iovs.13-12450.

46. Chrenek MA, Dalal N, Gardner C, Grossniklaus H, Jiang Y, Boatright JH, Nickerson JM (2012) Analysis of the RPE sheet in the rd10 retinal degeneration model. *Advances in experimental medicine and biology* 723:641–647. doi: 10.1007/978-1-4614-0631-0_81.

47. Neuhardt TH, May CA, Wilsch C, Eichhorn M, Lütjen-Drecoll E (1999) Morphological Changes of Retinal Pigment Epithelium and Choroid in rd-mice. *Experimental eye research* 68:75–83. doi: 10.1006/exer.1998.0589.

48. Jaissle GB, May CA, van de Pavert SA, Wenzel A, Claes-May E, Giessl A, Szurman P, Wolfrum U, Wijnholds J, Fischer MD, Fisher MD, Humphries P, Seeliger MW (2010) Bone

spicule pigment formation in retinitis pigmentosa: insights from a mouse model. *Graefe's archive for clinical and experimental ophthalmology = Albrecht von Graefes Archiv fur klinische und experimentelle Ophthalmologie* 248:1063–1070. doi: 10.1007/s00417-009-1253-9.

49. Grunwald JE, Maguire AM, Dupont J (1996) Retinal Hemodynamics in Retinitis Pigmentosa. *American journal of ophthalmology* 122:502–508. doi: 10.1016/S0002-9394(14)72109-9.

50. Yang YJ, Peng J, Ying D, Peng QH (2018) A Brief Review on the Pathological Role of Decreased Blood Flow Affected in Retinitis Pigmentosa. *Journal of ophthalmology* 2018:3249064. doi: 10.1155/2018/3249064.

51. Beutelspacher SC, Serbecic N, Barash H, Burgansky-Eliash Z, Grinvald A, Krastel H, Jonas JB (2011) Retinal blood flow velocity measured by retinal function imaging in retinitis pigmentosa. *Graefe's archive for clinical and experimental ophthalmology* 249:1855–1858. doi: 10.1007/s00417-011-1757-y.

52. Lang M, Harris A, Ciulla TA, Siesky B, Patel P, Belamkar A, Mathew S, Verticchio Vercellin AC (2019) Vascular dysfunction in retinitis pigmentosa. *Acta ophthalmologica* 97:660–664. doi: 10.1111/aos.14138.

53. Corazza P, Cirafici P, Testa V, Orlans HO, Berisso M, Traverso CE, Vagge A, Nicolò M (2021) Vascular Density and Retinal Function in Patients with Retinitis Pigmentosa Evaluated by Swept-Source OCT Angiography and Microperimetry. *Ophthalmologica. Journal international d'ophtalmologie. International journal of ophthalmology. Zeitschrift fur Augenheilkunde* 244:27–33. doi: 10.1159/000507961.

54. Battaglia Parodi M, Cicinelli MV, Rabiolo A, Pierro L, Gagliardi M, Bolognesi G, Bandello F (2017) Vessel density analysis in patients with retinitis pigmentosa by means of optical coherence tomography angiography. *The British journal of ophthalmology* 101:428–432. doi: 10.1136/bjophthalmol-2016-308925.

55. Shen C, Li Y, Wang Q, Chen Y-N, Li W, Wei W-B (2020) Choroidal vascular changes in retinitis pigmentosa patients detected by optical coherence tomography angiography. *BMC ophthalmology* 20:384. doi: 10.1186/s12886-020-01640-5.

56. Rezaei KA, Zhang Q, Chen C-L, Chao J, Wang RK (2017) Retinal and choroidal vascular features in patients with retinitis pigmentosa imaged by OCT based microangiography. *Graefe's archive for clinical and experimental ophthalmology = Albrecht von Graefes Archiv fur klinische und experimentelle Ophthalmologie* 255:1287–1295. doi: 10.1007/s00417-017-3633-x.

57. Riva CE, Grunwald JE, & Sinclair SH (1983) Laser Doppler Velocimetry study of the effect of pure oxygen breathing on retinal blood flow. *Investigative ophthalmology & visual science* 24:47–51.

58. Matthes MT, Bok D (1984) Blood vascular abnormalities in the degenerative mouse retina (C57BL/6J-rd le). *Investigative ophthalmology & visual science* 25:364–369.

59. Fernández-Sánchez L, Esquiva G, Pinilla I, Lax P, Cuenca N (2018) Retinal Vascular Degeneration in the Transgenic P23H Rat Model of Retinitis Pigmentosa. *Frontiers in neuroanatomy* 12. doi: 10.3389/fnana.2018.00055.

60. Joseph H, Yücel YH, Zhou X, Mathieu E, Paczka-Giorgi LA, Gupta N (2018) Progressive loss of retinal blood vessels in a live model of retinitis pigmentosa. *Canadian journal of ophthalmology. Journal canadien d'ophtalmologie* 53:391–401. doi: 10.1016/j.jcjo.2017.10.014.

61. Kim T-H, Son T, Lu Y, Alam M, Yao X (2018) Comparative Optical Coherence Tomography Angiography of Wild-Type and rd10 Mouse Retinas. *Translational vision science & technology* 7:42. doi: 10.1167/tvst.7.6.42.

62. Liu H, Tang J, Du Y, Saadane A, Tonade D, Samuels I, … & Kern, T. S. (2016) Photoreceptor cells influence retinal vascular degeneration in mouse models of retinal degeneration and diabetes. *Investigative ophthalmology & visual science* 10:4272–4281. doi: 10.1167/iovs.16-19415.

63. Brown WR (2010) A review of string vessels or collapsed, empty basement membrane tubes. *Journal of Alzheimer's disease* 21:725–739. doi: 10.3233/JAD-2010-100219.

64. Nagy A (2000) Cre recombinase: The universal reagent for genome tailoring. *genesis* 26:99–109.

65. Kim H, Kim M, Im S-K, Fang S (2018) Mouse Cre-LoxP system: general principles to determine tissue-specific roles of target genes. *Laboratory animal research* 34:147–159. doi: 10.5625/lar.2018.34.4.147.

66. Indra AK, Warot X, Brocard J, Bornert JM, Xiao JH, Chambon P, Metzger D (1999) Temporally-controlled site-specific mutagenesis in the basal layer of the epidermis: comparison of the recombinase activity of the tamoxifen-inducible Cre-ERT and Cre-ERT2 recombinases. *Nucleic acids research* 27:4324–4327. doi: 10.1093/nar/27.22.4324.

67. Prigge JR, Wiley JA, Talago EA, Young EM, Johns LL, Kundert JA, Schmidt EE (2013) Nuclear double-fluorescent reporter for in vivo and ex vivo analyses of biological transitions in mouse nuclei. *Mammalian genome* 24:389–399. doi: 10.1007/s00335-013-9469-8.

68. Davis RJ, Hsu C-W, Tsai Y-T, Wert KJ, Sancho-Pelluz J, Lin C-S, Tsang SH (2013) Therapeutic margins in a novel preclinical model of retinitis pigmentosa. *The Journal of neuroscience* 33:13475–13483. doi: 10.1523/JNEUROSCI.0419-13.2013.

69. McLaughlin ME, Ehrhart TL, Berson EL, Dryja TP (1995) Mutation spectrum of the gene encoding the beta subunit of rod phosphodiesterase among patients with autosomal recessive retinitis pigmentosa. *Proceedings of the National Academy of Sciences* 92:3249–3253. doi: 10.1073/pnas.92.8.3249.

70. Koch SF, Tsai Y-T, Duong JK, Wu W-H, Hsu C-W, Wu W-P, Bonet-Ponce L, Lin C-S, Tsang SH (2015) Halting progressive neurodegeneration in advanced retinitis pigmentosa. *The Journal of clinical investigation* 125:3704–3713. doi: 10.1172/JCI82462.

71. Koch SF, Duong JK, Hsu CW, Tsai YT, Lin CS, Wahl-Schott CA, Tsang SH (2017) Genetic rescue models refute nonautonomous rod cell death in retinitis pigmentosa. *Proceedings of the National Academy of Sciences of the United States of America* 114:5259-5264. doi: 10.1073/pnas.1708940114.

72. Maj M, Wagner L, Tretter V (2019) 20 Years of Secretagogin: Exocytosis and Beyond. *Frontiers in molecular neuroscience* 12:29. doi: 10.3389/fnmol.2019.00029.

73. Mattapallil MJ, Wawrousek EF, Chan C-C, Zhao H, Roychoudhury J, Ferguson TA, Caspi RR (2012) The Rd8 mutation of the Crb1 gene is present in vendor lines of C57BL/6N mice and embryonic stem cells, and confounds ocular induced mutant phenotypes. *Investigative ophthalmology & visual science* 53:2921–2927. doi: 10.1167/iovs.12-9662.

74. Chang B, Dacey MS, Hawes NL, Hitchcock PF, Milam AH, Atmaca-Sonmez P, Nusinowitz S, Heckenlively JR (2006) Cone photoreceptor function loss-3, a novel mouse model of achromatopsia due to a mutation in Gnat2. *Investigative ophthalmology & visual science* 47:5017–5021. doi: 10.1167/iovs.05-1468.

75. Chen M, Rajapakse D, Fraczek M, Luo C, Forrester JV, Xu H (2016) Retinal pigment epithelial cell multinucleation in the aging eye - a mechanism to repair damage and maintain homeostasis. *Aging cell* 15:436–445. doi: 10.1111/acel.12447.

76. Lamprecht MR, Sabatini DM, Carpenter AE (2007) CellProfiler: free, versatile software for automated biological image analysis. *BioTechniques* 42:71–75. doi: 10.2144/000112257.

77. Zudaire E, Gambardella L, Kurcz C, Vermeren S (2011) A computational tool for quantitative analysis of vascular networks. *PloS one* 6:e27385. doi: 10.1371/journal.pone.0027385.

78. Chou JC, Rollins SD, Fawzi AA (2013) Trypsin digest protocol to analyze the retinal vasculature of a mouse model. *Journal of visualized experiments: JoVE*:e50489. doi: 10.3791/50489.

79. Clarke G, Collins RA, Leavitt BR, Andrews DF, Hayden MR, Lumsden CJ, McInnes RR (2000) A one-hit model of cell death in inherited neuronal degenerations. *Nature* 406:195–199. doi: 10.1038/35018098.

80. Benchorin G, Calton MA, Beaulieu MO, Vollrath D (2017) Assessment of Murine Retinal Function by Electroretinography. *Bio-protocol* 7. doi: 10.21769/BioProtoc.2218.

81. Puthussery T, Gayet-Primo J, Taylor WR (2010) Localization of the calcium-binding protein secretagogin in cone bipolar cells of the mammalian retina. *The Journal of comparative neurology* 518:513–525. doi: 10.1002/cne.22234.

82. Jauregui R, Park KS, Duong JK, Mahajan VB, Tsang SH (2018) Quantitative progression of retinitis pigmentosa by optical coherence tomography angiography. *Scientific reports* 8:13130. doi: 10.1038/s41598-018-31488-1.

83. Pinto LH, Invergo B, Shimomura K, Takahashi JS, Troy JB (2007) Interpretation of the mouse electroretinogram. *Documenta ophthalmologica. Advances in ophthalmology* 115:127–136. doi: 10.1007/s10633-007-9064-y.

84. Tanimoto N, Sothilingam V, Kondo M, Biel M, Humphries P, Seeliger MW (2015) Electroretinographic assessment of rod- and cone-mediated bipolar cell pathways using flicker stimuli in mice. *Scientific reports* 5:10731. doi: 10.1038/srep10731.

85. Verbakel SK, van Huet RAC, Boon CJF, Hollander AI den, Collin RWJ, Klaver CCW, Hoyng CB, Roepman R, Klevering BJ (2018) Non-syndromic retinitis pigmentosa. *Progress in retinal and eye research* 66:157–186. doi: 10.1016/j.preteyeres.2018.03.005.

86. Gallego C, Gonçalves MAFV, Wijnholds J (2020) Novel Therapeutic Approaches for the Treatment of Retinal Degenerative Diseases: Focus on CRISPR/Cas-Based Gene Editing. *Frontiers in neuroscience* 14:838. doi: 10.3389/fnins.2020.00838.

87. Pavlou M, Schön C, Occelli LM, Rossi A, Meumann N, Boyd RF, Bartoe JT, Siedlecki J, Gerhardt MJ, Babutzka S, Bogedein J, Wagner JE, Priglinger SG, Biel M, Petersen-Jones SM, Büning H, Michalakis S (2021) Novel AAV capsids for intravitreal gene therapy of photoreceptor disorders. *EMBO molecular medicine* 13:e13392. doi: 10.15252/emmm.202013392.

88. Burnight ER, Giacalone JC, Cooke JA, Thompson JR, Bohrer LR, Chirco KR, Drack AV, Fingert JH, Worthington KS, Wiley LA, Mullins RF, Stone EM, Tucker BA (2018) CRISPR-

Cas9 genome engineering: Treating inherited retinal degeneration. *Progress in retinal and eye research* 65:28–49. doi: 10.1016/j.preteyeres.2018.03.003.

89. JS Viana R, B Fonseca M, M Ramalho R, F Nunes A, & MP Rodrigues C (2010) Organelle stress sensors and cell death mechanisms in neurodegenerative diseases. *CNS & Neurological Disorders-Drug Targets (Formerly Current Drug Targets-CNS & Neurological Disorders)* 9:679–692. doi: 10.2174/187152710793237511.

90. Yang J, Nan C, Ripps H, Shen W (2015) Destructive Changes in the Neuronal Structure of the FVB/N Mouse Retina. *PloS one* 10:e0129719. doi: 10.1371/journal.pone.0129719.

91. Strettoi E, Pignatelli V, Rossi C, Porciatti V, Falsini B (2003) Remodeling of second-order neurons in the retina of rd/rd mutant mice. *Vision Research* 43:867–877. doi: 10.1016/S0042-6989(02)00594-1.

92. Barhoum R, Martínez-Navarrete G, Corrochano S, Germain F, Fernandez-Sanchez L, La Rosa EJ de, La Villa P de, Cuenca N (2008) Functional and structural modifications during retinal degeneration in the rd10 mouse. *Neuroscience* 155:698–713. doi: 10.1016/j.neuroscience.2008.06.042.

93. Stefanov A, Novelli E, Strettoi E (2020) Inner retinal preservation in the photoinducible I307N rhodopsin mutant mouse, a model of autosomal dominant retinitis pigmentosa. *The Journal of comparative neurology* 528:1502–1522. doi: 10.1002/cne.24838.

94. Leinonen H, Pham NC, Boyd T, Santoso J, Palczewski K, Vinberg F (2020) Homeostatic plasticity in the retina is associated with maintenance of night vision during retinal degenerative disease. *eLife* 9. doi: 10.7554/eLife.59422.

95. Wang T, Pahlberg J, Cafaro J, Frederiksen R, Cooper AJ, Sampath AP, Field GD, Chen J (2019) Activation of Rod Input in a Model of Retinal Degeneration Reverses Retinal Remodeling and Induces Formation of Functional Synapses and Recovery of Visual Signaling in the Adult Retina. *The Journal of neuroscience : the official journal of the Society for Neuroscience* 39:6798–6810. doi: 10.1523/JNEUROSCI.2902-18.2019.

96. Beltran WA, Cideciyan AV, Lewin AS, Iwabe S, Khanna H, Sumaroka A, Chiodo VA, Fajardo DS, Román AJ, Deng W-T, Swider M, Alemán TS, Boye SL, Genini S, Swaroop A, Hauswirth WW, Jacobson SG, Aguirre GD (2012) Gene therapy rescues photoreceptor blindness in dogs and paves the way for treating human X-linked retinitis pigmentosa. *Proceedings of the National Academy of Sciences of the United States of America* 109:2132–2137. doi: 10.1073/pnas.1118847109.

97. Beltran WA, Cideciyan AV, Iwabe S, Swider M, Kosyk MS, McDaid K, Martynyuk I, Ying G-S, Shaffer J, Deng W-T, Boye SL, Lewin AS, Hauswirth WW, Jacobson SG, Aguirre GD (2015) Successful arrest of photoreceptor and vision loss expands the therapeutic window

of retinal gene therapy to later stages of disease. *Proceedings of the National Academy of Sciences of the United States of America* 112:E5844-53. doi: 10.1073/pnas.1509914112.

98. Cline HT (2001) Dendritic arbor development and synaptogenesis. *Current opinion in neurobiology* 11:118–126. doi: 10.1016/s0959-4388(00)00182-3.

99. Prigge CL, Kay JN (2018) Dendrite morphogenesis from birth to adulthood. *Current opinion in neurobiology* 53:139–145. doi: 10.1016/j.conb.2018.07.007.

100. Radley JJ, Rocher AB, Janssen WGM, Hof PR, McEwen BS, Morrison JH (2005) Reversibility of apical dendritic retraction in the rat medial prefrontal cortex following repeated stress. *Experimental neurology* 196:199–203. doi: 10.1016/j.expneurol.2005.07.008.

101. Paveliev M, Fenrich KK, Kislin M, Kuja-Panula J, Kulesskiy E, Varjosalo M, Kajander T, Mugantseva E, Ahonen-Bishopp A, Khiroug L, Kulesskaya N, Rougon G, Rauvala H (2016) HB-GAM (pleiotrophin) reverses inhibition of neural regeneration by the CNS extracellular matrix. *Scientific reports* 6:33916. doi: 10.1038/srep33916.

102. Napoli D, Biagioni M, Billeri F, Di Marco B, Orsini N, Novelli E, Strettoi E (2021) Retinal Pigment Epithelium Remodeling in Mouse Models of Retinitis Pigmentosa. *International journal of molecular sciences* 22:5381. doi: 10.3390/ijms22105381.

103. Han JW, Lyu J, Park YJ, Jang SY, Park TK (2015) Wnt/β-Catenin Signaling Mediates Regeneration of Retinal Pigment Epithelium After Laser Photocoagulation in Mouse Eye. *Investigative ophthalmology & visual science* 56:8314–8324. doi: 10.1167/iovs.15-18359.

104. Zhou M, Geathers JS, Grillo SL, Weber SR, Wang W, Zhao Y, Sundstrom JM (2020) Role of Epithelial-Mesenchymal Transition in Retinal Pigment Epithelium Dysfunction. *Frontiers in cell and developmental biology* 8:501. doi: 10.3389/fcell.2020.00501.

105. Carter-Dawson LD, M. M. LaVail, and R. L. Sidman (1978) Differential effect of the rd mutation on rods and cones in the mouse retina. *Investigative ophthalmology & visual science* 17:489–498.

106. Jimenez A-J, et al. (1996) The spatio-temporal pattern of photoreceptor degeneration in the aged rd/rd mouse retina. *Cell and tissue research* 284:193–202. doi: 10.1007/s004410050579.

107. Kroeger H, Chiang W-C, Felden J, Nguyen A, Lin JH (2019) ER stress and unfolded protein response in ocular health and disease. *The FEBS journal* 286:399–412. doi: 10.1111/febs.14522.

108. Datta S, Cano M, Ebrahimi K, Wang L, Handa JT (2017) The impact of oxidative stress and inflammation on RPE degeneration in non-neovascular AMD. *Progress in retinal and eye research* 60:201–218. doi: 10.1016/j.preteyeres.2017.03.002.

109. Hurley JB (2021) Retina Metabolism and Metabolism in the Pigmented Epithelium: A Busy Intersection. *Annual Review of Vision Science* 7:665–692. doi: 10.1146/annurev-vision-100419-115156.

110. Li B, Zhang T, Liu W, Wang Y, Xu R, Zeng S, Zhang R, Zhu S, Gillies MC, Zhu L, Du J (2020) Metabolic Features of Mouse and Human Retinas: Rods versus Cones, Macula versus Periphery, Retina versus RPE. *iScience* 23:101672. doi: 10.1016/j.isci.2020.101672.

111. Bracko O, Cruz Hernández JC, Park L, Nishimura N, Schaffer CB (2021) Causes and consequences of baseline cerebral blood flow reductions in Alzheimer's disease. *Journal of cerebral blood flow and metabolism : official journal of the International Society of Cerebral Blood Flow and Metabolism* 41:1501–1516. doi: 10.1177/0271678X20982383.

112. Snyder HM, Corriveau RA, Craft S, Faber JE, Greenberg SM, Knopman D, Lamb BT, Montine TJ, Nedergaard M, Schaffer CB, Schneider JA, Wellington C, Wilcock DM, Zipfel GJ, Zlokovic B, Bain LJ, Bosetti F, Galis ZS, Koroshetz W, Carrillo MC (2015) Vascular contributions to cognitive impairment and dementia including Alzheimer's disease. *Alzheimer's & dementia : the journal of the Alzheimer's Association* 11:710–717. doi: 10.1016/j.jalz.2014.10.008.

113. Yuan C (2020) *Chapter 1: Vascular dysfunction and neurodegenerative disease. In Vessel Based Imaging Techniques (eds Yuan, C. et al.)* (Springer International Publishing AG, Seattle).